UNIVERSITÀ DEGLI STUDI DI PALERMO

Dottorato di Ricerca in Scienze Fisiche
Dipartimento di Fisica e Chimica-Emilio Segré
Settore Scientifico Disciplinare - FIS/05 - Astronomia e Astrofisica

A comprensive spectral-timing study of Ultraluminous X-ray sources

IL DOTTORE
ALESSANDRA ROBBA

IL COORDINATORE
Prof. MARCO CANNAS

IL TUTOR
Dr. GIANCARLO CUSUMANO

CO TUTOR
Dr. CIRO PINTO

CICLO XXXV
ANNO CONSEGUIMENTO TITOLO 2023

Contents

List of Figures

List of Tables

Abstract

Almost all type of astronomical objects, from individual stars to the interstellar medium, have been discovered to emit X-rays, which indicates that they host a plasma heated to temperatures of a million degrees by energetic phenomena. In other words, X-ray astronomy enables us to unveil and study the hot and energetic Universe. One of the most important achievements was the discovery of X-ray binaries (XRBs), in which a compact object, i.e. a black hole (BH) or a neutron star (NS) or a white dwarf (WD), accretes matter from a companion star. The brightest among XRBs can achieve extreme luminosities and exhibit tremendous phenomena of ejection with matter leaving the systems at significant fractions of the speed of light. These are the so-called Ultraluminous X-ray sources (ULXs), a subclass of the XRBs which are point-like off-nuclear sources, mainly powered by rapid matter accretion onto compact objects with a luminosity above 10^{39} erg/s, peaking in the X-ray band (0.3–10 keV).

The purpose of this thesis is to investigate this accretion regime, deepening the study of ULXs. In particular, I applied spectral and timing techniques, to analyse the nature and the physics of known ULXs and search for new ones. In this work, I present recent results for different ULXs with various spectral shapes which are related to the combination of accretion rate and system inclination. The first chapter of this thesis introduces the theory of accretion, describes the instrumentation used in the thesis and presents the general X-ray data reduction procedures that have been adopted.

The second chapter reports the identification and the properties of a new ULX candidate in the galaxy NGC 55, which was previously classified as a transient X-ray

source with a luminosity around a few 10^{38} erg/s. Thanks to recent *XMM-Newton* and the *Swift* observations, we show that the source surpasses the 10^{39} erg/s threshold in multiple occurrences.

In the third chapter, I focus on the pulsating NGC 1313 X-2, which exhibits remarkable X-ray spectral variability. I performed a spectral analysis of all archival data collected by *XMM-Newton*, studying the spectral evolution over about 20 years. Above 10^{39} erg/s the spectral components deviate from the L–T^4 in agreement with an expansion of discs with an extremely-high accretion rate around a stellar mass compact object. Some of the variability is likely due to the wind detected with Doppler-shifted lines as shown by several ULXs.

The final project is dedicated to timing analysis, focusing on the changes in the intrinsic variability and in the time lags during high and low flux states of the source NGC 1313 X-2. I applied Fourier advanced techniques to the X-ray time series, to study the time variability of the emitted radiation. I extracted the power spectrum, cross-spectrum and time lag in the frequency domain, between light curves extracted in two different bands (i.e. soft 0.3–1.2 keV and hard 1.2–10 keV). I detected a soft and a hard lag at low frequencies, with magnitudes of a few hundred seconds, whose origin could support the wind scenario.

The final chapter contains the conclusions of the thesis, the potential future research developments in this field and the promising upcoming X-ray observatories.

1 Introduction

This Chapter provides a brief introduction to the physics of accretion and X-ray binary systems, which are composed of a compact object accreting material from a companion star and emit mostly in the X-ray band.

1.1 The physics of accretion onto compact objects

X-ray astronomy is a relatively young branch of astronomy, being only 60 years old. Isolated stars, like the Sun, are known to emit X-rays but it is typically a minority of the bolometric luminosity. However, most stars are found in binary systems some of which are interacting, i.e. transferring matter via Roche-lobe overflow or winds, in which cases the X-ray throughput can be the dominant one. These are known as X-ray binaries (XRBs) where the primary, accreting, star is a high-density compact object i.e. either a black hole or a neutron star or a white dwarf. The first X-ray binary, Scorpius X-1, was discovered by Giacconi 1974 with a sounding rocket carrying a soft X-ray detector.

The physical process invoked to explain the X-ray emission in XRBs is the accretion of matter, an efficient mechanism that allows these systems to convert gravitational energy into radiation. The two stars orbit around their common centre of mass or barycentre, and for the conservation of the angular momentum, the matter spirals around the compact object forming an accretion disc, whose emission peaks in the X-ray band ($\sim 0.1 - 100$ keV) due to viscosity and other processes such as Compton scattering, which heats up the matter to millions of degrees.

Let us consider a star of mass M and radius R which accretes a mass-test m, initially

at infinity; the energy released by the accretion of m in the form of radiation equals the variation of gravitational energy of the test-mass in moving from infinity to R: $\Delta E_{acc} = GMm/R$, where G[1] is the gravitational constant. This energy is emitted as radiation, with a luminosity equal to

$$L_{acc} \approx \frac{GM\dot{m}}{R} \tag{1.1}$$

where $\dot{m}$ is the accretion rate.

Not all the gravitational energy is converted into radiation but only a certain fraction. This is parameterised with a dimensionless parameter η, which represents the conversion efficiency, namely the efficiency of the process to transform the rest energy of the accretion mass into luminosity. Formula 1.1 becomes:

$$L_{acc} = \eta \dot{m} c^2 \tag{1.2}$$

where c represents the speed of light[2]. For accreting bodies with a solid surface, η can be expressed as GM/Rc^2. The parameter η is strongly dependent on the compactness of the accreting object: the larger the ratio M/R, the greater the efficiency. Using the standard values for M and R of a NS, i.e. 1.4 $M_\odot$[3] and R = 10 km, $\eta = 0.15$. In the case of a WD, η is much smaller, since M = $M_\odot$ and the radius is 1000 times larger. An analogous calculation for BHs gives values of $\eta \sim 0.06$ for a non-rotating, Schwarzschild BH, and ~ 0.4 for a maximally rotating Kerr black hole (e.g. Thorne 1974).

1.1.1 Accretion disc emission

It is very important to study the spectral range of the radiation emitted by an accretion disc to determine the nature of the compact object itself. The spectrum of the emitted radiation is characterised by the radiation temperature, equal to:

$$T_{rad} = \frac{h\nu}{k}, \tag{1.3}$$

[1]Gravitational constant $G \approx 6.67 \times 10^{-8} g^{-1}$ cm^3 s^{-2}
[2]Speed of light c $\approx 3 \times 10^{10}$ cm/s
[3]Solar mass $M_\odot \approx 2 \times 10^{33}$ g

where $h\nu$ represents the energy of a typical photon, ν is the photon frequency, h and k are the Planck[4] and the Boltzmann[5] constants, respectively.

For an accretion luminosity L_{acc}, if each ring of the disc radiates as a blackbody, the temperature of the source is:

$$T_{bb} = \left(\frac{L_{acc}}{4\pi R^2 \sigma} \right)^{1/4} \tag{1.4}$$

If the gravitational potential energy of the accreted material is turned entirely into thermal energy, for each proton-electron pair accreted the temperature T_{th} is

$$T_{th} = \frac{GMm_p}{3kR} \tag{1.5}$$

where GMm_p/R is the potential energy released and $2 \times \frac{3}{2}kT$ is the thermal energy.

In general, the radiation temperature can be expected between the thermal and blackbody temperature, namely

$$T_{bb} \lesssim T_{rad} \lesssim T_{th}. \tag{1.6}$$

Using the typical values for a neutron star (M = 1.4 $M_\odot$ and $L_{acc} \sim 10^{36}$ erg/s) the result is 1 keV $\lesssim h\nu \lesssim$ 50 MeV. Similar results hold for stellar-mass black holes. These objects emit in the X-ray band and some sources also in that γ-ray band. For a white dwarf, with M = 1 $M_\odot$ and $L_{acc} \sim 10^{33}$ erg/s, the radiation temperature is within the range 6 eV $\lesssim h\nu \lesssim$ 100 keV. Accreting white dwarfs should be optical, ultraviolet and X-ray sources (Frank et al. 2002).

1.1.2 The Eddington limit

As seen from eq. 1.1, for a given value of the compactness M/R, the luminosity of a system depends on the accretion rate. This can lead to the existence of an upper threshold, which XRBs can reach, corresponding to the point where the radiation produced through accretion has enough energy to prevent matter to be accreted any further: this threshold luminosity is called the Eddington luminosity (L_{Edd}) or Eddington limit. In order to derive the standard analytical expression for such limit, a few approximations must be

[4]Planck constant $h \approx 6.63 \times 10^{-27}$ erg/s

[5]Boltzmann constant $k \approx 1.38 \times 10^{-16}$ erg/K

made:

- mass accretion is stationary and isotropic;
- matter is considered as composed of completely ionised hydrogen;
- matter and radiation interact only through Thomson scattering.

Since Thomson scattering has the lowest cross-section among the other typical matter-radiation interaction processes, the Eddington limit represents indeed an upper limit. It is the solution of the hydrostatic equilibrium equation, where the outward force, given by the radiation pressure, is equal to the inward force, given by the gravitational attraction.

In such assumptions, we assume that the radiation pressure is exerted mainly on free electrons, through Thomson scattering, since the Thomson cross-section depends on m^{-2} ($\sigma_T = 6.7 \times 10^{-25}\mathrm{cm}^2$). On the other hand, the gravitational force acts mainly on protons, since $m_p >> m_e$, and thus $GM(m_p + m_e)/r^2 \cong GMm_p/r^2$.

Putting into equation the outward force, obtained by multiplying the radiation pressure ($L/c4\pi R^2$) by σ_T with the gravitational force, the following equation can be obtained:

$$L_{Edd} = \frac{4\pi GMm_p c}{\sigma_T} \approx 1.38 \times 10^{38} \frac{M}{M_\odot} \text{ erg/s}. \tag{1.7}$$

In principle, there should be no accreting systems in excess of this luminosity. In practice, it is possible to exceed the limit by breaking spherical symmetry or with strong magnetic fields (which can suppress the electron scattering cross-section).

1.1.3 Mass transfer in binary systems

In order for matter to be accreted onto the compact object, the companion star has to transfer mass; following the approach outlined in Frank et al. (2002), there are two fundamental reasons for which there is a mass transfer: (1) the emission of stellar wind and (2) the so-called Roche lobes overflow (RLOF), where the outer layers of the companion star are stripped by the compact object (see Fig. 1.1).

X-ray binary systems with compact stars accreting from the stellar wind are defined high-mass X-ray binaries (HMXBs) due to the presence of a young massive companion powering the wind and are likely to be found in regions where recent star formation

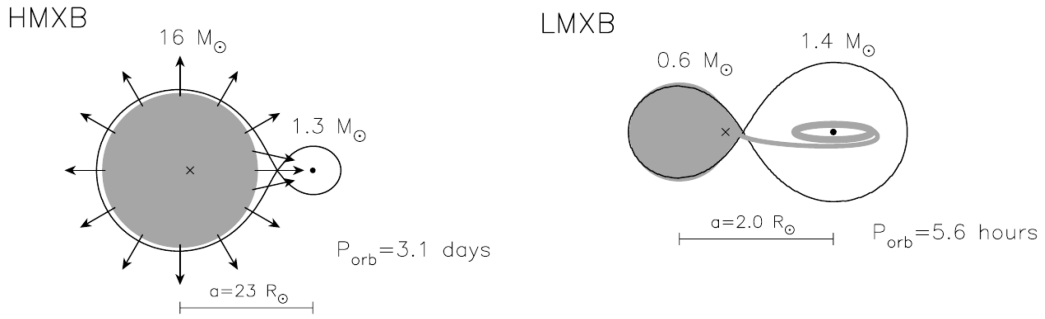

Figure 1.1: Examples of a typical HMXB (left) and LMXB (right). The neutron star in the HMXB is fed by a strong high-velocity stellar wind and/or by beginning atmospheric Roche-lobe overflow. The neutron star in an LMXB is surrounded by an accretion disk which is fed by Roche lobe overflow (Tauris & van den Heuvel 2006).

has occurred (Grimm et al. 2002). On the other hand, systems accreting via RLOF are classified as low-mass X-ray binaries (LMXBs, see Section 1.1.4).

1.1.4 X-ray binaries classification

Nowadays, the scientific community knows that binary systems are among the most common sources of X-rays in the Galaxy and form a very heterogeneous sample of objects. As already mentioned, these systems are composed of a compact object (NS, BH or WD) called primary star, accreting matter from a companion star, defined secondary star, that can be observed in the optical. The accreted mass, which is transferred by the companion star, is accelerated to extremely high velocities up to a fraction of the speed of light. When the matter reaches the surface of the compact object, it is rapidly decelerated by radiation and the (free-fall) kinetic energy radiated away as heat which can power an X-ray source.

A first criterion exists according to the nature of the primary star: systems hosting a BH or a NS are called X-ray Binaries (XRBs) and systems with WDs are called cataclysmic variables (CVs). CVs show irregular and dramatic changes in luminosity, especially in the optical energy band. Instead, on the basis of the mass of the companion star, XRBs consist of two classes: High Mass X-Ray Binaries and Low Mass X-Ray Binaries, which are described below.

High Mass X-Ray Binaries

High Mass X-Ray Binaries (HMXBs) are relatively young objects ($\lesssim 10^7$ yr), mostly distributed on the Galactic plane. They contain an early-type O or B star (> 10 $M_\odot$) which, through a strong stellar wind, expels part of its mass that is captured by a compact object (NS or BH), emitting strongly in X-ray band. Moreover, NS HMXBs can have strong magnetic fields, with $B \sim 10^{12}$ G, and usually display coherent pulsations in X-rays (i.e. narrow spikes in their X-ray power spectra). This is possible if the magnetic and rotation axes of the neutron star are misaligned. Their X-ray spectrum is hard with blackbody temperatures of a few keV and sometimes shows X-ray eclipses, due to the obscuration of the donor star, if they are viewed at moderate-to-high inclination angles with the disc axis (Bhattacharya & van den Heuvel 1991).

Low Mass X-Ray Binaries

The second class, called Low Mass X-Ray Binaries (LMXBs), consists of a solar-like or sub-solar companion star with a mass $\lesssim 1$ $M_\odot$. Accretion process can only occur through Roche lobe overflow since companion stars are unable to emit strong stellar winds. LMXBs are among the oldest systems in the galaxy ($\sim 10^{9-10}$ yr), in fact, they are associated with late-type stars and are sometimes found in Globular Clusters. NSs in LMXBs have weak magnetic fields with $B \sim 10^{8-9}$ G. Only a minority of these sources are X-ray pulsators; a small group of them form the class of the so-called Accreting Millisecond X-ray Pulsars (AMXPs) which are characterised by very short spin periods.

Ultraluminous X-ray Sources

A subclass of XRBs is represented by Ultraluminous X-ray sources (ULXs), objects that are found in galaxies outside the nuclear region, characterised by an X-ray luminosity greater than Eddington's luminosity for a stellar-mass BH ($L_X = 10^{39-41}$ erg/s). ULXs are mainly associated with star-forming regions in spiral and irregular galaxies.

ULX spectra, which peak in the X-ray band, typically show a strong curvature in the $\sim$ 2–10 keV band, before turning over to a steep spectrum at high energies, with spectral slopes of $\Gamma \sim 3$ (Bachetti et al. 2013). Since these sources are the subject of this thesis, they will be described in detail in a separate chapter (see Chapter 2).

1.2 The *XMM-Newton* observatory

In this thesis, I study the evolution of the accreting systems and the physics of their accretion with X-ray spectroscopic observations.

The following section describes the main characteristics of the instruments on board the *XMM-Newton* telescope and the procedure I applied for data reduction. In particular, I focus on the *European Photon Imaging Camera* (EPIC, see Turner et al. 2001 and Strüder et al. 2001). Further detail on *XMM-Newton* can be found on ESA website. [6]

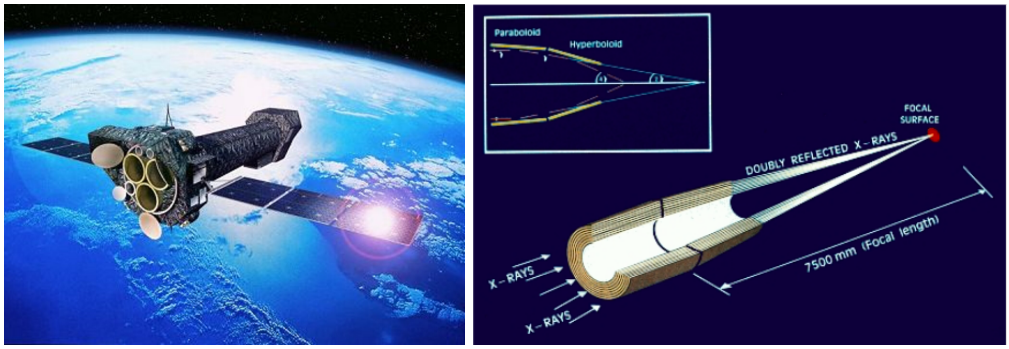

Figure 1.2: *Left*: Artistic view of *XMM-Newton* (Credit: ESA). *Right*: Schematic representation of mirrors in Wolter I configuration. It consists of an elliptical mirror (or a parabolic mirror in the case the source is very distant) followed by a hyperbolic mirror. (Credit: https://www.cosmos.esa.int/web/xmm-newton)

The **X-ray Multi-Mirror Mission** (*XMM-Newton*) is an X-ray satellite developed by the European Space Agency (ESA) and launched by Ariane 504 on 10th December 1999. Scientific operations are managed by the *XMM-Newton* Science Operations Centre (SOC), located at the European Space Astronomy Centre (ESAC) in Villafranca, Spain. The *XMM-Newton* Observatory carries three telescopes, each of them is composed of a system of 58 coaxial and confocal mirrors with grazing incidence disposed in configuration Wolter I (see Figure 1.2).

The observatory is composed of three main instruments, which are presented in more detail in the following.

- The **European Photon Imaging Camera** (EPIC, Strüder et al. 2001, Turner et al. 2001) allows extremely sensitive imaging observations over the telescope's field

[6] https://www.cosmos.esa.int/web/xmm-newton.

of view of 30 arcmin and in the energy range 0.2–12 keV with moderate spectral (E / ΔE = ~ 20–50) and angular resolution (Point Spread Function, PSF: 6 arcsec Full Width Half Maximum, FWHM)

- Two **Reflection Grating Spectrometers** (RGS, Brinkman et al. 1998, den Herder et al. 2001, designed to achieve high resolution spectroscopy (E / ΔE ≈ 100–500, for the first order) over the range 0.33–2.5 keV;
- The **Optical Monitor** (OM, Mason et al. 2001) is a telescope with a diameter of 30 cm and focal length of about 3.8 m, which operates in the band 180–600 nm allowing image and spectral analysis.

XMM-Newton mirrors have a focal length of 7.5 m. In their focal plane, there are two MOS and one pn detector which provide the highest effective area in the 0.3–10 keV energy band, which is equal to 4650 cm^2 in total.

In table 1.1, the main characteristics of *XMM-Newton* are reported. In particular, during my work I used data extracted from EPIC, thanks to its highest effective area; therefore I focus my attention on this camera in the following paragraphs.

Table 1.1: Main characteristics of *XMM-Newton*'s instruments.

	PN	MOS	RGS	OM
Passing band	0.2-12 keV	0.2-12 keV	0.3-2 keV	180-600 nm
Field of view (arcmin)	30	30	~ 5	17
PSF[1] (arcsec)	6/15	5/14	-	1.4/2.0
Dimension of pixels	150 μm (4.1")	40 μm (1.1")	81 μm	1"
Timing resolutions (ms)	0.03	1.75	600	500
Spectral resolution[2]	80 eV	70 eV	0.04 Å	180 nm

[1] FWHM/HEW. [2] At 1 keV. The temporal resolution reported is the best one for each instrument, namely *timing mode* for MOS and pn, *high time resolution mode* for RGS and *fast mode* for OM.

1.2.1 EPIC

The EPIC camera is composed of three Charge-Coupled Device (CCD) cameras, two Metal Oxide Semiconductors (MOS) and one pn. In addition, *XMM-Newton* hosts

the EPIC Radiation Monitor (ERM), which detects the radiative belts and solar flares to give particle environment information for the correct operation of the EPIC camera. Each one of the two MOS cameras is constituted by 7 MOS-CCDs, while the pn camera is constituted by 12 pn-CCDs (see Fig. 1.3). There are four different filters (*thin1, thin2, medium, thick* that can be used according to the presence of bright sources in the field of view, (FOV)) and a calibration source in each EPIC camera.

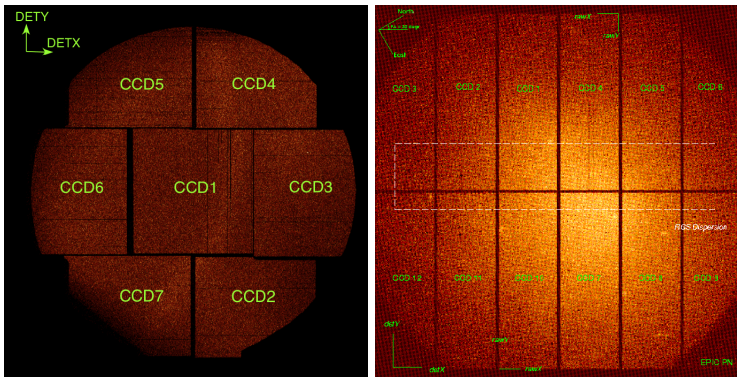

Figure 1.3: Disposition of the MOS (left panel) and pn CCDs (right panel) onboard *XMM-Newton* (Credit: https://www.cosmos.esa.int/web/xmm-newton).

EPIC MOS

As already mentioned in Section 1.2.1 each camera is characterised by seven front-illuminated CCDs in the focal plane, working in the energy range 0.2–12 keV. There is a central CCD at the focal point on the optical axis of the telescope, while the other six are at a distance of 4.5 mm towards the mirror, to approximately reproduce the focal plane curvature. With an imaging area of $\sim$ 2.5 cm $\times$ 2.5 cm each, the mosaic of the seven CCDs covers the entire focal plane (62 mm in diameter, equivalent to 28.4 arcmin).

Table 1.2 shows all the possible settings with the corresponding time resolution.

EPIC PN

The monolithic fabrication of 12 individually pn-CCDs (3x1 cm^2) on a single wafer, guarantees the spatially uniform detector quality over the entire field of view. Because of redundancy reasons, the focal plane, namely each of the four individual quadrants, is

composed of three pn-CCDs sub-units, with a format of 200×64 pixels, which operated in parallel.

Different settings for EPIC / pn are also available to improve the temporal resolution (more details are in Table 1.2).

Table 1.2: Characteristics of different settings for the MOS and pn detectors.

	Time resolution	
	MOS	pn
Full Frame	2.6 s	73.4 ms
Extended Full Frame	-	199.1 ms
Large Window	0.9 s	47.7 ms
Small Window	0.3 s	5.7 ms
Timing [1]	1.75 ms	0.03 ms

[1] Timing mode allows for better temporal resolution but it involves the loss of information on a spatial dimension for the image.

1.2.2 Data reduction

The *XMM-Newton* data is generally private to the prime investigator during the first year from the observation date, after which it becomes public and available to the entire community. All the public and private data can be found on the *XMM-Newton Science Archive* (XSA) archive[7]. After the download, the datasets are processed using a standard pipeline software called *Science Analysis System* (SAS, more information is available on https://www.cosmos.esa.int/web/xmm-newton) and the latest available calibration files (CCF) retrieved from https://www.cosmos.esa.int/web/xmm-newton/ccf-release-notes. SAS is a collection of tasks, scripts and libraries, specifically designed to reduce and analyse data collected by the *XMM-Newton* observatory. The method of data reduction depends on the instrument; the reduction procedure for EPIC detectors is explained below.

XMM-Newton data are available in two formats:

- Observation Data Files (ODF), namely reformatted telemetry in FITS format;

[7] http://nxsa.esac.esa.int/nxsa-web/

- Pipeline Processing System (PPS), a collection of validated, top-level scientific products generated at the *Survey Science Center* (SSC)[8].

Reprocessing and filtering

At first, pn data are reprocessed using the task `epproc` and MOS data are reprocessed using the `emproc` task (alternatively, there are also other tasks such as `epchain` and `emchain`).

The calibrated and concatenated event lists are filtered for high background epochs to acquire good time intervals (GTI) as follows. For each data set and each instrument, the high energy light curve (including events between 10–12 keV) is extracted to identify intervals of flaring particle background and a suitable threshold (typically 0.35 and 0.40 ct/s for MOS and pn, respectively), which is above the low steady background, is chosen to create the corresponding filtered EPIC event list.

As recommended, only events of PATTERN ≤ 4 (single/double) are usually accepted for EPIC-pn data, and events of PATTERN ≤ 12 (single-quadruple) are accepted in EPIC-MOS datasets to avoid instrumental effects and cosmic rays.

Afterwards, to select the source and region background, the images of the pn and MOS exposures are extracted, using the task `evselect`, in the 0.3–10 keV energy range. The source regions are typically circles with a radius of 20–30 arcsec, while the corresponding background regions are usually chosen larger in a nearby region on the same chip, avoiding chip gaps and free from contaminating sources. The background region should also not generally be located in the "copper ring" on the pn chip where further instrumental effects occur (Lumb et al. 2002).

The task `arfgen` is used to reproduce the effective area of the instrument (which converts the count rates into fluxes) and to correct instrumental factors, such as bad pixels and bad columns, using calibration information. The response matrix, which describes the response of the instrument as a function of energy and PI channel (Pulse-Invariant, calibrated spectral channel), is generated with `rmfgen`.

The `epicspeccombine` routine can be used to stack the EPIC spectra if required.

[8]The SSC is a consortium of 10 European institutes appointed by the ESA.

1.3 Analysis method

Source detection

In order to detect new sources in X-ray images, I performed source detection on EPIC images, using the SAS metatask `edetectchain`. This procedure allows searching for sources simultaneously in several energy bands, applying different source detection methods, with the creation of a final combined source list and the computation of sensitivity maps which contain information on the point source detection upper limits.

I ran the source detection simultaneously for pn and MOS for five energy bands: (0.2–0.5 keV (0.3–0.5 keV for pn), 0.5–1 keV, 1–2 keV, 2–4.5 keV, 4.5–12 keV). This was done with the task `edetectchain` by setting a likelihood threshold limit to the default value of 10, which corresponds to a detection threshold of $\sim 3\ \sigma$ (see Fig. 1.4).

Then, I classified the sources detected for the corresponding host galaxy, using the cross-correlation with catalogues (e.g. VizieR[9] and SIMBAD[10]) and performing spectral analysis of the brightest sources detected.

Spectral modelling

The spectrum is then analysed and fitted with theoretical models with a spectral fitting package. In this thesis, I employ two different fitting packages: XSPEC (more detail can be found in Arnaud 1996) and SPEX (see Kaastra et al. 1996).

These X-ray spectral-fitting programs are designed to be completely detector-independent so that they can be used for any spectrometer. The spectra have been extracted using data taken with the three different cameras (MOS1, MOS2, pn) in each observation. Subsequently, spectral analysis has been performed by fitting the spectra simultaneously from all three cameras.

In order to use the χ^2 statistics and its minimisation for models comparison, all spectra are rebinned to a minimum of 25 counts for the energy bin.

[9] https://vizier.unistra.fr/viz-bin/
[10] https://simbad.unistra.fr/simbad/

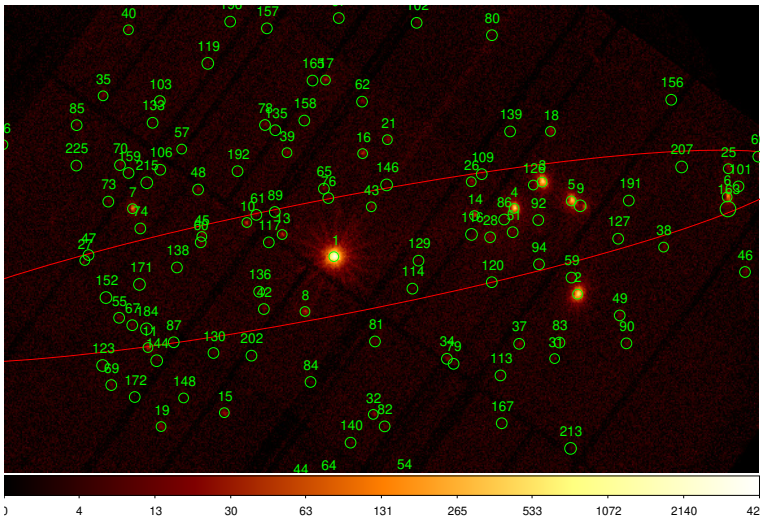

Figure 1.4: Example of source detection for the *XMM-Newton* stacked image of NGC 55 (ObsID 0864810101). Circles with 10″ radii are drawn around the X-ray sources detected and the colour bar shows the number of counts. The red line is the D_{25}, i.e. the operational definition of the galaxy diameter (where μB(B) = 25.0 mag/arcsec^2 isophote).

Timing techniques

Another important technique to study ULXs and, in general accreting compact objects, involves taking advantage of the time variability of the emitted radiation. Variability, associated with flux variations of the light curve, is a fundamental piece of information to probe the physical properties of the ULXs and the accretion disc. In XRBs, the variability time scales can be as short as a few milliseconds, which is a solid proof that the X-ray emitting source is very small, e.g. less than 1000 km. A useful tool to study this variability is the Fourier analysis of X-ray time series (see Uttley et al. 2014 for a review of spectral timing techniques). The key advantage of studying in the frequency domain is that various processes that contribute to the total variability at different time scales (or frequencies) can easily be disentangled.

Let us consider two time series, at first, the power spectrum of each sample is extracted. It describes the average variance per unit frequency of a signal at a given temporal frequency f, and it is defined as the square of the real part of the Fourier amplitudes of a single evenly sampled time series.

Instead, using the cross-spectrum (CS), it is possible to compare the variability that

occurs simultaneously in different energy bands. The CS between two light curves is defined as follows:

$$C_{xy,j} = X_j Y_j^* \tag{1.8}$$

where X_j and Y_j are the Fourier transforms of the light curves and the * denotes the complex conjugate. In order to reduce the effects of the noise, I calculate the averaged cross spectrum from a light curve by splitting it into several segments, Fourier-transforming each segment and then averaging the resulting cross spectra.

The argument of the complex cross-spectrum vector represents the phase of the resulting binned cross-spectrum $\phi(\nu_j)$, which gives the average phase lag between the two light curves in the ν_j frequency bin. The time lag is calculated by taking the phase lag ϕ and τ, as following:

$$\tau_j = \frac{\phi_j}{2\pi\nu_j} \tag{1.9}$$

for a phase angle ϕ_j derived from the argument of the complex cross spectrum and a midbin frequency ν_j.

Afterwards, we calculate the coherence γ^2 to measure the degree of linear correlation between the two light curves as a function of Fourier frequency. As defined by Vaughan & Nowak 1997, the coherence is calculated from the cross-spectrum as below:

$$\gamma_j^2 = \frac{|C_{xy,j}|^2}{C_{x,j} C_{y,j}} \tag{1.10}$$

Here, $C_{xy,j}$ corresponds to the averaged cross-spectrum, and $C_{x,j}$ and $C_{y,j}$ correspond to the analogous squared amplitudes of the power spectrum for each individual light curve.

1.4 Contents and aims of the thesis

The main scope of my PhD thesis is to improve our understanding of the physics that governs a certain regime of matter accretion known as super-Eddington accretion. This occurs when a compact object accretes matter from a companion star at a rate that exceeds the Eddington limit, which is set by the mass of the compact object. Such an extreme regime is not unusual in the Universe as it occurs at stellar-mass scales in accreting X-ray binaries (particularly in ULXs) and at supermassive scales in active

galactic nuclei such as in some Narrow Line Seyfert 1 galaxies (Collin & Kawaguchi 2004) and Tidal Disruption Event (Wu et al. 2018).

Despite decades of studies, the physics of super-Eddington accretion is not yet well understood. Moreover, the number of ULXs per galaxy and the duration of the ULX state are still highly uncertain. The detection and the study of new ULXs could improve our understanding of the contribution of these systems to the accreting binary population and the role of super-Eddington accretion in the evolution of the binary system and local feedback onto the star formation. ULXs represent among the best candidates to investigate the accretion above Eddington and are therefore the subject of this thesis.
This thesis is structured as follows:

- **Chapter 2** summarises the main properties of ULX astrophysics, with a broad description of timing and the X-ray spectral properties, multi-wavelength studies and population properties.

- **Chapter 3** reports the identification of a new (transient) ULX candidate. This source reaches and surpasses the 10^{39} erg/s threshold in multiple epochs, thus revealing its ULX nature. The work has been published in the following paper:
  Robba, A., Pinto, C., Pintore, F., et al. 2021, *"A transient ultraluminous X-ray source in NGC 55"*, Monthly Notices of the Royal Astronomical Society, Volume 515, Issue 4, pp.4669-4674.

- **Chapter 4** shows the evolution of the pulsar ULX NGC 1313 X-2 for which I found that the spectral components deviate from the L–T^4 in agreement with an expansion of a super-Eddington disc around a stellar mass compact object. These results were published in the following paper:
  Robba, A., Pinto, C., Walton, D. J., et al. 2021, *"Broadband X-ray spectral variability of the pulsing ULX NGC 1313 X-2"*, Astronomy and Astrophysics, 652, A118.

- **Chapter 5** presents the study of the variability properties of the pulsar ULX NGC 1313 X-2, which are used as diagnostic of the accretion rate of the source. The work uses a different approach than the one in Chapter 4 and will be published in Robba, A., De Marco, B., Pinto, C. et al (*in prep*).

- **Chapter 6** summarises the results of this thesis and provides some implications in the research field as well as prospects for future work.

2

Ultraluminous X-ray sources

This Chapter provides the state of art for the research field regarding the class of X-ray sources known as Ultraluminous X-ray sources, that are of great interest in astrophysics. They are binary systems, generally with a BH or a NS as the compact object, and characterised by a luminosity $>10^{39}$ erg s^{-1}. The study of the ULXs allows us to investigate the accretion phenomena near and above the Eddington limit. This is also relevant in the cosmological context because it may provide further knowledge onto the growth of the primordial supermassive black holes.

2.1 ULXs: a different group of sources

The first ULXs were discovered by the Einstein Observatory in 1981, which allowed us to obtain the first resolved images of external galaxies (Giacconi 1981). However, the low spatial resolution of this telescope led to confusing some of them with Galactic stellar-mass BH candidates discovered in the same years. In addition, the lack of long-term monitoring has made it difficult to detect them.

Subsequently, new satellites were used, such as *ROSAT* and *ASCA*, characterised by a higher spatial resolution. Through these ones, it was possible to discover that some of these sources had apparent luminosities above the Eddington limit of the typical Galactic stellar-mass BHs. With the era of *Chandra*, *XMM-Newton*, *Suzaku* and *Swift* it was possible to make ground-breaking discoveries, develop new spectral X-ray models and new studies of timing properties and of the counterparts of these enigmatic sources

at different wavelengths.

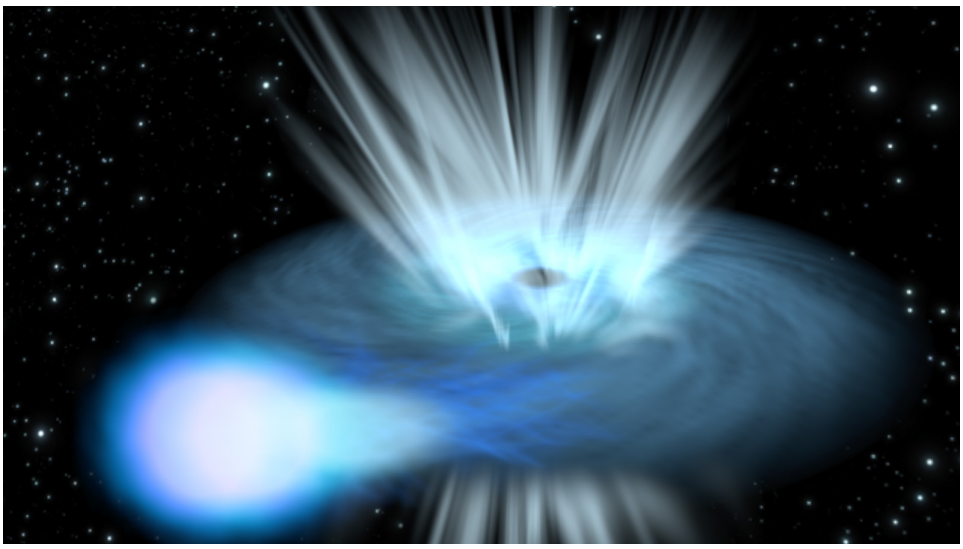

Figure 2.1: ULX artistic image: a compact object feeds on a massive companion star at high accretion rates with the consequent launch of powerful winds. Credit: ESA-C. Carreau

2.2 Definition of ULXs

As already mentioned in Chapter 1, ULXs are non-nuclear sources mostly seen in nearby galaxies (particularly, in star-forming galaxies) and they are thought to be X-ray binaries powered by accretion onto a compact object (for a review see Pinto & Walton 2023). They are defined by two observational properties:

- they are point-like, off-nuclear X-ray sources with a peak emission localised in the X-ray band (i.e. not to be confused with an active galactic nucleus);
- their X-ray luminosities (under the assumption of isotropic emission) surpass the Eddington limit for a standard $10M_{\odot}$ stellar-mass black hole ($L > 10^{39}$ erg/s).

By considering also that, in rare cases, ULXs can reach a few times 10^{41} erg/s, they represent the most extreme amongst XRBs and ideal targets to study super-Eddington accretion. ULXs show very different behaviours and some of these sources show strong X-ray variability, both in the short and long timescales.

2.3 ULX catalogues

The first *ROSAT*/HRI catalogue of non-nuclear X-ray sources, created by Colbert & Mushotzky (1999), has been important for classifying ULXs, but afterwards, more detailed X-ray source catalogues have been produced through a re-analysis of the *ROSAT*/HRI archive data (e.g. Roberts & Warwick 2000, Colbert & Ptak 2002, and Liu & Bregman 2005). Thanks to these works, it has been possible to study these objects, their properties and their relation to their host galaxies. This led to longer and more focused observations with *Chandra* (Kovlakas et al. 2020) and *XMM-Newton* (Earnshaw et al. 2019). One of the most recent catalogues is Walton et al. (2022), which uses the combination of two decades of observations with *Chandra*, *XMM-Newton* and *Swift*, resulting in ~ 1800 ULX candidates in ~ 950 host galaxies, with an average distance of D = 74.7 ± 2.7 Mpc.

2.4 The nature of the compact object

In order to explain the high luminosities of these sources, which nowadays we know to depend mainly on the accretion rate, several hypotheses have been proposed.

In the past, it was speculated that the extreme luminosities exhibited by ULXs were produced by black holes with masses in the range $10^2\,M_\odot \lesssim M \lesssim 10^4\,M_\odot$, called intermediate-mass black holes (IMBHs), which accrete at sub-Eddington rates (Taniguchi et al. 2000). This hypothesis has been supported by the discovery of a cool disc component (with temperatures ~ 0.1 keV) in the ULX spectra. Among the different models for the IMBH formation, the rapid merging of stellar-mass black holes in globular clusters (Miller 2002), or of stars in dense clusters (Portegies Zwart & McMillan 2002), have been proposed.

An alternative scenario invoked extreme geometrical beaming in Eddington limited stellar-mass BH (King et al. 2001). Among the most accepted hypotheses for the nature of the ULXs is that they are powered by super-Eddington accretion onto such objects. There are multiple arguments for this explanation (see Section 2.5).

The ULX field was revolutionised after the detection of X-ray pulsations in such systems, which represents the strongest evidence of super-Eddington accretion onto neutron stars. Neutron stars form an unknown, but likely significant fraction of the ULX

population given that pulsations were found in about 20% of the ULXs with sufficiently sensitive data (Rodríguez Castillo et al. 2020).

2.5 X-ray spectral properties of ULXs

Historically speaking, ULX spectra have typically been compared to the spectral states that are often seen in Galactic black hole XRBs (see Fig. 2.2).

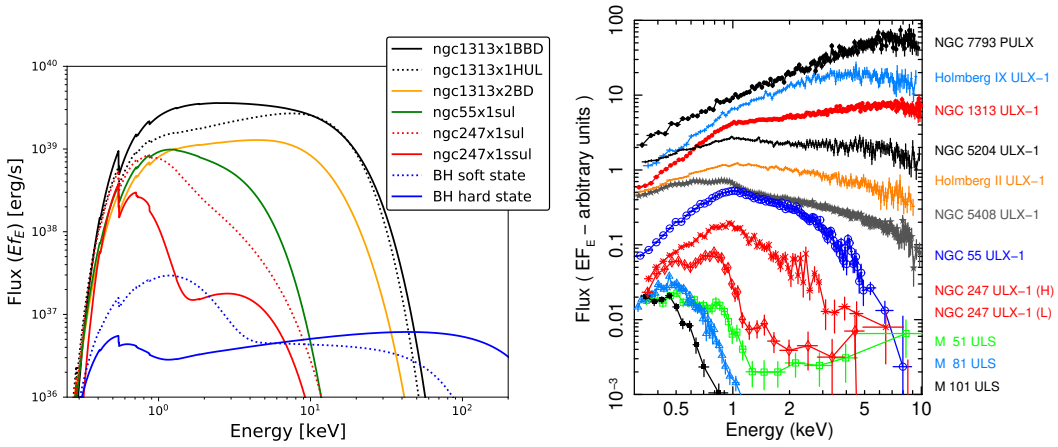

Figure 2.2: *Left:* Comparison between typical spectra of ULXs and Galactic BH binaries. ULX spectra are divided into several classes: hard (HUL), soft (SUL), supersoft (SSUL or ULS) and broadened disc (BD) (as defined by Sutton et al. 2013). *Right:* X-ray spectra of some among the brightest ULXs with the hardness increasing from the bottom to top (Pinto & Walton 2023).

Thanks to *Chandra*, *XMM-Newton* and *NuSTAR*, even more detailed studies of the ULX spectra have been made possible. This was achieved, in the 0.3–10 keV energy band, by combining the large effective area of *XMM-Newton* with spatially resolved observations with *Chandra*. High energy coverage was achieved thanks to the launch of *NuSTAR* (which covers 3–78 keV). Owing to their distinct spectral appearance, comparisons between ULX spectra and the standard sub-Eddington accretion states have become largely obsolete. Observations with high signal-to-noise and good energy resolution provided a "canonical" picture of ULX X-ray spectra (see Fig. 2.3).

With the improvement in data quality, single-component spectral models were excluded, suggesting the presence of a soft excess (below $\sim$ 2 keV) and a break to very

steep spectra (above $\sim$ 10 keV).

Based on the spectral morphologies observed by Gladstone et al. (2009), ULXs are now mostly interpreted as a new, super-Eddington accretion state, called the ultra-luminous state. Depending on the different spectral properties that the ULX population exhibits in the 0.3–10 keV band, they are empirically divided into four main classes or regimes (Sutton et al. 2013):

- **Hard ultra-luminous** (HUL) – the spectra required two spectral components, modelled with a cool accretion disc and a dominant higher energy power law with slope $\Gamma < 2$.

- **Soft ultra-luminous** (SUL) - the spectra are distinctly two-component as HUL, modelled with a cool and stronger accretion disc (with $kT \sim 0.1 - 0.3$ keV) and a power law with $\Gamma > 2$.

- **Broadened disc** (BD) - the spectra appear too broad to be fitted by a single thermal component, such as the standard thin accretion disc. Instead, they tend to be well fitted by the advection-dominated disc with $kT_{in} \sim 1 - 2$ keV and p $\sim 0.5 - 0.6$ (p = 0.75 for a standard thin disc, where p follows the law $T(R) \propto R^{-p}$)).

- **Supersoft ultra-luminous** (SSUL or ULS) - these spectra are mainly dominated by a cool blackbody-like component, with $kT \sim 0.1$ keV, contributing over 90% of the flux, and a fainter hard component, with $\Gamma = 2 - 4$.

Depending on the view angle, different spectral properties are observed. As we can see in Fig. 2.3, for such a geometry, the inner regions of the accretion disc are expected to be both geometrically and optically thick and to launch powerful outflows.

In the framework of the super-Eddington accretion, the hardest X-rays are produced in the innermost (and hottest) regions of the accretion system by either a Comptonised corona (in the case of a black hole accretor) or by an accretion column (in the case of a magnetised neutron star accretor). The 0.3–10 keV spectra are usually modelled by two thermal components. A softer component, which is usually described by a simple blackbody (DISKBB or DBB, in XSPEC and SPEX respectively) or an advection dominate disc (DISKPBB, where p = 0.75), with a temperature of $\sim$ 0.2 keV. It is thought to likely originate from the outer, Eddington-limited part of the accretion disc, or in an optically

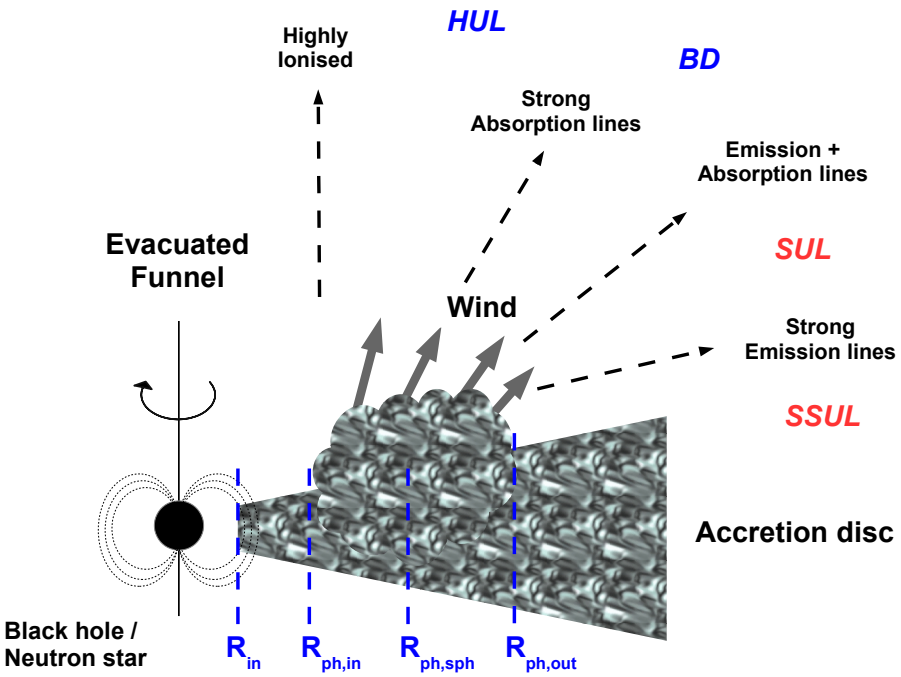

Figure 2.3: The picture represents a toy model of ULXs in supercritical accretion. Strong outflows, around the inner region of the accretion flow, are propelled by the radiation pressure (Credit: Pinto & Walton 2023).

thick outflow. The hotter of the two components, with a temperature around 1–2 keV is usually associated with the inner, super-Eddington part of the accretion disc.

In this scenario, we expect to observe hard spectra at low inclinations (i.e. along the disc axis), a softer spectrum with strong absorption lines from the wind at moderate inclinations and, at high inclinations, a significantly absorbed continuum with strong emission lines implying a supersoft spectrum.

2.6 High-resolution X-ray spectroscopy

Evidence for atomic spectral features in the soft band below 2 keV (especially near 1 keV) has been found in multiple ULXs (Stobbart et al. 2006) and with different instruments (like *XMM-Newton* and *Chandra*), using continuum models. There is a substantial similarity in the shape of these residuals for several ULXs with high signal-to-noise spectra and an anti-correlation between their strength and the X-ray spectral

hardness (Middleton et al. 2015b).

The resolving power of CCD spectra ($R = E/\Delta E \lesssim 20$ around 1 keV) was not sufficient to resolve them. This was achieved thanks to the use of instruments with higher energy resolution, such as *XMM-Newton*/RGS ($R \sim 100$–600, in the 0.3–2 keV band). The features near 1 keV and, later on, in the Fe K band at 8–9 keV were resolved in a forest of rest-frame emission and blueshifted lines (Pinto et al. 2016, Walton et al. 2016). The absorption lines, in particular, unveiled the long-sought ultrafast ($\gtrsim 0.1c$) outflows (UFOs) as evidence of strong radiation pressure in ULXs. Kosec et al. (2018b), interestingly, found the first evidence of UFOs in the pulsating NGC 300 ULX-1, implying a non-magnetar magnetic field. An in-depth study of Kosec et al. (2021), using a sample of 19 ULXs, showed that rest-frame emission lines and blue-shifted absorption lines are ubiquitous features but more frequent in SUL spectra in agreement with the overall picture for which the continuum is progressively absorbed at higher inclinations with a spectral softening and manifestation of spectral lines (see Fig. 2.3).

2.7 Timing properties

X-ray timing properties offer a great opportunity for understanding the physical nature of ULXs, but extensive monitoring campaigns are needed for long-term timing analysis. Variability properties are often characterised via Fourier timing techniques, which are powerful tools for investigating in a model-independent way the geometry of accretion discs, the size scales involved, and the nature of the compact objects. They have revealed variations on short timescales (e.g. broadband noise, pulsations and quasi-periodic oscillations) and on long timescales (periodicities could be associated with orbital or super-orbital variability). Below I provide some relevant examples.

2.7.1 Pulsations

Following the discovery of coherent pulsations from M82 X-2 (Bachetti et al. 2014), it was understood that some of these systems host neutron stars, forming a new class called *Ultraluminous X-ray pulsars* (PULXs). To date, there are 6 persistent ULXs that are known to be pulsars: NGC 5907 ULX-1 (Israel et al. 2017a), NGC 7793 P13 (Fürst et al. 2016, Israel et al. 2017b), NGC 300 ULX (Carpano et al. 2018), NGC 1313 X-2

(Sathyaprakash et al. 2019) and M51 ULX-7 (Rodríguez Castillo et al. 2020). Although it is plausible to suggest that a significant fraction of all ULXs might contain a NS as a compact object.

In addition to these sources, there are a similar number of transient X-ray binaries hosting neutron star accretors that occasionally peak just above 10^{39} erg/s whilst in outburst, and so could also formally be considered ULX pulsars (e.g. Skinner et al. 1982, Wilson-Hodge et al. 2018 and Vasilopoulos et al. 2020).

The first pulsation from a ULX was discovered in M82 from Bachetti et al. (2014) with *NuSTAR* observations. The source, which is responsible for the signal of average period 1.37 s with a 2.5 day orbital modulation, is M82 X-2, an X-ray source characterised by a peak of luminosity above 10^{40} erg/s (in the 0.3–10 keV band).

However, the vast majority of the ~ 1800 known ULXs in the nearby galaxies (Walton et al. 2022) do not have sufficient data quality for deep pulse searches.

PULXs typically show similar temporal and spectral properties, e.g. their sinusoidal pulse profiles which suggest that the emission is not strongly beamed. Moreover, these sources are highly variable; in fact, their luminosities vary from peaks of the order of 10^{40}–10^{41} erg/s to much weaker values below 10^{38} erg/s. The drops in the light curves of these systems could be associated to the onset of the propeller effect (Fürst et al. 2023).

2.7.2 Time delays between different energy bands

Searching for a correlation between spectral variability and time lags between different energy bands in ULXs is crucial to understanding their emission mechanism and the structure of the accretion disc. This is a very useful technique since is model-independent. Despite the low count rate and low short-term variability of most ULXs, compared to Galactic XRBs, several authors showed evidence of delays in the soft band (e.g. 0.3–1 keV) at various frequencies (see De Marco et al. 2013, Pinto et al. 2017, Kara et al. 2020 and Pintore et al. 2021) that could unveil photons reprocessing in the outer disc and further details on the disc size and the presence of optically-thick winds.

2.7.3 Cyclotron Resonant Scattering Features

Cyclotron resonant scattering features (CRSFs) are known to arise from the interaction of X-ray photons with a strong magnetic field in highly-magnetised neutron stars

(Truemper et al. 1978). These features can be used as an indicator of the accretor being a neutron star, as black holes are unable to generate such intense magnetic fields.

Due to the limited number of ULXs with high signal-to-noise ratio (S/N) broadband spectra, CRSF detections in ULXs are elusive. In Galactic X-ray pulsars cyclotron features can have a width of a few keV (indicating an electron origin rather than proton), and in some cases, they can be distinguished in spectra with moderate resolution.

2.8 Multi-wavelength studies

Multi-wavelength observations of ULXs are crucial to improve our knowledge, especially onto the nature of the donor star, the mass of the compact object, the presence of outflows and the local environments.

In the early 2000s, it was found that many ULXs are associated with an optical nebula (Pakull & Mirioni 2003) and/or radio nebula (Kaaret et al. 2004). Most of these nebulae, characterised by large extensions of $\sim$ 10–100 pc, can be powered by different phenomena. Among the major causes, originally they were thought to be mainly photoionised (Pakull & Mirioni 2003). The photoionisation is demonstrated by the presence of strong high ionisation lines, like HeII λ4686. This line is characterised by fully ionised He, which requires photons with energies in excess of 54.4 eV.

After the discovery of outflows (with a large velocity broadening, up to 150 km/s) and given the presence of shocks and lines from collision excitation (e.g. [O I] at 6300 Å), it was understood that in many cases mechanical power due, e.g., to winds or jets is actually inflating them.

Optical spectra of ULXs also show the presence of broad emission lines, characterised by widths of 500–1,500 km/s, in the Balmer series and in HeII λ4686. Caution should be used to measure radial velocity curves and to constrain the parameters of the binary system, using emission lines as they may be contaminated by disc wind emission.

Also in some cases, jets could power ULX bubbles. Indeed, evidence of jets is revealed in radio observations of some ULXs, e.g. Holmberg II X-1 (Cseh et al. 2014), M 31 ULX (Middleton et al. 2013) and NGC 7793 S26 (Pakull et al. 2010).

In the last decade, substantial work has been done in order to search for optical counterparts. They permit to obtain crucial information on the history of binary evolution, the nature of the donor star and the geometry of the disc. The optical counterpart refers

to the point-like optical source, that is spatially associated with the ULX. It could allow the measurement of radial velocity curves for the companion stars and thus unambiguous constraints on the compact object masses. However, identifying the counterparts is complicated, because these sources are very distant and therefore faint.

The best results have been obtained through the simultaneous use of *Hubble Space Telescope* (HST) for the optical image and *Chandra* for the localisation of the X-ray source. Tao et al. (2011) and Gladstone et al. (2013) succeeded in identifying unique optical counterparts for ∼ 20 ULXs. The results obtained have suggested that the companions are OB supergiants. However, the optical emission can be significantly affected by photon reprocessing occurring in the outer disc.

Given the large distances of most ULXs and since these systems tend to occupy crowded fields, there may be several optical counterparts associated with the X-ray astrometric position (e.g. Gladstone et al. 2013). Furthermore, it must be considered that the emission from the star may be contaminated by the wind photosphere depending on the accretion rate (Poutanen et al. 2007). For all these reasons, it is not easy to identify exactly the emission from the companion star.

Moreover, as shown by Fabrika et al. (2015), the spectroscopic signatures (e.g. He II emission lines in NGC 7793 P13) may also be contaminated or dominated by the wind.

2.9 Super Eddington vs sub Eddington

In the previous sections, different properties defining the population of ULXs and the proposed theoretical models have been discussed. ULXs are believed to constitute a heterogeneous class of objects, including neutron stars, black holes, or intermediate-mass black holes. A crucial question is whether these objects exhibit generic similarities, or can divide into subgroups with distinct physical, and if there are identifiable differences between them. However, despite years of research, determining the nature of the compact object in ULXs remains a challenge, due to their large distances, low statistics and, therefore, difficulty to detect pulsations.

Among the various proposed scenarios, the possibility that some ULXs are composed of IMBHs was supported by their high luminosities ($L \sim 10^{39-41}$ erg/s) and the detection of a cool disc temperature (∼ 0.1 keV) in the spectra, which is expected in the case of very massive black holes ($M \sim 10^{2-4}$ $M_{\odot}$). Moreover, a few of them exhibit quasi-

periodic oscillations (QPOs) at a hew Hz which would indeed suggest the presence of massive BHs (Pasham et al. 2015), although doubts have been raised on such association (Middleton et al. 2011).

The detection of coherent pulsations has revolutionised the field of ULXs by unequivocally identifying neutron stars in 6 classical and persistent ULXs and in 6 other transient ULXs (for a review see Pinto & Walton 2023). However, as mentioned above, the fact that only about 30 ULXs have data good enough to detect pulsations strongly suggests that a substantial fraction (if not the majority) of ULXs is actually powered by super-Eddington accreting NS. Of course, some ULXs could still host stellar-mass BHs as indicated by the detection of strong jets in some of the closest objects (Cseh et al. 2014) in analogy with the super-Eddington Galactic source SS 433 (see Hjellming & Johnston 1981, Marshall et al. 2002).

The broadband spectral shape measured in nearby ULXs with deep *XMM-Newton* and *NuSTAR* observations appears very soft, unlike the hard spectra of sub-Eddington states seen in classic Galactic XRBs, thereby disfavouring Eddington-limited accretion onto massive BHs. The very soft spectral energy distributions (SEDs) are instead in agreement with super-Eddington thick discs where Compton scattering is producing the cutoff seen around 5-10 keV.

Furthermore, this scenario is supported by the L–T trends which do not agree with the predictions for Eddington-limited thin discs ($L \propto T^4$). The flatter relationships imply a different geometry for the discs with a possible contribution from the winds (Walton et al. 2020). My thesis has focused on tackling this issue and provides further, new results (see Sect. 4).

3

A transient ultraluminous X-ray source in NGC 55

Summary

It is not easy to estimate the actual number of ULXs per galaxy, due to, e.g., their variability, transient behaviour, viewing angle and local obscuration. This is important not only to understand the binary evolution but also to estimate the contribution of ULXs to galactic feedback (especially at the peak of the star formation). For all these reasons, long-term monitoring of the host galaxies is necessary to improve the probability of detecting transient ULXs, while deep observations allow accurate measurements of the source spectral shape and luminosity.
I studied the X-ray emission from the population of X-ray sources in the galaxy NGC 55, thanks to recent *XMM-Newton* observations which were awarded to look for spectral and wind changes in NGC 55 ULX-1. In this Chapter, I report the identification of a new ULX (XMMU J001446.81-391123.48, hereafter ULX-2), which was previously reported as a transient X-ray source with a luminosity around a few 10^{38} erg/s in the 2010 *XMM-Newton* observation and, possibly, even brighter in archival *Swift* data. I demonstrated that this source unambiguously reaches and surpasses the 10^{39} erg/s threshold in multiple epochs, revealing its ULX nature.

3.1 Introduction

Ultraluminous X-ray sources (ULXs) are extragalactic off-nuclear objects with bolometric X-ray luminosities $\gtrsim 10^{39}$ erg s^{-1}, i.e. the Eddington limit for accretion onto a

10 $M_\odot$ black hole (e.g. Kaaret et al. 2017). There is a growing consensus that ULXs are mainly powered by neutron stars (NS) or stellar-mass black holes (BHs), whose radiation is mildly beamed into our line of sight by a wind-cone in a super-Eddington regime (e.g. Poutanen et al. 2007). This has been corroborated by the unambiguous discoveries of pulsations (e.g. Bachetti et al. 2014) and winds (e.g. Pinto et al. 2016) in a growing number of ULXs. Other theories have suggested that some ULXs could host intermediate-mass black holes accreting at sub-Eddington rates such as for HLX-1 (Webb et al. 2012).

Early studies of ULX properties in the X-ray energy band showed a particular spectral behaviour called as the *ultraluminous state* (Gladstone et al. 2009). Here, a strong spectral curvature is observed between 2–10 keV, which has been robustly confirmed by *NuSTAR* data (e.g. Walton et al. 2020), and often coupled with a soft excess below 2 keV. Depending on the spectral slope in the 0.3–5 keV band, ULXs are generally classified as soft (SUL, $\Gamma > 2$) or hard (HUL, $\Gamma < 2$) ultraluminous regimes (Sutton et al. 2013). In the latter case, if the X-ray spectrum has a single peak and a blackbody-like shape, it is classified as broadened disc regime.

The spectral properties have been interpreted in the framework of super-Eddington accretion where the disc is vertically inflated by the strong radiation pressure which is also responsible for launching winds (Poutanen et al. 2007). Depending on the viewing angle with respect to the edge of the wind, a certain fraction of the hard photons coming from the innermost regions are obscured (edge-on) or not (face-on) by the wind (Middleton et al. 2011). The different spectral shapes of ULXs and the observed switch from one regime to another (e.g. Sutton et al. 2013) can be explained in terms of variability of accretion rate and wind optical depth, as well as in changing of the viewing angle (e.g. due to precession, Middleton et al. 2015a). Such scenario can also explain the unpredictable temporal variability observed on short time-scales, i.e. from seconds to hours (Heil et al. 2009; Alston et al. 2021), and on longer time-scales of a few months (e.g. Fürst et al. 2018). Pulsations are mainly found in ULXs with hard spectra, which agrees with the overall picture and the need for a face-on configuration to detect them (e.g. Walton et al. 2018c).

About 500 ULXs have been found in nearby ($d \lesssim 100$ Mpc) galaxies with typically 1-2 ULXs per galaxy and a higher fraction in spirals or star forming galaxies (Swartz et al. 2011). Many ULXs are transient objects, including the ones harbouring pulsating

NS (Hameury & Lasota 2020), whilst some high-inclination sources might be obscured by gas along the line of sight such as the Galactic super-Eddington source SS 433 (Middleton et al. 2021) and thus not appear as an ULX. This means that the actual number of ULXs might be larger than currently thought.

In this work, we provide evidence for a new (the second) ULX in the galaxy NGC 55, thanks to recent *XMM-Newton* observations. The object XMMU J001446.81-391123.48 (hereafter ULX-2) was previously reported as a transient X-ray source with luminosity of a few 10^{38} erg s^{-1} (Jithesh & Wang 2015) based on archival observations with *XMM-Newton* and the Neil Gehrels Swift Observatory (hereafter *Swift*). Here we adopt a distance of 1.9 Mpc for the galaxy NGC 55, which is the average value of the recent Cepheid estimates[1].

3.2 Observations and data analysis

The galaxy NGC 55 was observed 10 times by *XMM-Newton* from 2001-11-14. We do not use the early observations 0028740101-0201 as the new ULX candidate was not detected there (Stobbart et al. 2006). For our analysis, we particularly benefited from three recent deep ($\gtrsim$ 90 ks) observations of NGC 55 (PI: Pinto). The observations were carried out with the EPIC-pn and EPIC-MOS detectors (Strüder et al. 2001; Turner et al. 2001), all operated in full frame mode and with a thin filter. For spectral and temporal analysis we used only the data provided by pn and MOS 2, since the source fell in one of the failed MOS1 chips (CCD3 and CCD6) in some observations.

Table 3.1 lists the details of the *XMM-Newton* observations that we analysed, including the date and the net exposure for each instrument.

The data analysis was performed using the *XMM-Newton Science Analysis System* (SAS) version 18.0.0 and the calibration files of January 2021. We reduced the data from the EPIC cameras, following the standard procedure. As recommended, we selected events with FLAG=0, and PATTERN $\leq$4 ($\leq$12) for EPIC-pn (MOS), respectively. Using the task `emosaic`, we extracted the stacked EPIC MOS 1-2 and pn image in the 0.3–10 keV energy range. The field of the galaxy NGC 55 and the bright X-ray sources are shown in Fig.3.1 along with the contours derived from the archival DSS [2] optical image.

[1] https://ned.ipac.caltech.edu/

[2] https://archive.stsci.edu/cgi-bin/dss_form

Table 3.1: *XMM-Newton* observations of NGC 55.

Obs.ID [(1)]	Date [(2)]	$t_{\rm exp}$ (ks) [(3)]		Count rate (10^{-2} s^{-1})	
		(pn)	(MOS 2)	(pn)	(MOS 2)
0655050101	2010-05-24	95.3	117.4	2.0	0.7
0824570101	2018-11-17	90.6	136.5	21.8	6.9
0852610101	2019-11-27	4.1	9.4	13.8	5.8
0852610201	2019-12-27	4.1	6.5	18.6	6.0
0852610301	2020-05-11	4.9	7.5	5.4	2.0
0852610401	2020-05-19	4.0	6.5	14.4	5.5
0864810101	2020-05-24	102.2	124.4	8.2	3.1
0883960101	2021-12-12	91.3	117	13.5	6.6

Notes: [(1)] observation identifier; [(2)] observation date (yyyy-mm-dd); [(3)] net exposure times are reported after removing periods of high background.

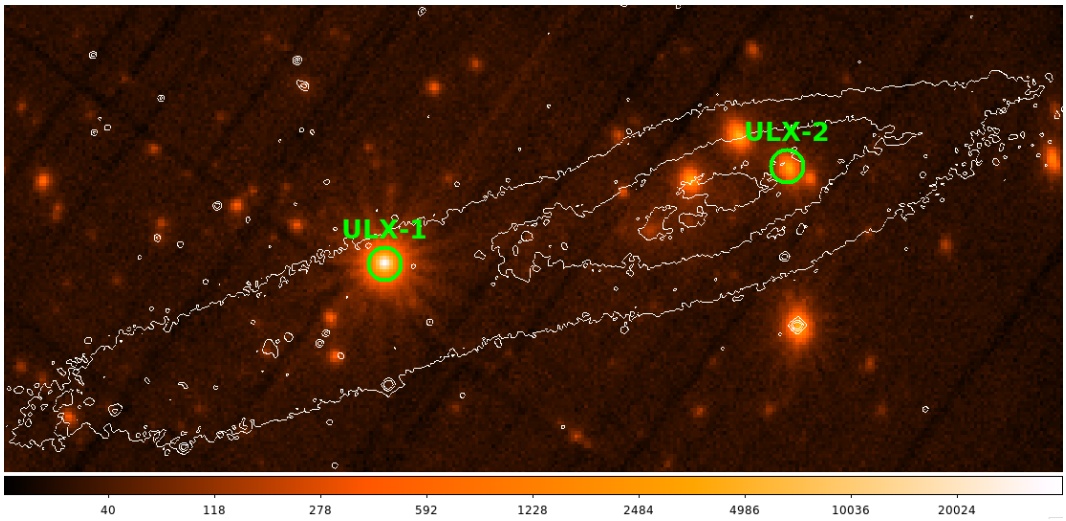

Figure 3.1: *XMM-Newton* stacked image of NGC 55. Circles with 20″ radii are drawn around the ULXs along with surface brightness contours from the filter-RG610 DSS image. The colour bar shows the number of counts.

We extracted the source and the corresponding background events from circular regions with radii of 20″ and 50″, respectively. The background region was chosen in a nearby region on the same chip, but away from any contaminating point source.

3.2.1 Source detection

Stobbart et al. (2006) reported one ULX (ULX-1) in NGC 55, using the 2001 *XMM-Newton* observations (see Fig. 3.1). To better classify the brightest sources located in this galaxy, we carried out a source detection on the recent deep *XMM-Newton* data (2018, 2020 and 2021, see Table 3.1). We ran the source detection simultaneously for EPIC-pn and EPIC-MOS for five energy bands: 0.2-0.5 keV and 0.3-0.5 keV for pn and MOS, respectively, 0.5-1 keV, 1-2 keV, 2-4.5 keV, 5.5-12 keV for both cameras. This was done with the task `edetectchain` by setting a likelihood threshold limit to the default value of 10, which corresponds to a detection threshold of $\sim 3\ \sigma$.

A detailed and thorough study of the population of X-ray bright sources in NGC 55 will be reported in a forthcoming paper. Here, we report on the remarkable X-ray variability of the source XMMU J001446.81-391123.48 (ULX-2). We detected this object in all exposures since 2010.

3.3 Spectral Analysis

We fit the *XMM-Newton* spectra with the SPEX code (Kaastra et al. 1996), over the 0.3–10 keV energy range. We only use the long ($\gtrsim$ 100 ks) observations, which provide sufficient statistics to decompose the spectrum. We decided to stack the spectra from ObsID 0824570101 and 0883960101 because the single spectra were compatible. We grouped the MOS2 and pn spectra to a minimum of 25 counts per energy bin to use χ^2 statistics, adopt 1 σ uncertainties, and fit them simultaneously.

We tested three phenomenological models to describe the inner and outer accretion flow. In the first model we used the standard thin disc model (DBB in SPEX) and a powerlaw component (POW) that are often used to model the thermal emission from the accretion disc and the Comptonised emission from the corona or the inner accretion flow, respectively (e.g. Robba et al. 2021). A second model is considered to account for dominant disc emission in very bright states. This model consists of a hot disc modified

by a coherent Compton scattering (MBB, see SPEX manual for more details) component and a cooler blackbody component (BB) describing the emission from the outer disc and/or powerful winds (e.g. Pinto et al. 2017). We finally tested a combination of the standard thin disc model (DBB) and the Comptonised emission from the corona (COMT). All continuum components are absorbed by a neutral interstellar medium, described by the HOT component (from both our Galaxy and NGC 55).

Since it is not yet clear whether the source is always sub-/super-Eddington or it shifts between different regimes we simultaneously applied the models to the three spectra coupling the parameters that are weakly constrained or that could vary due to some modelling artefact such as the column density, $N_{\rm H}$, and the optical depth, τ. However, given that most parameters are decoupled we do not expect any effects on their best-fit value. We also tested a model with the column density free to vary, obtaining consistent results albeit with larger uncertainties. The resulting value is $N_{\rm H} = (5.8 \pm 0.2) \times 10^{21}$ cm^{-2} for the fit with DBB+COMT model, which is much higher than 7×10^{20} cm^{-2} (Galactic value), suggesting further absorption in agreement with the source being in the central regions of the host galaxy. All results are shown in Figure 3.2 and Table 3.2. As we can see, sometimes we found almost indistinguishable χ^2. There is a degeneracy between different models that can fit the spectra equally well. We have attempted to fit the spectra individually freezing the $N_{\rm H}$ to the average value and found consistent results.

The DBB+COMT model provides the best description of the broadband spectra often yielding a much lower χ^2 value than the other two models. The data and the best fit model are shown in Fig. 3.2. All three models result in a slight under-prediction of the data above $\sim$ 6 keV in the brightest ULX-like spectrum, which is likely due to a hard X-ray tail as observed in many ULXs (Walton et al. 2018c). Interestingly, the brightest state (i.e. Obs.ID 0824570101+08839601) also shows residuals at 1 keV (in emission) and between 1.2-1.5 keV (in absorption) with a pattern very similar to that observed in many ULXs and resolved in a forest of emission and absorption lines produced by winds (Pinto et al. 2016, 2017).

In order to verify these spectral features, we fitted all spectra, modifying our baseline model DBB+COMT by addying a gaussian line. We fixed the energy centroid at 1 keV and the line width to 0 (only instrumental broadening, which is $>$ 1000 km/s at 1 keV). We found a Gaussian flux of $(31\,^{+9}_{-11})\times10^{44}$phot/s for the high-flux spectrum ($\Delta\chi^2 = 9$),

Table 3.2: Broadband continuum models.

Parameter	Units	0655050101	0824570101+0883960101	0864810101
		Model 1 : hot (dbb + po)		
$N_{\rm H}$	(10^{21}/cm^2)		$6.9^{+0.3}_{-0.2}$ $^{(a)}$	
Norm$_{\rm dbb}$	(10^{16} m^2)	$1.5^{+4}_{-1.1} \times 10^{-3}$	$2.8^{+1.1}_{-0.6} \times 10^{-4}$	$2.1^{+15}_{-1.8} \times 10^{-3}$
Norm$_{\rm po}$	(10^{16} m^2)	419^{+24}_{-23}	1741^{+93}_{-82}	1332^{+52}_{-48}
$kT_{\rm dbb}$	(keV)	$0.18^{+0.03}_{-0.02}$	0.37 ± 0.02	0.17 ± 0.04
Γ		$2.90^{+0.07}_{-0.06}$	1.91 ± 0.04	2.34 ± 0.03
L$_{\rm dbb,0.3-10}$ $^{(b)}$	(10^{38} erg/s)	$1.7^{+5}_{-1.3}$	15^{+6}_{-3}	$2.2^{+15}_{-1.9}$
L$_{\rm po,0.3-10}$ $^{(b)}$	(10^{38} erg/s)	2.17 ± 0.12	$10.5^{+0.6}_{-0.5}$	$6.8^{+0.3}_{-0.2}$
L$_{\rm tot,0.3-10}$	(10^{38} erg/s)	$3.9^{+3}_{-0.8}$	$25.5^{+0.5}_{-0.2}$	$15.0^{+7}_{-0.9}$
χ^2/d.o.f.		103.53/84	304.22/251	237.38/178
		Model 2 : hot (bb + mbb)		
$N_{\rm H}$	(10^{21}/cm^2)		$3.79^{+0.15}_{-0.14}$ $^{(a)}$	
Norm$_{\rm bb}$	(10^{16} m^2)	$2.7^{+3}_{-1.5} \times 10^{-4}$	$1.10^{+0.17}_{-0.13} \times {}^{-3}$	$6.3^{+2}_{-1.5} \times 10^{-5}$
Norm$_{\rm mbb}$	(10^{16} m^2)	$0.33^{+0.04}_{-0.05}$	$0.33^{+0.03}_{-0.02}$	0.45 ± 0.05
$kT_{\rm bb}$	(keV)	$0.16^{+0.03}_{-0.02}$	0.246 ± 0.006	0.31 ± 0.03
$kT_{\rm mbb}$	(keV)	0.86 ± 0.04	2.33 ± 0.09	1.43 ± 0.06
L$_{\rm bb,0.3-10}$ $^{(b)}$	(10^{38} erg/s)	$0.13^{+0.14}_{-0.07}$	$3.8^{+0.6}_{-0.5}$	$0.62^{+0.2}_{-0.15}$
L$_{\rm mbb,0.3-10}$ $^{(b)}$	(10^{38} erg/s)	$0.65^{+0.10}_{-0.08}$	$5.8^{+0.5}_{-0.4}$	2.7 ± 0.3
L$_{\rm tot,0.3-10}$	(10^{38} erg/s)	$0.8^{+1.2}_{-0.7}$	9.6 ± 0.2	3.3 ± 0.4
χ^2/d.o.f.		84.97/84	360.76/251	187.72/178
		Model 3 : hot (dbb + comt)		
$N_{\rm H}$	(10^{21}/cm^2)		5.8 ± 0.2 $^{(a)}$	
Norm$_{\rm dbb}$	(10^{16} m^2)	$3.7^{+3}_{-1.5} \times 10^{-5}$	$5.9^{+1.7}_{-1.3} \times 10^{-5}$	$1.0^{+0.5}_{-0.3} \times 10^{-5}$
Norm$_{\rm comt}$	(10^{44}ph/(s keV))	118^{+83}_{-72}	180^{+144}_{-148}	262^{+164}_{-233}
$kT_{\rm dbb}$	(keV)	0.33 ± 0.03	0.49 ± 0.02	$0.52^{+0.05}_{-0.04}$
$kt_{\rm e}$	(keV)	$2.9^{+19}_{-1.1}$	10^{+24}_{-4}	$3.5^{+17}_{-1.3}$
τ			$2.9^{+1.3}_{-3}$ $^{(a)}$	
L$_{\rm dbb,0.3-10}$ $^{(b)}$	(10^{38} erg/s)	$0.9^{+0.7}_{-0.4}$	10^{+3}_{-2}	$2.2^{+1.1}_{-0.6}$
L$_{\rm comt,0.3-10}$ $^{(b)}$	(10^{38} erg/s)	$0.7^{+0.5}_{-0.4}$	6 ± 5	$3^{+1.7}_{-2}$
L$_{\rm tot,0.3-10}$	(10^{38} erg/s)	$1.6^{+1.5}_{-1.1}$	$16^{+1.1}_{-1.0}$	$5.2^{+1.1}_{-0.9}$
χ^2/d.o.f.		83.05/84	310.68/251	182.50/178

Notes: $^{(a)}$ $N_{\rm H}$ and τ are coupled between the observations. $^{(b)}$ L$_X$ (0.3–10 keV) unabsorbed luminosities are calculated assuming a distance of 1.9 Mpc.

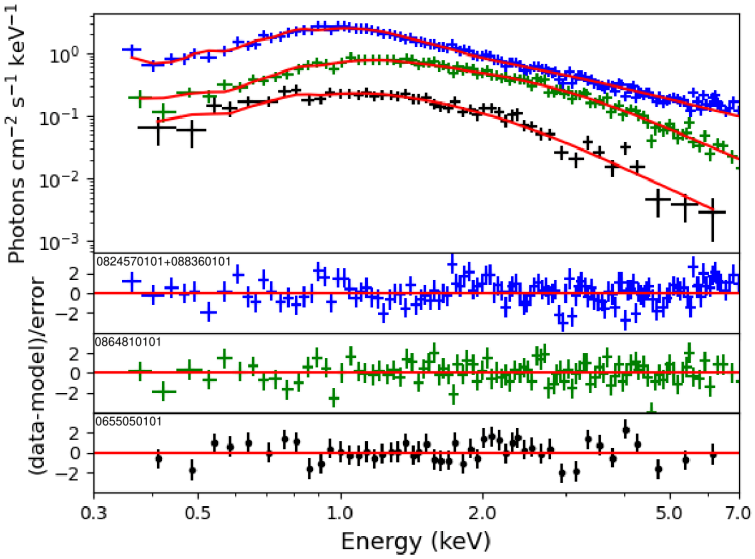

Figure 3.2: *XMM-Newton* spectra of NGC 55 ULX-2 candidate. For visual purposes, only EPIC-pn data are shown. The best-fit DBB+COMT model is overlapped (red, solid line). The bottom panels show the corresponding residuals.

which is about 10× higher than its upper limit in the other observations, where the line is not significant.

As seen in Table 3.2, we estimated that during the *XMM-Newton* Obs.ID 0824570101 and 0883960101, the source reached an unabsorbed 0.3–10 keV luminosity of 1.6×10^{39} erg s^{-1} (using model DBB+COMT), which would put the source in the low-luminosity end of the typical luminosities observed in transient ULXs. The spectral parameters obtained for the two observations with lower flux (Obs.ID 0655050101 and 0864810101) within the uncertainties are similar to those previously obtained for the soft state of transient BHs (e.g. Del Santo et al. 2008).

In order to understand the structure of the accretion disc, we also estimated the inner radius for the DBB component in the DBB+COMT model for each observation, using the normalisation factor with the formula $r_{\rm in} = \sqrt{(\rm norm/cos\, i)}$, where i is the inclination of the disc with respect to our line of sight. The inner radius results in $R_{in}(\cos\, i)^{-1/2} \approx$ 600, 800, and 300 km (with uncertainties of 50-100%), for the three spectra, respectively (0655050101, 0824570101+0883960101 and 0864810101). As we expect for transient BHs, the source becomes softer and brighter when approaching 10^{39} erg/s from Obs.ID

0655050101 to 0864810101: the radius of the disc decreases resulting in an increase of the temperature likely due to a higher but still Eddington-limited $\dot{m}$. The transition to the ULX state is instead followed by an expansion of the disc photosphere as expected from super-Eddington accretion.

3.4 Temporal Analysis

3.4.1 Short-term variability

We extracted *XMM*/EPIC-pn light curves in the 0.3–10 keV and in two energy-selected bands (i.e. soft 0.3–1 keV and hard 1–10 keV) with a time bin of 1 ks. We computed the hardness ratios (HRs) as the ratio between the counts in the hard and the broad energy bands. We use data from all 8 observations to explore the source flux in different epochs. Due to the MOS lower count rate, we mainly use its data to confirm the overall trend measured with pn. The pn light curves of the 8 observations are then glued and shown in Fig. 5.2 (right panel). The light curve was rebinned for visual purposes. The light curve shows $\lesssim$2 ks dips, during which the flux decreases by a factor of 20%. These dips are shallower than those seen in NGC 55 ULX-1 or other soft ULXs suggesting that a less dense wind crosses the light of sight. This is likely due to a lower accretion rate in ULX-2.

We estimate the fractional root-mean-square variability (*rms*) for the light curves of the three longest *XMM-Newton* observations using standard equations (Vaughan et al. 2003). The three light curves have comparable time baselines (115-120 ks) albeit a slightly different effective clean exposure (due to periods of high proton flaring background, see Table 3.1). They show low intra-day variability similarly to high/soft states in XRBs (e.g. Koljonen et al. 2018) and many other ULXs with soft spectra ($\Gamma \sim 2-3$, e.g. Heil et al. 2009). The highest value (*rms* $\sim$ 9 %) is measured in the observation with the lowest flux. The other values are *rms* $\sim$ 7 % and $\sim$ 3 % for Obs.ID 0824570101 and 0864810101, respectively.

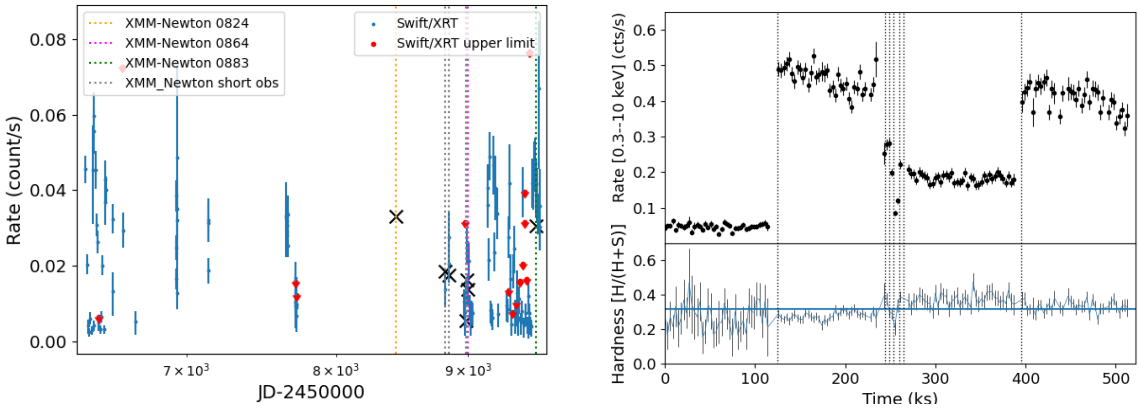

Figure 3.3: Left: 0.3–10 keV long-term *Swift*/XRT light curve of NGC 55 ULX-2, with the dates of the *XMM-Newton* observations indicated by vertical dotted lines and the equivalent XRT count rates indicated by black 'X'. Right: 0.3–10 keV *XMM-Newton* / EPIC-pn light curve of NGC 55 ULX-2. Since the observations occur at different epochs, we removed the gaps between observations with grey-dashed lines for displaying purposes.

3.4.2 Long-term variability

The *XMM-Newton* data show that the source count rate has varied by an order of magnitude over the years (and more if we account for the two earliest observations, i.e. when it was undetected). For the 2001 *XMM-Newton* observations, Jithesh & Wang (2015) calculated the upper limit of the count rate in 0.3–8 keV, resulting in $L_X < 10^{36}$ erg s^{-1}. The lack of detection might have been caused by either a variation of the disc inclination due to the precession of the accretion disc, or the onset of the propeller effect (in the case of a magnetised neutron star), perhaps due to a lower accretion rate, below 10^{38} erg s^{-1}, which is the lowest level found in both the *XMM-Newton* and *Swift* light curves (see below).

The X-ray behaviour of ULX-2 is similar to that seen in GRS 1915+105, which after 25 years of high-brightness X-ray activity has decayed into a prolonged low-flux X-ray state (see Motta et al. 2021).

In order to better understand the behaviour of this source, we also studied the 0.3–10 keV historical light curve by using all the archival *Swift*/XRT observations taken between April 2013–January 2022 (see Fig. 5.2, left) produced with the online tool (Evans

et al. 2007)[3]. The *Swift*/XRT monitoring confirms the strong long-term variability and underlines the presence of multiple high-flux states as previously suggested by Jithesh & Wang (2015). In Fig. 5.2 the dotted lines show the dates of the *XMM-Newton* observations. Unfortunately, we do not have much information on the period between 2017–2019. However, using WEBPIMMS[4] and a simple powerlaw (with Γ=2.6) fit for the *XMM-Newton* observation 0824570101, we predict a *Swift*/XRT count rate of 0.033 cts/s (0.3–10 keV). This corresponds to the high count-rate epochs of the XRT light curve. Moreover, we see that ULX-2 shows even higher peaks of $\sim$ 0.05 counts/sec (cts/s), which is the average *Swift*/XRT count level of NGC 55 ULX-1 (Pintore et al. 2015).

We also investigated the possible presence of long-term periodicities, like the super-orbital variability seen in a number of ULXs, by applying a Lomb-Scargle search (Lomb 1976; Scargle 1982; VanderPlas 2018). We adopted the LOMBSCARGLE function in the TIMESERIES class of the Python package ASTROPY[5].

We firstly analysed all the available *Swift*/XRT observations, choosing the background subtracted source events in the 0.3–10 keV energy band. We searched for periodicities in the frequency range (5×10^{-4} – 0.08) 1/d. We found that in the periodogram no statistically significant signal (>5σ) is found. This may be due to the scanty time coverage of the whole *Swift*/XRT dataset.

Therefore we restricted our analyses to all the observations taken after MJD 58800 (11/2019 to 12/2021), where the *Swift*/XRT time sampling is denser. We found that the periodogram shows two peaks at periods in the range 40-60 days. The highest peak is at 41 days, but the false alarm probability (FAP) of this signal is very poor (0.81), meaning that it is not statistically significant.

A similar approach was applied to the observations earlier than MJD 58800 (04/2013 to 12/2016). The highest peak was at $\sim$ 67 days. This could imply that during the large gap of three years the evolution of the system might have changed any super-orbital modulation. We however caution the reader that a longer and more regular monitoring of the source is necessary to confirm such a tentative periodicity.

[3] https://www.swift.ac.uk/user_objects/
[4] https://heasarc.gsfc.nasa.gov/cgi-bin/Tools/w3pimms/w3pimms.pl
[5] https://docs.astropy.org/en/stable/timeseries/lombscargle.html

3.4.3 Search for pulsations

We performed a deep search for periodic signals over the *XMM-Newton* light curves, following the detection method outlined in Israel et al. (2016). Since significant period variations are observed in pulsating ULXs, we corrected the events time of arrival (ToA), for the presence of a first period derivative, using a grid of 3000 points, by a factor of $-\frac{1}{2}\frac{\dot{P}}{P}\,t^2$, in the range $3{\times}10^{-6} < |\frac{\dot{P}}{P}\,(\mathrm{s}^{-1})| < 9{\times}13^{-11}$, where $\dot{P}$ is the first period derivative. We also corrected the ToA for an orbital motion, with orbital periods in the range from 4h up to 4d and a projected semimajor axis in the range 0.05 – 120 lt-s (see Rodríguez Castillo et al. 2020 for details). No significant coherent signals were detected; we estimated a 3σ upper limit of $\sim 15\%$ for the pulsed fraction in the data (i.e. the semi-amplitude of the signal sinusoid divided by the average count rate).

3.5 Discussion and Conclusions

In this work, we report the identification of a new ULX candidate (ULX-2) in the galaxy NGC 55. This source was previously reported as a transient X-ray source with a luminosity of a few 10^{38} erg s^{-1}, but thanks to new, deeper, *XMM-Newton* data, we show that the source surpasses the 10^{39} erg s^{-1} threshold in multiple occurrences. In some cases, sources are detected with luminosity lower than 10^{39} erg s^{-1} before reaching the ULX regime (e.g. Hu et al. 2018).

Unlike many transients, characterised by a hard spectrum with $\Gamma < 2$ (e.g. Earnshaw et al. 2020), NGC ULX-2 has a soft spectrum. In the *XMM-Newton* Obs.ID 0824570101 and 0883960101 where the source reaches $L_{X\,[0.3-10\,\mathrm{keV}]} > 10^{39}\,\mathrm{erg\,s^{-1}}$, the spectrum is much softer than in previous observations and, according to Sutton et al. (2013), fits in the class of soft ULXs (with a $F_{\mathrm{pow}}/F_{\mathrm{dbb}} \gtrsim 5$ flux ratio and $\Gamma > 2$). These sources become typically softer when brighter if the higher flux is driven by an increase in the $\dot{M}$ (e.g. NGC 5408 ULX-1, Gúrpide et al. 2021a). This is due to the fact that they are seen at moderately high inclination and at high accretion rates (close or above Eddington). The inner hot accretion flow is substantially obscured by the disc bulge around the spherisation radius and the wind. Therefore, at higher $\dot{M}$ the source would get even softer (Middleton et al. 2015a). For more information on the lower states of ULX-2, see Jithesh & Wang (2015) who suggests that the source is likely a stellar-mass BH or

NS XRB. A wind seems indeed to appear in the brightest (ULX) state as shown by the features observed around 1 keV (see Fig. 3.2) and formerly resolved in to emission and absorption lines from photoionised gas in many ULXs (e.g. Pinto et al. 2016, 2017).
The temporal behaviour shows that the time scales of the flux variations are of the order of a month. Over such period the flux can change by up to an order of magnitude. A tentative modulation on time scales of the order of 2 months appears in the earlier monitoring (2013–2016), but it is not confirmed in the follow-up observations (2019–2021) possibly due to the shorter and sparser monitoring. Super-orbital modulations on similar time scales are found in several ULXs and are sometimes attributed to precession of the accretion disc (Fürst et al. 2018). It is possible that, in addition to this geometric factor, the variability of the source can be associated with variations of the accretion rate. As a consequence of the increase of $\dot{m}$, the source becomes softer entering in the ULX state. Additional observations and cycles will be important to confirm or reject this result.
Extrapolating the best-fit model to the 0.01-100 keV band, we estimate for the 2018 and 2021 *XMM-Newton* observations a bolometric luminosity of $\sim 3 \times 10^{39}\,\mathrm{erg\,s^{-1}}$. Its equivalent *Swift*/XRT count rate is 50% lower than the *Swift*/XRT peaks, which suggests that the source might reach even higher bolometric luminosities, and confirms ULX-transient nature.

4

Broadband X-ray spectral variability of the pulsing ULX NGC 1313 X-2

Summary

Super-Eddington accretion is one of the most interesting and extreme phases in the life of black holes and neutron stars, with a significant impact on their evolution. Multi-epoch studies of spectral variability showed that the trend between bolometric luminosity and inner temperature in ULXs disagrees with the $L_{\rm disc} \propto T_{\rm in}^4$ relationship expected in the case of sub-Eddington discs. In the most luminous ULXs, with high-quality spectra, an inverted L–T relationship ($L_{\rm disc} \propto T_{\rm in}^{-4}$) has been discovered. In this work, I present a comprehensive X-ray study of the pulsating ULX NGC 1313 X-2, characterised by a strong spectral variability. In order to follow the spectral evolution, I analysed the full set of available observations with *XMM-Newton*, which covers 17 years, modelling the spectra with two thermal components (for the disc) plus a cutoff power law (for the accretion column onto the neutron star). I found an anti-correlation between the temperature and the luminosity of the cool component, suggesting an expansion of the photosphere of the disc or soft X-ray emission from the wind.

4.1 Introduction

Ultraluminous X-ray sources (ULXs) are among the best candidates for studying super-Eddington accretion in stellar-mass accreting compact objects. ULXs are the brightest off-nuclear, steady, point-like X-ray sources ($> 10^{39}$ erg s^{-1}) in the Universe. They are often found in or near regions of recent star formation (Swartz et al. 2009; Kovlakas et al. 2020) and they have X-ray luminosities that exceed the isotropic Eddington luminosity for a standard black hole (BH) with a mass of M≈10 $M_\odot$ (e.g. Kaaret et al. 2017). ULXs represent a heterogeneous sample of astronomical sources and are composed of a compact object, most likely a BH or a NS, and a companion star, which has been found to be a red or blue supergiant in some ULXs, see for example Heida et al. (2019).

In order to explain the high X-ray luminosities of these sources, several hypotheses have been proposed. A first scenario suggests that ULXs are powered by stellar-mass BHs whose radiation is preferentially beamed in our line of sight (King et al. 2001; Poutanen et al. 2007). A second scenario supposes that a BH more massive than 10 $M_\odot$ (30−80 $M_\odot$; e.g. Zampieri & Roberts 2009), which accretes at or below the Eddington limit, is the compact object of a ULX. The existence of more massive BHs was proven by the detection of gravitational waves (e.g. Abbott et al. 2016b,a; Abbott et al. 2019, with BH masses between 10 $M_\odot$ and 80 $M_\odot$. In addition, in the past, other theories have suggested that some of these systems could be intermediate-mass BHs (10^{3-4} $M_\odot$, Colbert & Mushotzky 1999), accreting at sub-Eddington rates from low-mass companion stars with ESO243-49 HLX-1 being the best candidate (see Farrell et al. 2009).

For many years, the mass estimation of putative BHs powering ULXs was the subject of significant debate. However, the recent detection of coherent pulsations in several sources clearly demonstrates that some ULXs are powered by NSs accreting at very high Eddington rates with luminosities up to $\sim 500\,L_{Edd}$. The first pulsation in a ULX was discovered in M 82 X-2 by Bachetti et al. (2014) with *NuSTAR* observations and, at the moment, six ULXs are known to exhibit pulsations (Israel et al. 2017a,b; Fürst et al. 2016; Carpano et al. 2018; Sathyaprakash et al. 2019). It is not straightforward as to how to distinguish between BH and NS accretors based on the spectral analysis alone (Pintore et al. 2017; Koliopanos et al. 2017; Walton et al. 2018d). Moreover, pulsations are not always detectable; high count rates are indeed required for a low pulsed fraction or long

exposure times for low count rates. This means that NSs are likely numerous among the compact objects of ULXs (see also Rodríguez Castillo et al. 2020; Wiktorowicz et al. 2019; King et al. 2017; Middleton & King 2016).

One of the fundamental predictions of the super-Eddington accretion theory is that strong, relativistic winds are launched from the supercritical discs, driven by the extreme radiation pressure (see e.g. Poutanen et al. 2007). Middleton et al. (2014) suggest that the spectral residuals around 1 keV could be associated with the winds. The first discovery of powerful winds in two ULXs was achieved by Pinto et al. (2016) by detecting blueshifted absorption lines in the high-resolution soft X-ray spectra provided by the *XMM-Newton* Reflection Grating Spectrometers (RGS). Further confirmations in other ULXs and with different detectors were obtained by Walton et al. (2016), Pinto et al. (2017), Kosec et al. (2018a) and Kosec et al. (2018b). The exact launching mechanism of such winds is still unclear as magnetic pressure might also contribute, although Pinto et al. (2020a) show that the relation between their velocities and ionisation parameters with the ULX luminosities agrees with the radiation driving mechanism. A thorough understanding of the ULX phenomenology requires additional constraints on the nature of these winds and their link with the source appearance and, therefore, accretion rate. This involves a study of the wind properties via high-resolution X-ray spectroscopy combined with a careful study of the evolution of ULX broadband spectra.

In this work we present the analysis of the X-ray spectra of the pulsating ULX X-2 in the galaxy NGC 1313. This barred galaxy (see Fig. 4.1) hosts a supernova remnant (SN 1978K) and two ULXs: X-1, close to the nucleus, and X-2, in the outskirts of the galaxy, which is the subject of this work. Sathyaprakash et al. (2019) discovered pulsations in NGC 1313 X-2 for the first time thanks to our deep *XMM-Newton* campaign. This ULX is characterised by strong variability in both luminosity and spectral shape. The high X-ray variability and spectral hardness suggest that the object is viewed at an inclination angle, which is low enough to allow for a direct view of the inner regions of its accretion flow and to detect pulsations (Middleton et al. 2015b). NGC 1313 X-2 also shows evidence of winds in the form of X-ray spectral features in the soft band (see, e.g. Middleton et al. 2015b and Kosec et al. 2018a).

Throughout this work, we assume a distance of D = 4.2 Mpc to NGC 1313 (Mendez et al. 2002; Tully et al. 2016). The only Cepheid distance available is 4.6 Mpc, which is a little bit of an outlier from the other measurements (Qing et al. 2015).

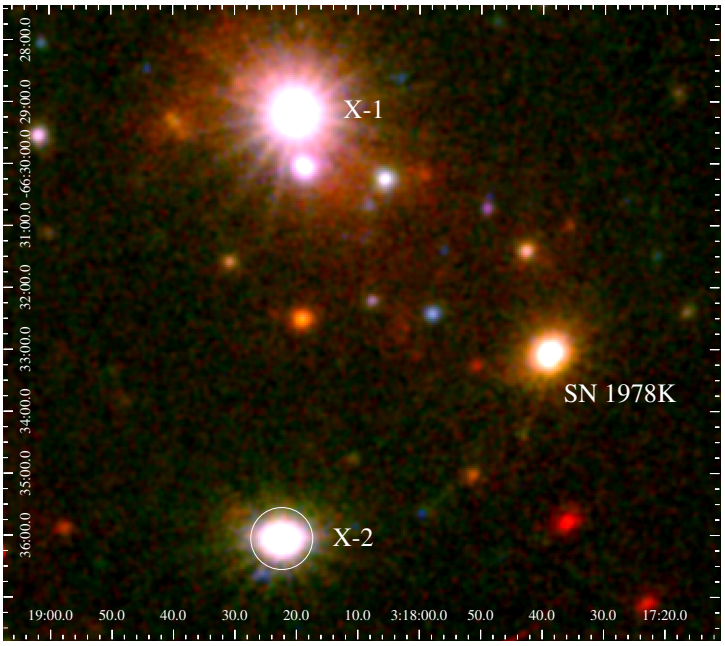

Figure 4.1: *XMM-Newton* image of NGC 1313, which we obtained by combining all the data available from the 2017 EPIC-pn and MOS 1,2 observations. The 30″-radius circle around the ULX X-2 represents our default source extraction region. The red colour corresponds to 0.2–1 keV, green is for 1–2 keV, and blue is for 2–12 keV.

This paper is structured as follows. In Section 4.2, we provide details about the *XMM-Newton* observations used in this work and the data reduction. We show some basic time properties and the model-independent variability of the X-ray spectral shape. In Section 4.3, we describe the main results of the spectral and timing analysis, while in Section 4.4 we discuss the behaviour of the thermal components in the luminosity-temperature plane and, finally, provide our conclusions in Section 4.5.

4.2 Data analysis

4.2.1 Observations

We analysed the public archival *XMM-Newton* data of all the high signal-to-noise observations between 2000 and 2017. For our analysis, we particularly benefitted from a recent deep ∼1Ms view of NGC 1313 (PI: Pinto). The observations were carried out

with the EPIC-pn and EPIC-MOS detectors (Strüder et al. 2001; Turner et al. 2001). For observations 0803990301 and 0803990401, we used only the data provided by pn and MOS 2 since the source was out of the MOS1 field of view due to damage to CCD6 and CCD3 (since 2005 and 2012, respectively). We have excluded observations 0150280201 and 0150280701 from this analysis as they contain only MOS data and they were very short, therefore providing low statistics. We also excluded observation 0205230201 because of a slew failure. Table 4.1 lists the details of the high signal-to-noise *XMM-Newton* observations (96 % of the available data) that we analysed, including the date, the duration after the removal of flares, the count rates, and the filter of each observation.

4.2.2 Data reduction

The data analysis was performed using the *XMM-Newton Science Analysis System* (SAS) version 18.0.0 and the calibration files of January 2020.[1] Following the standard procedures, EPIC-pn and MOS data were reprocessed using the tasks '*epproc*' and '*emproc*'. The calibrated and concatenated event lists were filtered for high background epochs to acquire good time intervals (GTI) as follows. For each data set and each instrument, we extracted the high energy light curve (including events between 10-12 keV) to identify intervals of flaring particle background and we chose a suitable threshold (0.35 and 0.40 cts $\mathbf{s}^{-1}$ for EPIC-MOS and pn, respectively), which is above the low steady background, to create the corresponding filtered EPIC event list. As recommended, we selected only single and double events (PATTERN ≤4) for EPIC-pn, and single to quadruple events (PATTERN ≤12) for EPIC-MOS.

We extracted EPIC MOS 1-2 and pn images in the 0.2–1/1–2/2–12 keV energy range and stacked them with the '*emosaic*' task. The field of the NGC 1313 galaxy and the brightest X-ray sources are shown in Fig. 4.1. We generally extracted source spectra from circular regions with a radius of 30", except where the source was near the edge of the CCD (in these cases we used regions with a radius of 20") and the corresponding background from a larger circle in a nearby region on the same chip, free from contaminating point sources. The background region was also not generally placed in the Copper emission region (Lumb et al. 2002), with the exception of a small number

[1] https://www.cosmos.esa.int/web/xmm-newton/ccf-release-notes.

Table 4.1: *XMM-Newton* observations of NGC 1313 X-2.

Obs.ID [1]	Date [2]	Exposure time [3] (s)			Count rates [4] (cts/s)			Filter
		pn	MOS1	MOS2	pn	MOS1	MOS2	
0106860101	2000-10-17	31638	29250	29183	0.2554	0.07654	0.07588	Medium
0150280101	2003-11-25	19173	12498	12501	0.712	0.2181	0.2584	Thin1
0150280201	2003-12-09	5648	3609	3622	-	-	-	Thin1
0150280301	2003-12-21	10335	11971	11976	0.8365	0.2803	0.2795	Thin1
0150280401	2003-12-23	14098	15278	15293	0.9459	0.3081	0.3104	Thin1
0150280501	2003-12-25	15299	15262	15249	0.5249	0.1551	0.1510	Thin1
0150280601	2004-01-08	14757	15382	15377	0.4095	0.1277	0.1287	Thin1
0150280701	2003-12-27	16686	17779	17810	-	-	-	Thin1
0150281101	2004-01-16	7036	8671	8676	0.3545	0.1117	0.1170	Thin1
0205230201	2004-05-01	3459	12270	12275	-	-	-	Thin1
0205230301	2004-06-05	10036	11672	11674	0.9813	0.3181	0.32	Thin1
0205230401	2004-08-23	16137	17771	17776	0.2829	0.08781	0.09462	Thin1
0205230501	2004-11-23	14137	15769	15774	0.3190	0.09469	0.09883	Thin1
0205230601	2005-02-07	12437	14071	14074	0.9053	0.2974	0.3023	Thin1
0301860101	2006-03-06	19937	21570	21575	0.6510	0.1734	0.1963	Medium
0405090101	2006-10-15	121190	122456	122453	0.6437	0.1689	0.1576	Medium
0693850501	2012-12-16	123341	124921	124927	0.5395	0.1820	0.1819	Medium
0693851201	2012-12-22	123341	124921	124924	0.275	0.1036	0.1086	Medium
0722650101	2013-06-08	28841	30421	30426	0.1713	0.009892	0.01064	Medium
0742590301	2014-07-05	60040	61653	61624	0.3937	0.1074	0.1035	Medium
0742490101	2015-03-30	100041	98937	101625	0.07816	0.07223	0.07989	Medium
0764770101	2015-12-05	71941	73555	73524	0.2417	0.07106	0.07295	Thin1
0764770401	2016-03-23	30041	31653	31624	0.4102	0.1260	0.1261	Thin1
0782310101	2016-10-08	88041	89655	89626	0.5705	0.1863	0.1865	Medium
0794580601	2017-03-29	44542	46155	46127	0.3424	0.07281	0.1022	Medium
0803990101	2017-06-14	134142	133036	135725	0.2304	0.09635	0.09032	Medium
0803990201	2017-06-20	130841	132453	132425	0.3525	0.07631	0.08879	Medium
0803990301	2017-08-31	96686	-	91971	0.2380	-	0.07478	Medium
0803990401	2017-09-02	64008	-	63472	0.1077	-	0.09849	Medium
0803990701	2017-09-24	14500	9798	9797	0.2483	-	0.06602	Medium
0803990501	2017-12-07	125941	127555	127524	0.07091	0.07314	0.07887	Medium
0803990601	2017-12-09	125942	127555	127524	0.07893	0.07587	0.08123	Medium

Notes: [1] observation identifier; [2] observation date (yyyy-mm-dd), [3] exposure time corrected for solar flares, [4] count rates in the 0.3–10 keV energy band.

of observations for which X-2 was also located in the Cu region.

We used the task '*arfgen*' to reproduce the effective area of the instrument and to correct instrumental factors, such as bad pixels and bad columns, using calibration information. The response matrix was generated with '*rmfgen*'. Since the EPIC-MOS1 and EPIC-MOS2 spectra are consistent for each observation, we stacked data from the MOS cameras into a single spectrum with the '*epicspeccombine*' routine.

4.2.3 Spectral analysis

Fig. 4.2 shows an overview of the spectral properties of X-2. In particular, the right panel illustrates the shape of the observed EPIC-pn spectra of NGC 1313 X-2 for six individual exposures during the most recent campaign (2017). The spectra indicate substantial variability in luminosity by a factor of up to five and there is no significant spectral variability. The left panel of Fig. 4.2 instead shows a comparison between some spectra of a remarkably different shape and flux: a high flux spectrum (Obs.ID:0150280401), two spectra with intermediate flux (Obs.ID:0803990201 and Obs.ID:0782310101), and one with low flux (Obs.ID:0106860101). As it has been observed in most ULXs (e.g. Middleton et al. 2015b), the spectrum becomes harder at higher fluxes. This behaviour disagrees with that seen in the classical Galactic X-ray binaries that accrete below Eddington limit and it is therefore considered as strong evidence in support of super-Eddington accretion. The left panel of Fig. 4.2 clearly shows that the spectrum is more variable in the hard X-ray band ($\gtrsim$ 1 keV), which indicates that at least two different (soft and hard) spectral components are responsible for the X-ray emission.

We carried the spectral analysis out over the 0.3-10.0 keV energy range with XSPEC version 12.10.1 (Arnaud 1996). We simultaneously fitted the spectra of the MOS and pn cameras and estimated the parameter uncertainties at the 68% confidence level. Spectra were grouped for a minimum of 25 counts per energy bin, so that the χ^2 statistic could be used.

There is no coverage beyond 10 keV in most observations and even in the *NuSTAR* data, the source has low statistics above 10 keV (e.g. Bachetti et al. 2013). As the source is generally softer than X-1 in the NGC 1313 galaxy, the systematic error due to the lack of *NuSTAR* data is negligible. We therefore focussed on the canonical 0.3-

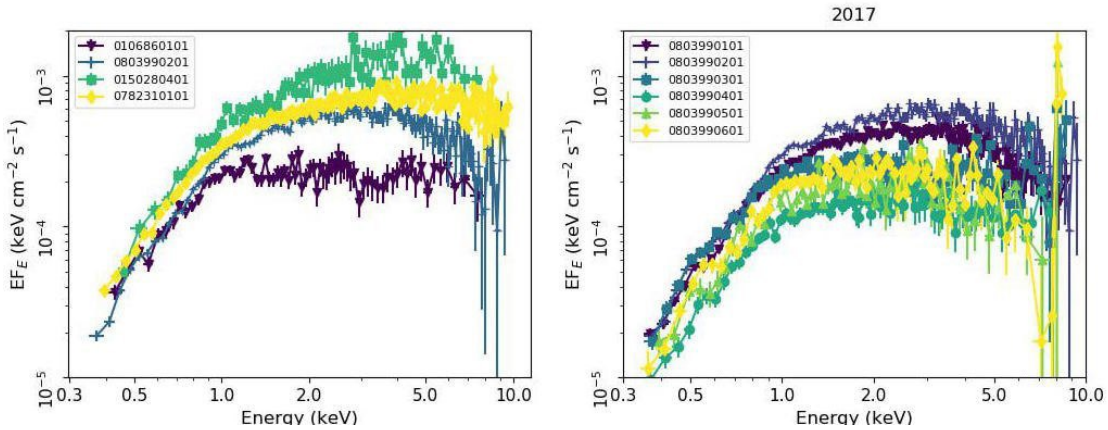

Figure 4.2: Left panel: Comparison between four spectra, from low (Obs.ID:0106860101), to intermediate (Obs.ID:0803990201 and Obs.ID:0782310101), and to high flux (Obs.ID:0150280401). Right panel: *XMM-Newton*/EPIC-pn spectra of the recent observations (2017 campaign).

10 keV X-ray band and assumed a simplified model with either two or three emission components. In the case, for instance, of the double blackbody disc and an exponential cutoff powerlaw model, the low-temperature component mimics the emission of the outer disc and wind, while the hotter temperature component reproduces the emission from the inner super-Eddington accretion flow. The third component is necessary to describe the contributions of the central accretion columns by the magnetic accretor, that is, the NS. Walton et al. (2018d) show that in all ULXs, this latter component is significant above 8-9 keV (see also Bachetti et al. 2013).

4.2.4 Timing analysis

In order to better understand our spectra, we extracted light curves in the whole band (0.3–10 keV) and in two different bands (i.e. soft 0.3–1.2 keV and hard 1.2–10 keV). The latter were extracted to calculate the hardness ratios (HRs), which were computed as follows: NGC 1313 X-2 shows high variability during the two decades of (non-contiguous) observations. As a short-term flux variability test, we adopted the normalised excess variance in the whole band (0.3–10 keV), which is useful to quantify the different amplitudes of intrinsic variability of each light curve. As reported by

Nandra et al. (1997), it is defined as follows:

$$\sigma^2_{NXV} = \frac{1}{N\bar{x}^2}\sum_{i=1}^{N}[(x_i - \bar{x})^2 - \sigma^2_{err,i}], \tag{4.1}$$

where x_i and $\sigma_{err,i}$ are the count rate and its error in the i-th bin, $\bar{x}$ is the mean count rate, and N is the number of bins used to estimate σ^2_{NXV}. The associated error is the following:

$$\Delta\sigma^2_{NXV} = \frac{S_D}{\bar{x}^2(N)^{1/2}},$$
$$S_D = \frac{1}{N-1}\sum_{i=1}^{N}\{[(x_i - \bar{x})^2 - \sigma^2_{err,i}] - \sigma^2_{NXV}\bar{x}^2\}^2.$$

The fractional root mean square (RMS) variability amplitude (F_{var}, see Vaughan et al. 2003) is the square root of the normalised excess variance, that is

$$F_{var}(\%) = \sqrt{\sigma^2_{NXV}} \times 100 = \sqrt{\frac{1}{N\bar{x}^2}\sum_{i=1}^{N}[(x_i - \bar{x})^2 - \sigma^2_{err,i}]} \times 100 \tag{4.2}$$

$$\Delta\sigma_{F_{var}}(\%) = \frac{1}{2} * \frac{\Delta\sigma^2_{NXV}}{\sqrt{\sigma^2_{NXV}}} \times 100, \tag{4.3}$$

where F_{var} is a linear statistic, which gives the same information as σ^2_{NXV}, but in percentage terms. In order to compare the RMS and to account for the different exposure times, we split all light curves into 40ks segments, which is approximately a minimum-common-denominator segment for the long observations. Then we averaged the RMS results from the two or more segments available in longer (80-120 ks) observations and binned with ΔT of 1000 s. For the observations shorter than 40 ks, we did not estimate the RMS.

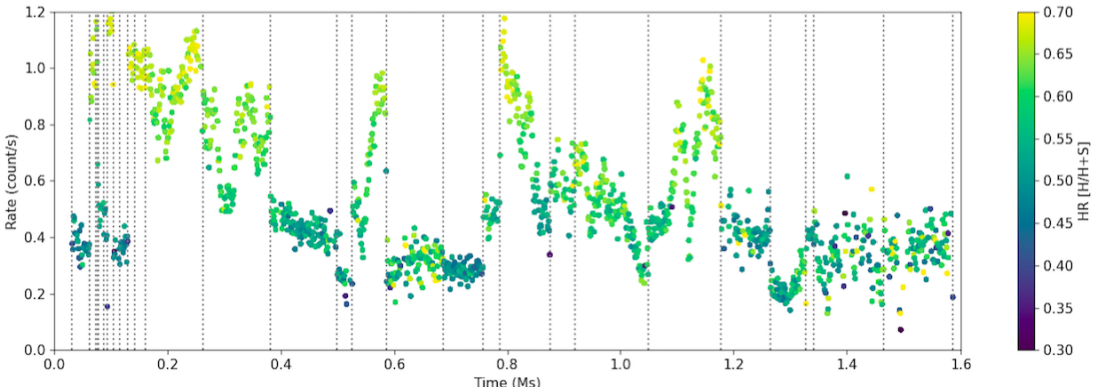

Figure 4.3: 0.3–10 keV long-term EPIC/pn light curve of NGC 1313 X-2 colour-coded according to the HR for all the *XMM-Newton* observations, with time bins of 1000 s. The HR was computed using the light curves in the soft [0.3–1.2 keV] and in the hard [1.2–10 keV] X-ray energy bands. Observations occur at different epochs: we removed the gaps between observations with grey-dashed lines for visual purposes.

4.3 Main results

4.3.1 Spectral modelling

In this section, we present the spectral analysis of NGC 1313 X-2. In order to obtain an adequate description of the continuum, ULX broadband X-ray spectra require several emission components. Among the several models tested, we adopted one similar model to that used in Walton et al. (2018d). All models also include neutral absorption, which was modelled with TBABS (Wilms et al. 2000). This absorption, which is due to an interstellar and circumstellar medium in the line of sight towards the source, is necessary to partially explain the low-energy spectral curvature. We adopted a lower limit equal to the Galactic value of N_H=7 $\times$ 10^{20} cm^{-2}.

Baseline models

Our baseline model for the X-ray spectra of NGC 1313 X-2 consists of two thermal components, a cold disc blackbody (DISKBB) and a warmer DISKBB for the outer and the inner disc, respectively. It also consists of an exponential cutoff powerlaw component (CUTOFFPL) for the central accretion column that forms when the material flows down

onto the magnetic poles. For the CUTOFFPL component, we set its spectral parameters to the average values seen from the pulsed emission of the following ULX pulsars currently known: Γ = 0.59 and E_{cut}= 7.9 keV (Brightman et al. 2016; Walton et al. 2018b,d,a).

In most spectra, there are notable residuals at ~1 keV, related to atomic emission and absorption associated with the likely presence of an extreme outflow powered by wind (Pinto et al. 2016; Kosec et al. 2018a,b; Wang et al. 2019). Despite this, the overall shape of the X-ray spectra is well reproduced by our featureless continuum model. Indeed, as pointed by Pinto et al. (2020a) and Walton et al. (2020), the presence of the wind has no dramatic effects on the modelling of the spectral continuum and, therefore, we did not include any line emission or absorption components in our current fits. In addition, this would require the use of deep, on-axis, RGS spectra that are unavailable since the source is off-axis in most of the observations. This is valid for the optically thin ionised wind phase responsible for the spectral lines, but it might not hold in the case of further optically thick wind components.

The spectral fits with the best-fitting baseline double disc-blackbody and the exponential cutoff powerlaw models are presented in Appendix A.1. As we show in Table A.1, we obtained a column density between N_H = (0.095–0.32) × 10^{22} cm^{-2}, a cold temperature in the range from 0.20 < T_1 < 0.49 keV, and a warm temperature in the 0.69 < T_2 < 1.9 keV range. The corresponding luminosities are L_1 = (1–6) × 10^{39} erg s^{-1} and L_2 = (2–8) × 10^{39} erg s^{-1}. The goodness of the spectral fits is indicated by the χ^2, which are satisfactory as shown in Table A.1 (the reduced χ^2 are in the range from 0.8–1.4).

Alternative models

We also tested several other models to describe the spectral shape of the spectrum of X-2. We show examples of our model fits for Obs.ID:0803990201 in Fig. 4.4 with corresponding best-fit parameters in Table 4.2.

Spectral modelling of ULXs using *XMM-Newton* data is well established with two-component models, which resemble multi-colour blackbody emission (e.g. Gladstone et al. 2009 and Stobbart et al. 2006). In this context, the first attempt consists of a double disc-blackbody DISKBB+DISKBB, in which the first component describes the outer accretion flow and the possible optically thick wind and the second one takes both

the inner flow and any other emission closer to the NS into account. As we expected (considering the lack of the hard cutoff powerlaw component), in comparison to the best-fitting model, the values of the temperatures are larger. The column densities, on the other hand, are similar (see Table A.2). We also tested the model with the column density fixed to $N_H = 1.94 \times 10^{21}$ cm^{-2}, obtained from the weighted average of the previous fits with free N_H, to evaluate the contribution of neutral absorption and systematic effects. However, we note that this assumption does not strongly influence the broadband continuum fits, so we preferred to keep N_H free to vary amongst the spectra.

The spectral fits with two thermal components are generally worse than the baseline three-component model with the greatest discrepancy at the lowest flux, where the hard cutoff powerlaw component starts to be important ($\Delta\chi^2$ = 41 and 61 for Obs.ID 0405090101 and 0782310101, respectively, for 1 additional degree of freedom). Spectral parameters are reported in Appendix A.2 (see Table A.2).

The second alternative model consists of replacing the double DISKBB continuum model with a single DISKBB modified by a SIMPL component. This empirical model of Comptonisation assumes that a fraction of the soft photons is scattered into a corona or a photosphere warmer than the disc. As shown in Table 4.2, although the parameters are physically acceptable, we found a worse fit with an increase of χ^2 ($\Delta\chi^2$ = 140) in observation 0803990201. Column densities, N_H, and cool temperature values are similar and follow the same behaviour as the baseline model with two DISKBBS plus a CUTOFFPL component.

Afterwards, we tried using a DISKBB+DISCKPBB model, where DISKPBB is a multiple blackbody disc model characterised by the additional free parameter p (Mineshige et al. 1994). The p parameter defines the radial dependency of the temperature, following the law $T \propto R^{-p}$ (p=0.75 for a standard disc, p<0.75 for a profile affected by advection, and p=0.5 for a slim disc, see Abramowicz et al. 1988).

In this case, the temperatures obtained for the cool component are similar to parameters from the best-fit (in the DISKBB+DISKBB+CUTOFFPL baseline model); whereas for the hot component, the temperature is largely unconstrained in some observations. In general, the values for parameter p (e.g. p=0.573±0.019, for Obs.ID:0803990201) indicate a regime very close to the slim disc profile (the mean value for all spectral fits is $p_{mean} \sim 0.57$). The addition of the extra free parameter (p) provides spectral fits that are statistically halfway between the two DISKBB and three component models.

All the models show some residuals around 1 keV, as described in Section 4.3.1. They appear very similar and narrow ($\sim$ 0.1 keV) in all fits, indicating that they are independent from the particular model chosen and do not affect our results.

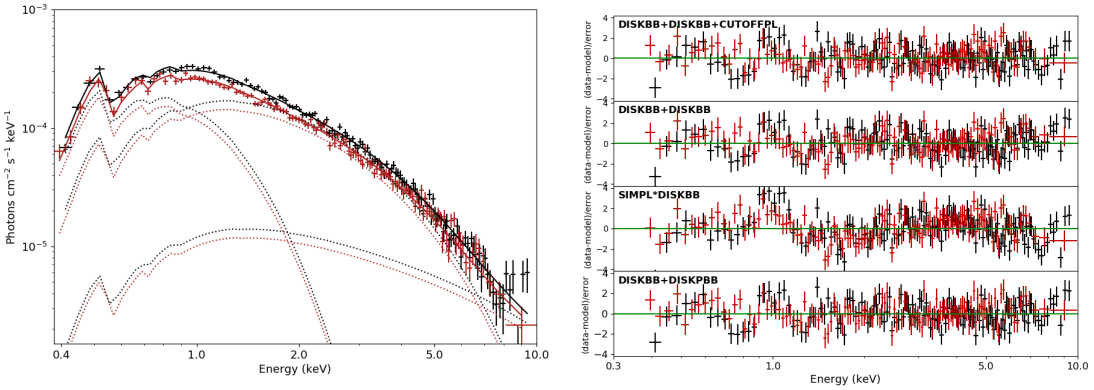

Figure 4.4: Left panel: *XMM-Newton* unfolded spectrum of observation 0803990201 of NGC 1313 X-2. The black points are EPIC-pn and the red points show the stacked EPIC-MOS1/2 data. We overlapped the best-fit DISKBB+DISKBB+CUTOFFPL model (black and red, solid lines) and its single components (dashed lines). Right panel: Residuals from a selection of models listed in Table 4.2.

4.3.2 Time variability

NGC 1313 X-2 shows high variability during the two decades of (non-contiguous) observations, as seen in the long-term light curve (see Fig. 5.2). Strong short-term ($\sim$ hours) variability is also seen during some individual and long observations. We see that the source becomes harder when it is brighter, which is indicative of an increasingly brighter super-Eddington inner disc. This is because the hot disc is the dominant component in the 0.3–10 keV energy band.

The timing properties of X-2 were also probed using the fractional variability (see Section 4.2.4). The average values of F_{var} for several observations and the corresponding HR mean are presented in Table 4.3. We have reported only the values for the observations that have a common time baseline of exposure time (40 ks) for comparing the RMS estimated. The complete values calculated for each segment are shown in Appendix A.3 (see Table A.3). Also, in cases where the observed variance is less than the error associated with each bin, the excess variance value is negative. These values

are excluded from our considerations.

As shown in Fig. 4.5, the variability of the source considerably increases in the observations with a higher flux, which is in agreement with the RMS-flux variability of accretion discs. Sutton et al. (2013) suggest that the increased flux variability observed at energies above 1 keV in ULXs with hard spectra can be attributed to the obscuration of the hard central emission when observed through the clumpy edge of the outflowing wind and from the photosphere of the super-Eddington disc.

Sathyaprakash et al. (2019) have found evidence of pulsations during observations Obs.ID:080399401 and Obs.ID:0803990601. This corresponds to the low-flux end of the new campaign, which suggests that the bright variable continuum is strongly affected by the inner accretion flow. In other words, at higher accretion rates the disc flux may significantly exceed the flux of the accretion column, thereby decreasing the pulse fraction. Walton et al. (2018d) also suggest this for the ensemble of ULXs observed by *NuSTAR*. In addition, this would imply a low-to-mild magnetic field ($B \lesssim 10^{12}$ G, see e.g. King & Lasota 2020), because the magnetospheric radius (R_m) is likely smaller than the spherisation radius (R_{sph}) for this object, given the presence of a bubble nebula (e.g. Pakull & Mirioni 2002) that is thought to be inflated by the disc wind.

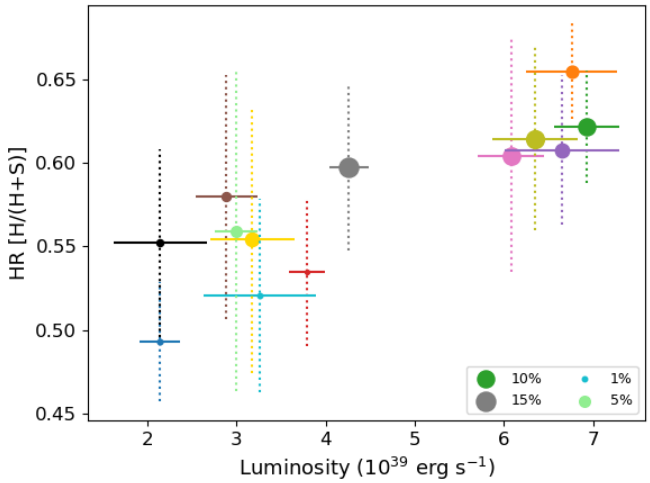

Figure 4.5: Average HR (from the 1.2–10/0.3–10 keV energy bands) versus luminosity in linear space. The size of the markers correspond to the different values of the fractional variability (reported in Table 4.3).

4.4 Discussion

We have performed a detailed spectral analysis of the ultraluminous X-ray source NGC 1313 X-2, focussing on the *XMM–Newton* observations, with the aim of understanding the long-term behaviour of the spectral components. Given that the compact object is now known to be a NS, the accretion rate must be highly super-Eddington, and its spectral and temporal properties are expected to diverge from the case of sub-Eddington thin accretion discs.

As Vierdayanti et al. (2010) showed, the evolution of NGC 1313 X-2 appears similar to the archetypal ULX Holmberg IX X-1, characterised by strong spectral variability (see also Luangtip et al. 2016; Pintore et al. 2014; Walton et al. 2014). As reported by Walton et al. (2017), the spectra of Holmberg IX X-1 are well fit by two thermal blackbody components, which dominate the emission below 10 keV, plus a powerlaw tail which dominates above 10 keV.

As shown in Fig. 4.4, the spectrum is reasonably well described by a combination of two DISKBB plus a cutoffpl components. This model approximates super-Eddington accretion onto a NS, characterised by a standard outer disc, a thick inner disc region, and strong optically thick winds, which may contribute to the cooler component. In particular, the $\sim$ 1–10 keV band is mainly dominated by the hotter component, which describes the emission from the inner region, and the cutoffpl component representing the accretion column and the boundary layer near the NS. Instead, the emission from the outer disc or from the wind is responsible for the cooler blackbody component with a temperature around 0.3 keV. Wind is expected to be launched from the upper regions of the inner disc at accretion rates comparable to or higher than the Eddington limit. This scenario is supported by the presence of strong and narrow residuals around 1 keV that have been resolved in similar sources with the aid of high-resolution X-ray spectra (Pinto et al. 2016).

The modelling of the spectra with high statistics shows that the column density, N_H, is broadly consistent with $\sim 2\times10^{21}$ cm^{-2} (see Table A.1). Fixing the N_H (see Appendix A.4) does not strongly influence the broadband continuum fits, so we preferred to keep N_H free.

With the intention of improving the analysis, we tested several spectral models, as described in Section 4.3.1. When the accretion rate is high, the structure of the disc is

expected to deviate considerably from the standard Shakura-Sunayev thin disc. For this reason, as reported by Bachetti et al. (2013), we replaced the hotter DISKBB with a DISKPBB component (we tested the DISKBB+DISKPBB model). Considering only the DISKPBB component, we have obtained similar results. Comparing the same observations analysed in Bachetti et al. (Obs.ID1:0693850501 and Obs.ID2:0693851201), we found the values of p to be consistent within 2 σ (this work: $p_{ID}1$=0.62±0.03 and p_{ID2}=$0.62^{+0.18}_{-0.07}$; Bachetti et al.: p_{ID1}=0.58±0.01 and p_{ID2}=$0.500^{+0.006}_{*}$). We also found consistent temperatures (this work: T_{in1}=$1.52^{+0.06}_{-0.04}$ and T_{in2}=$1.15^{+0.06}_{-0.07}$; Bachetti et al.: T_{in1}=1.56±0.06 and T_{in2}=1.27±0.05). In general, for several observations, the p values are compatible with an accretion regime significantly affected by advection and they are sometimes close to the slim disk regime, which strongly argues in favour of super-Eddington accretion.

In the future we will use principal component analysis (PCA) to decompose the spectrum in a model-independent way (e.g. Pinto et al. 2020b). Moreover, we will search for winds with both PCA and physical models and then we will study how they vary with the spectral shape.

4.4.1 Luminosity-temperature plane

In this section we discuss the temporal behaviour of the two thermal components, investigating how they evolve in the luminosity-temperature plane. We calculated the unabsorbed luminosities (i.e. corrected for interstellar absorption by setting the column density N_H=0) for each of the thermal components individually, over the broadband from 0.001–10 keV, which provides their bolometric values. The comparison between the temperature and the luminosity of each component in the case of free column density is shown in Fig. 4.6. We show the L–T trends for both the cool (blue) and hot (orange) thermal components in the same figure because their separation in temperature is sufficiently high to avoid confusion.

It is very useful to compare the observed trends with the $L–T^{\alpha}$ relationships as expected from theoretical scenarios such as a sub-Eddington thin disc of Shakura-Sunayev ($L \propto T^4$ for constant emitting area, see Shakura & Sunyaev 1973) or an advection-dominated disc ($L \propto T^2$, see Watarai et al. 2000). These laws are shown as red-solid and green-dashed lines in Fig. 4.6, respectively.

The L–T trend observed for the hot disk-blackbody component is somewhere in

between the two trends above. We do indeed obtain $\alpha_H = 3.0 \pm 0.35$ by fitting the L–T group of the hot component, which also argues in favour of super-Eddington accretion with a thicker disc.

The trend followed by the cool component is instead negative ($\alpha_C = -3.9 \pm 1.0$) and differs form the one expected from a sub-Eddington thin disc of Shakura-Sunayev ($L \propto T^4$) or an advection-dominated disc ($L \propto T^2$). Our results are in agreement with the interpretation of Qiu & Feng (2021), suggesting that the soft emission originates from the photosphere of the optically thick wind, driven by supercritical accretion. In this scenario, the measured blackbody luminosities of the PULXs are often higher than the Eddington limit of NSs, assuming spherical accretion (i.e. $L_{EDD,NS}$ = (1-3) $\times$ 10^{38} erg s^{-1}). Moreover, we may expect an inversion of the L–T relationship at accretion rates much higher than the Eddington limit due to the expansion of the photosphere, which is marked by an increase in the size of the emitting region of the soft component and a decrease in temperature. This effect can be interpreted as the fact that the spherisation radius, where the strong winds start to be launched, would increase with the accretion rate, yielding lower temperatures at a higher luminosity (see, e.g. Poutanen et al. 2007.)

Although the nature of the compact object is unknown, the hotter disc component of NGC 1313 X-1 also exhibits a positive relation for the luminosity-temperature trend, consistent with the theoretical scenarios. Walton et al. (2020) did not seem to find a strong anti-correlation between L and T for the low-T component, but this might be due to the low number of spectra (seven) along with the more complex DISKBB+SIMPL*DISKPBB and DISKPBB+DISKBB+cutoffpl model.

In order to check the presence of the third component, we tested the L–T trends with the simpler DISKBB+DISKBB model. As can be seen from Fig.4.7, the L–T trend observed for the hot disk-blackbody component shows a much more chaotic behaviour. Observations with better statistics (higher fluxes and longer durations) still sit somewhere in between the two theoretical cases outlined above, but there are considerable deviations for a cluster of points where the hotter component is characterised by high temperatures and low luminosities. Indeed, we obtain $\alpha_H = 2.8 \pm 0.6$ by fitting the L–T group of the hot component, which also argues in favour of super-Eddington accretion with a thicker disc. The trend followed by the cool component is instead much flatter ($\alpha_C = -0.13 \pm 0.36$) than the one expected from the theoretical scenarios. We conclude that the introduction of a third (cutoffpl) component significantly improves the spectral fits of some observations,

which is confirmed by the detection of more regular trends in Fig. 4.6 and from their lower reduced χ^2.

The presence of a correlation or anti-correlation between these points (luminosity and temperature for the hot and cool components) for the baseline model was also verified by the computation of the correlation coefficients of Pearsons and Spearmans (see Table 4.4). They were calculated using the PYTHON routines *scipy.stats.pearsonr* and *scipy.stats.spearmanr*. The result for the cooler component indicates a negative correlation and a positive correlation for the hotter component. The coefficients obtained are not very high because, as opposed to the least squares method, they do not take the error associated with the luminosity and temperature into account.

The behaviour of the soft component has also been recently examined by Gúrpide et al. (2021b). As they report, the significantly softer spectra of NGC 1313 X-2 can be explained by the scenario consistent with the wind structure responsible for highly anisotropic emission, given the wide HR variability the source spans. However, they do not report a clear correlation between the temperature and luminosity. Although their model is a double DISKBB model and thus is conceptually similar to ours, they adopted a different model for the high-energy component, using a SIMPL powerlaw continuum instead. As previously discussed, this may exacerbate parameter degeneracies when only soft X-ray data (i.e. <10 keV) are available, and this may explain the different conclusion found here. Moreover, for some observations they have used only pn spectra, resulting in a lower overall signal-to-noise ratio (S/N) and thus larger uncertainties. As we also suggest, they hypothesise that the observed residuals at soft energies around 1 keV can be produced by the presence of strong outflows. Kajava & Poutanen (2009) also studied the (L,T) relation of the soft component, although much less data were available at that time (i.e. prior to our new 2017 campaign). They found that, taken together, the soft component followed a trend $L_{soft} \propto T^{-3.5}$ for a sample of ULXs that included NGC 1313 X-2, although the behaviour of individual sources was not considered in detail. In addition, Soria (2007) showed an anti-correlation between the disc luminosity and temperature, supporting the non-standard outer disc. As Soria (2007) showed, if we assume that the boundary between the outer and inner disc scales as $\dot{m}$, the negative slope of the L–T relation depends on the T(R) function. For $T \sim R^{-0.5}$, it is expected that the $L \sim T^{-4}$, which is consistent with our result ($L \sim T^{-3.9}$). Therefore, we suggest that the outer disc is affected by the wind.

About 10% of the available data have also been analysed by Pintore & Zampieri (2012). They adopted a different model where the hot DISKBB is replaced with the much broader Comptonisation component, COMPTT. They also tied the temperature of the seed photons to that of the cool blackbody. For the broad X-ray spectra of ULXs, this has the effect of lowering the contribution in terms of flux from the cooler blackbody component. They reported a weak correlation between the luminosity of the soft component with the inner temperature, $L_{disc} \propto T_{disc}^{1.2\pm0.3}$.

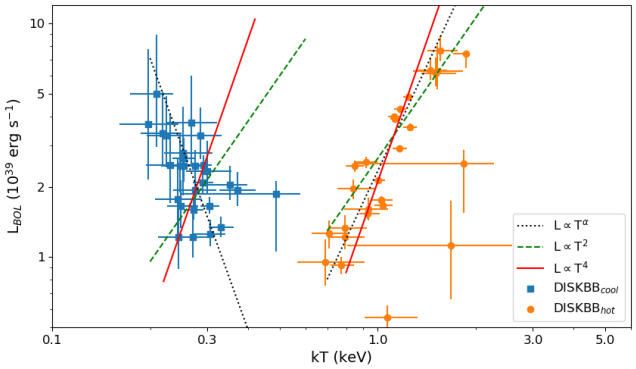

Figure 4.6: 0.001–10 keV (i.e. bolometric) luminosity versus temperature for both the cool DISKBB (blue points) and hot DISKBB (orange points) components with free column density, N_H (model: DISKBB+DISKBB+cutoffpl).

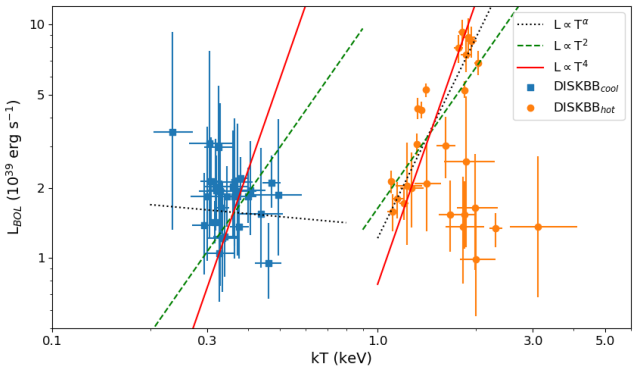

Figure 4.7: 0.001–10 keV (i.e. bolometric) luminosity versus temperature for both the cool DISKBB (blue points) and hot DISKBB (orange points) components with free column density, N_H (model: DISKBB+DISKBB).

4.4.2 Radius-luminosity relation

In order to test the consistency with the luminosity-temperature trends, we also estimated the mean inner radii for the DISKBB component for each of the two groups, using the normalisation factor with the formula $R_{in} = \sqrt{(norm * D_{10}^2)/cos\, i}$, where D_{10} is the distance to the source in units of 10 kpc and i is the inclination of the disc. The mean inner radii are $R_{in,1} \sim 1722\ (\cos i)^{-1/2}$ km and $R_{in,2} \sim 146\ (\cos i)^{-1/2}$ km (where subscripts 1 and 2 refer to the lower and higher temperature tracks, respectively), which correspond to $\sim 414\ R_S$ and $\sim 35\ R_S$ (where $R_S = 2GM/c^2$ is the Schwarzshild radius, assuming $M = 1.4\ M_\odot$).

Using the relation $L = A\sigma T^4$, we can also determine the emitting areas for each DISKBB component, as shown in Fig. 4.8. We note that, for the hot component, the size of the emitting area of the accretion disc is broadly constant (in units of R_{NS} =10 km, $\Delta R \sim 57\ R_{NS}$) for several observations. Instead, the emitting area for the cool component varies from $R_{min} \sim 180\ R_{NS}$ to $R_{max} \sim 1600\ R_{NS}$. This would agree with the expectations from a local increase in the accretion rate (Poutanen et al. 2007).

Using the formalism outlined in King & Lasota (2020) and assuming $20 < \dot{m} < 25$ (which is reasonable for the observed luminosity), we can also estimate the spherisation radius $R_{sph} \sim 70$–$87\ R_S$. We found that the inner radius for the cool component is larger than the spherisation radius, that is $R_{in,1} > R_{sph}$, which suggests that the cool component takes both the emission from the cool disc and the contribution from the wind in account. The inner radius of the hot DISKBB is instead smaller than the spherisation radius ($R_{in,2} < R_{sph}$), indicating that this component is likely reproducing the super-Eddington inner accretion flow within R_{sph}.

Our approach has made use of phenomenological models in order to describe the long-term spectral evolution of the source. Future work will benefit from adopting physically motivated models which account for the thick nature of super-Eddington discs and Compton scattering through the disc atmosphere.

4.5 Conclusions

In this paper we have presented the analysis of the X-ray emission spectrum of NGC 1313 X-2, a pulsating ultraluminous X-ray source, using all the available observations

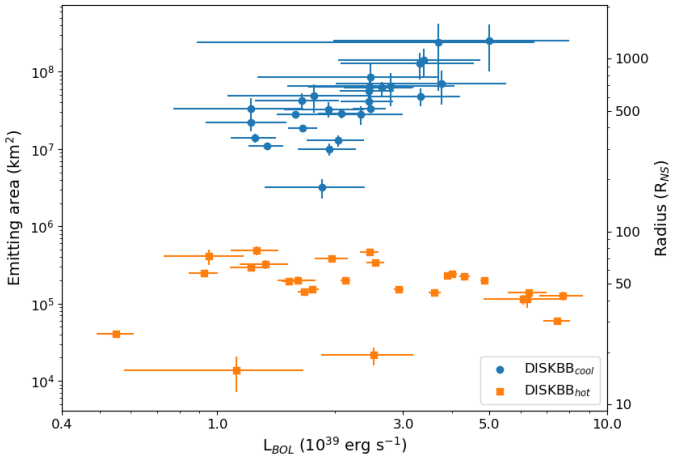

Figure 4.8: Left Y-axis: Emitting area versus luminosity for both the cool and hot DISKBB components (blue and orange points, respectively). Right Y-axis: Radius, in units of typical NS radius of 10 km, versus luminosity for both the cool and hot DISKBB components (blue and orange points, respectively).

performed by *XMM-Newton* between 2000 and 2017. With the aim of characterising the spectral shape and its long-term variability, we have tested various spectral models for all observations. Since pulsations have been detected, we know that the compact object is a NS. In order to reach high luminosities (up to 10^{40} erg s^{-1} in some observations), the compact object must be in a super-Eddington accretion regime.

The spectral model that provides the best description of the *XMM-Newton*/EPIC data consists of two multi-colour disk blackbody components plus an exponential cutoff powerlaw, as in Walton et al. (2018d). Similar to previous works, we find that the hotter of the two thermal components dominates the 1–10 keV band, and the cooler one is more relevant in the energy band below 1 keV. Furthermore, we found that the inner radius of the hot component is smaller than the spherisation radius, while the characteristic radii associated with the cooler component are all larger than the spherisation radius. In the framework of super Eddington accretion, this is strong evidence that the hotter component describes the dominant emission from the innermost region of the disc. Instead, the cooler component accounts for the emission from a larger region of the disc, outside the spherisation radius and the characteristic wind launching radius. Finally, we argued that the cutoff powerlaw component comes from the accretion columns onto the NS.

Most spectra show narrow residuals around ∼1 keV, which are likely associated with atomic emission and absorption lines produced by powerful outflows, as they are qualitatively similar to those seen in other ULXs that have been resolved and identified with the aid of dedicated high-resolution observations (see e.g. Pinto et al. 2020b). The luminosity and the temperature of each emission component evolves along L–T trends that deviate from those expected for some typical regimes such as the sub-Eddington thin disc of Shakura-Sunayev ($L \propto T^4$, for constant emitting area) or the advection-dominated disc ($L \propto T^2$). In particular, we obtain power indexes of $\alpha_H = 3.0 \pm 0.35$ and $\alpha_C = -3.9 \pm 1.0$ for the hotter and the cooler components, respectively. This implies a super-Eddington accretion regime and suggests a geometry closer to the funnel than a thin disk for the inner regions due to intense radiation pressure. Optically thick winds are also likely responsible for the scatter seen in Fig. 4.6.

This behaviour is qualitatively similar to the broadband spectral evolution seen in NGC 1313 X-1 and Holmberg IX X-1. The similar spectral evolution between these sources, where the flux above 1 keV increases significantly at higher luminosity, may indicate a common structure and evolution among archetypal ULXs.

Table 4.2: Best-fit parameters for the models tested in this work for Obs.ID:0803990201.

TBABS*(DISKBB+DISKBB+CUTOFFPL)			
Model component	Parameter	Unit	
TBABS	N_H	$[10^{22}cm^{-2}]$	0.28 ± 0.02
DISKBB	T_{in}	[keV]	0.25 ± 0.02
	norm		14^{+7}_{-5}
DISKBB	T_{in}	[keV]	1.13 ± 0.04
	norm		0.053 ± 0.007
CUTOFFPL	PhoIndex		0.59 (fixed)
	HighECut	[keV]	7.9 (fixed)
	norm	$[10^{-5}]$	$2.8^{+0.4}_{-0.5}$
χ^2/dof			314.91/259
TBABS*(DISKBB+DISKBB)			
Model component	Parameter	Unit	
TBABS	N_H	$[10^{22}cm^{-2}]$	$0.242^{+0.014}_{-0.013}$
DISKBB	T_{in}	[keV]	0.32 ± 0.02
	norm		$4.3^{+1.7}_{-1.2}$
DISKBB	T_{in}	[keV]	$1.36^{+0.03}_{-0.02}$
	norm		0.028 ± 0.002
χ^2/dof			336.86/260
TBABS*(SIMPL*DISKBB)			
Model component	Parameter	Unit	
TBABS	N_H	$[10^{22}cm^{-2}]$	$0.158^{+0.002}_{-0.004}$
SIMPL	Γ		$2.75^{+0.07}_{-0.02}$
DISKBB	T_{in}	[keV]	$0.56^{+0.01}_{-0.02}$
	norm		$0.62^{+0.09}_{-0.08}$
χ^2/dof			455.69/260
TBABS*(DISKBB+DISKPBB)			
Model component	Parameter	Unit	
TBABS	N_H	$[10^{22}cm^{-2}]$	$0.32^{+0.03}_{-0.02}$
DISKBB	T_{in}	[keV]	0.21 ± 0.02
	norm		30^{+37}_{-15}
DISKPBB	T_{in}	[keV]	$1.57^{+0.07}_{-0.05}$
	p		0.57 ± 0.02
	norm		0.008 ± 0.002
χ^2/dof			321.32/259

Table 4.3: Fractional variability measured using the average value of the EPIC-pn light curve segments for each observation with an exposure time of 40 ks and 1000 s bins.

Obs.ID	F_{var} mean (%)	HR mean
0405090101	6.06 ± 0.02	0.65 ± 0.03
0693850501	11.76 ± 0.07	0.62 ± 0.03
0693851201	0.748 ± 0.008	0.53 ± 0.04
0742590301	7.93 ± 0.07	0.61 ± 0.05
0742490101	3.26 ± 0.04	0.58 ± 0.07
0764770101	1.154 ± 0.002	0.49 ± 0.04
0782310101	12.17 ± 0.09	0.60 ± 0.07
0803990101	14.99 ± 0.04	0.60 ± 0.05
0803990201	12.93 ± 0.09	0.61 ± 0.05
0803990301	1.04 ± 0.04	0.52 ± 0.06
0803990401	1.91 ± 0.04	0.55 ± 0.06
0803990501	7.56 ± 0.16	0.55 ± 0.08
0803990601	4.79 ± 0.10	0.6 ± 0.1

Table 4.4: Pearson and Spearman correlation coefficients calculated for the trends between luminosity and temperature for both the cool and the hot DISKBB components (assuming the baseline model, i.e. DISKBB+DISKBB+CUTOFFPL).

Parameters	Pearson	Spearman
L_{hot}–T_{hot}	0.69	0.69
L_{cool}–T_{cool}	-0.44	-0.47

5

Timing analysis of the ULX NGC 1313 X-2

Summary

In order to place constraints on the accretion disc structure in a model-independent way, I have applied Fourier timing techniques to ULXs. In particular, I have studied the pulsating source NGC 1313 X-2, among the brightest and most variable ULXs and for which 10 full-orbit *XMM-Newton* observations are available along with other 10 shorter ones. For each observation, I extracted the time delays using the cross spectrum between the hard band and the soft band, which are related to the nature and geometry of the accretion flow. This work shows the detection of time lags with magnitudes of a few hundred seconds, whose origin could support the wind scenario. We observe soft lags unveiling faster reprocessing or multiple scatterings of hard photons in the outer disc and the optically-thick wind. A further hard lag is found at low frequencies, which is likely associated to slow propagation of fluctuations moving inward the disc.

5.1 Introduction

Ultraluminous X-ray sources (ULXs) are off-nuclear point sources with an isotropic luminosity that exceeds 10^{39} erg/s, which is the Eddington luminosity limit for a standard 10 $M_\odot$ black hole, and therefore represent the most extreme among X-ray binaries (for a recent review see Pinto & Walton 2023).

Several hypotheses have been proposed to explain the high luminosity of these sources. In the past, it was speculated that the extreme luminosity exhibited by ULXs was produced by an intermediate-mass black hole (IMBH) accreting at sub-Eddington rates (Colbert & Mushotzky 1999). Others scenarios invoked extreme geometrical beaming in Eddington limited stellar-mass BH or super-Eddington accretion onto such objects (King et al. 2001). However, ULX field was revolutionised after the discovery of pulsations, which provided unambiguous evidence in support of a ULX hosting a neutron star (NS, see Bachetti et al. 2014).

At the moment, six persistent ULXs are known to exhibit pulsations (Israel et al. 2017a,b; Fürst et al. 2016; Carpano et al. 2018; Sathyaprakash et al. 2019; Rodríguez Castillo et al. 2020). It is not straightforward to distinguish between BH and NS accretors based on the spectral analysis alone (Pintore et al. 2017, Koliopanos et al. 2017 and Walton et al. 2018a). This issue is indeed common also among Galactic Eddington-limited X-ray binaries where several indicators are used such as pulsations, quasi-periodic oscillations and Doppler-shifted lines in optical spectra (e.g. Remillard & McClintock 2006, Done et al. 2007). However, from all ULXs with sufficient statistics $\sim$ 25% at least host NSs. Given that pulsations are transient and require a favourable geometry for the detection (misaligned magnetic field, B, and disc axis coupled with a low viewing angle enabling the line of sight to access the inner accretion column) it is natural to assume that the NS fraction of the ULX population is higher than 25% and possibly even the majority, particularly because NS-XRBs tend to be more abundant than BH-XRBs in galaxies similar to ours.

ULXs represent an accretion state which differs from both the soft and hard states of Eddington limited X-ray binaries, called *ultraluminous state* (Gladstone et al. 2009). In particular, ULX broadband spectra exhibit a strong curvature in the $\sim$ 2–10 keV band before breaking to steep spectra above $\sim$ 10 keV and often a soft excess below 2 keV (Sutton et al. 2013). Moreover, the combination of broadband spectrometers (0.3–78 keV, by e.g. simultaneous observations with *XMM-Newton* and *NuSTAR*), showed that for - most ULXs - it is necessary to use at least two-blackbody components to reproduce the spectral shape in the 0.3–10 keV band. In this scenario, the first component (with typical temperatures $\sim$ 0.2–0.5 keV) describes the emission around the spherisation radius of the disc (i.e. where the flow becomes locally super-Eddington and a radiatively driven wind is launched (Pinto et al. 2016; Kosec et al. 2018a, 2021). The higher temperature

component (with temperature ∼ 2–4 keV) originates from the innermost part of the disc. A third, harder, component with a power-law-like shape appears to dominate above 10 keV in HUL spectra, albeit showing weaker variability than that seen in the disc-like components below 10 keV (see, e.g., Walton et al. 2020).

Time lags and, in general, Fourier analysis is a common practice in time series of X-ray binaries and active galactic nuclei where it revealed crucial features that determined the structure of the accretion discs and the C.O. mass in a model-independent way and at different orders of magnitude of masses (e.g. Cackett et al. 2018, Fabian et al. 2009).

With this aim, despite the low count rate and low short-term (∼ hours) variability of most ULXs, several authors showed evidence of time lags from the soft X-ray band in 4 ULXs (De Marco et al. 2013, Kara et al. 2020, Pinto et al. 2017, Mondal et al. 2021) and a hard-band lag (Pintore et al. 2021).

In this paper, we extend the spectral-timing studies of NGC 1313 X-2, by a detailed analysis of the variability and the timing properties, and use them as diagnostics of the accretion state of the source.

This paper is organised as follows, in Section 5.2, we report the *XMM-Newton* data used in this work and the data reduction and in Section 5.3 the timing analysis of observations where the source shows more significant variability. The discussion and conclusions are provided in Section 5.4 and 5.7.

5.2 Observations and data reduction

The two ULXs in the NGC 1313 galaxy were the subject of an extensive campaign with *XMM-Newton* (PI: Pinto) which boosted even further an already reach archive of observations. We analysed the public archival *XMM-Newton* data of all the high signal-to-noise observations of NGC 1313 X-2 between 2000 and 2017. A detailed spectral analysis of NGC 1313 X-2 was extensively described by Robba et al. (2021) and has been reported in Chapter 4.

While all ∼ 2 Ms of data were analysed, only 5 observations showed sufficient variability (fractional root-mean square, $F_{var} \gtrsim 10\%$) to detect time delays. In this paper, we focus on the timing analysis of these observations (see Table 5.1) of the pulsar NGC 1313 X-2.

The data analysis was performed using the *XMM-Newton Science Analysis System* (SAS) version 19.1.0 and the calibration files of October 2022.[1]

We analysed the data from the EPIC-pn detector only as it has nearly three times larger photon-collective area than each MOS detector and higher timing resolution. As recommended from the standard procedure, we selected single and double events (PATTERN $\leq$ 4). These are subsequently filtered for the flaring particle background, choosing the standard cutting threshold in the light curves above 10 keV (count rate < 0.4 c/s). We produce a circular source extraction region of 30″ in radius, and a background region of 50″ in the same chip and avoiding the well-known copper ring. The light curves were extracted using 100s time bins and background corrected using the SAS task EPICLCCORR.

Table 5.1: *XMM-Newton* observations of NGC 1313 X-2 used in this paper.

Obs.ID [(1)]	Date [(2)]	Exposure time (pn) [(3)] (s)
0405090101	2006-10-15	121190
0742590301	2014-07-05	60040
0782310101	2016-10-08	88041
0803990101	2017-06-14	134142
0803990201	2017-06-20	130841

Notes: [(1)] observation identifier; [(2)] observation date (yyyy-mm-dd), [(3)] exposure time corrected for solar flares.

5.3 Timing Analysis

With the aim of understanding the mechanism which produces the ULX luminous spectra and their broad, thermal-like, shape, we searched for time lags between different energy bands and their connection with the overall source spectral variability, as done by a few authors for other ULXs (e.g. De Marco et al. 2013, Pinto et al. 2017 and Kara et al. 2020) and more frequently in high-statistic time series of Galactic XRBs. Following the procedure outlined in (Uttley et al. 2014), we performed a Fourier timing analysis, by

[1] https://www.cosmos.esa.int/web/xmm-newton/ccf-release-notes.

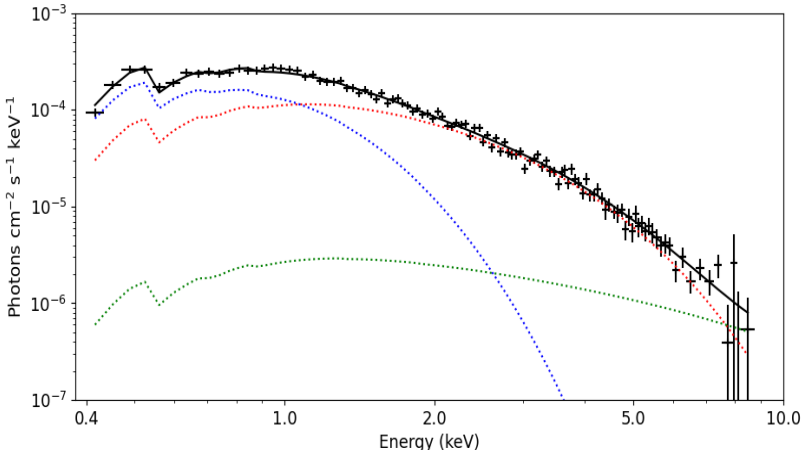

Figure 5.1: *XMM-Newton* spectrum of Obs.ID 0693851201, fit with a demonstrative model of two disc blackbody components (hot and cold DISKBB, in red and blue line respectively) plus a CUTOFF POWERLAW (green line).

using STINGRAY version v1.1 (see Huppenkothen et al. 2019; Huppenkothen et al. 2019), which is an open source spectral-timing Python software package for astrophysical data analysis. The general approach and computation are discussed in detail previously in Chapter 1. However, STINGRAY has rarely been applied to ULX time series with much lower statistics than Galactic XRBs. So far we are not aware of any robust detections and discoveries of soft X-ray lags in ULXs with this code and, therefore, we have validated the code applicability by testing it on a well-known ULX for which a highly significant detection was achieved, i.e. NGC 5408 X-1 (see Heil & Vaughan 2010, De Marco et al. 2013). This analysis is detailed in Appendix B.

NGC 1313 X-2 spectra are characterised by two dominant thermal components in the 0.3–10 keV band as for most ULXs (see Fig. 5.1). A detailed spectral analysis of the broadband continuum emission is provided in Robba et al. (2021).

For each observation, we extracted light curves in the whole band (0.3–10 keV) and in two different bands (i.e. soft 0.3–1.2 keV and hard 1.2–10 keV), with a time bin size of 100s. Fig. 5.2 shows the EPIC-pn light curves of the source in the band 0.3–10 keV with the most variable observations, for which we performed this analysis, coloured according to the hardness ratio, HR, defined as the ratio between the counts in the 1.2–10 keV and 0.3–10 keV energy bands. We chose to define these two bands, which select the soft and hard main spectral components of the X-ray spectrum of the source, as shown in

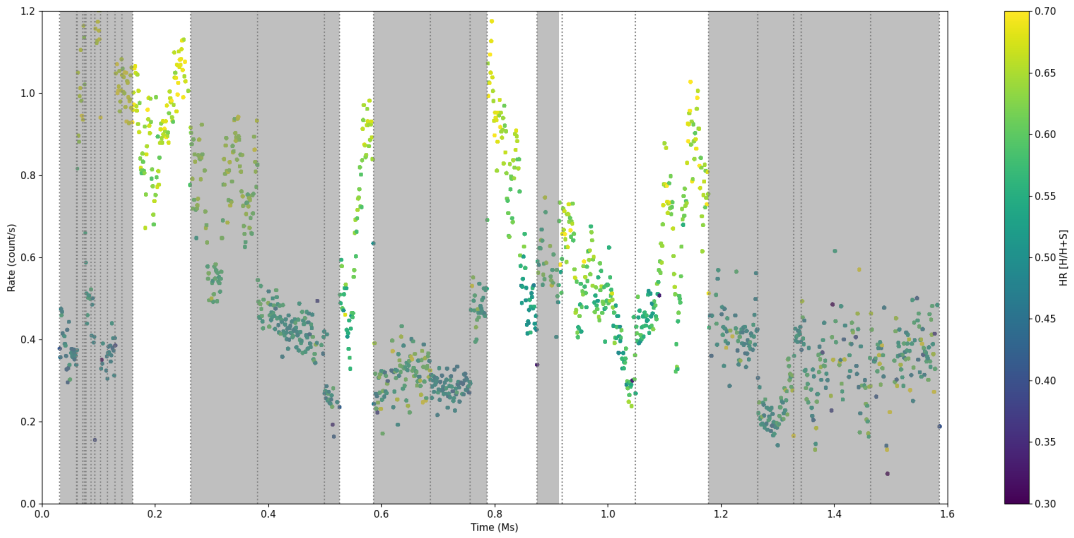

Figure 5.2: *XMM-Newton* EPIC-pn light curves of the five analysed observations of NGC 1313 X-2 in the energy band 0.3–10 keV. The colour is coded according to the hardness ratio, i.e. the ratio between the counts in the 1.2–10 keV and 0.3–10 keV energy bands. Vertical grey-dashed lines separate the individual observations, which have been attached for visual purposes.

Fig. 5.1 (see Robba et al. 2021), and to search for correlated variability between them. For ObsID 0405090101, we decided to consider only the first 30ks of the observation, because most of the variability occurs in the first part of the light curve following the approach adopted by Kara et al. (2020) for NGC 1313 X-1.

To explore the nature of the periodic pattern, we constructed the power density spectrum (PSD) from the extracted light curves of each observation. The PSD was extracted in the soft, hard and total energy bands. First, we split the soft and the hard band light curves into smaller segments (with a length $\sim$ 8000–10000 s), which allow us to sample the range of temporal frequencies $\nu \sim 0.000125$–0.01 Hz and 0.0001–0.01 Hz. The chosen segment length is a compromise between having a wide range of fluxes (smaller duration segments give a wider range of mean fluxes) and having better low-frequency coverage (longer segments give better low-frequency coverage). Moreover, it must also be such that it is not dominated by Poisson noise. Next, we calculated the PSD of each segment, averaged over all segments and rebinned, adopting bins of length $d\nu_j = d\nu_{j-1}(1 + f)$, with f = 0.1. We chose a fractional rms-squared normalisation,

which makes the Poisson noise level = 2 / mean rate (where mean rate is equal to the mean value of the light curve counts). The resulting averaged PSDs are shown in Fig. 5.3.

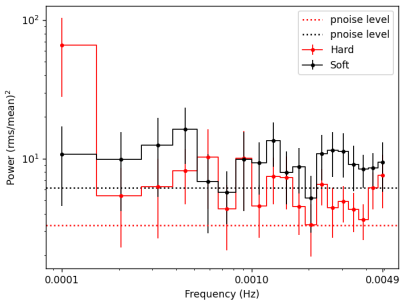

(a) 0405090101

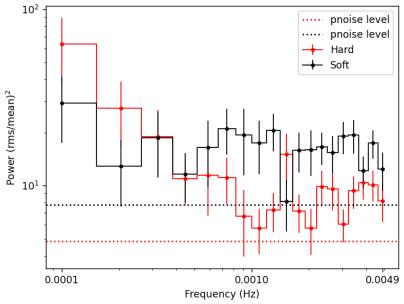

(b) 0742590301

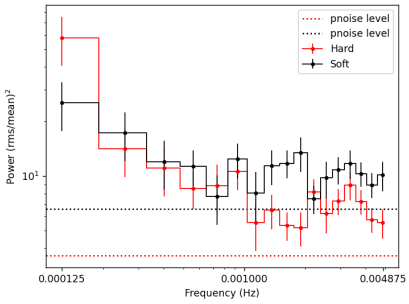

(c) 0782310101

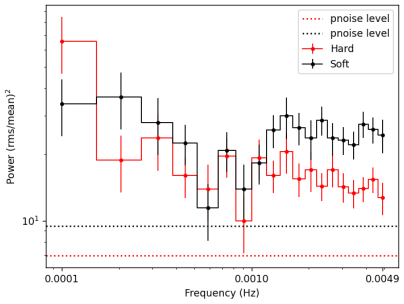

(d) 0803990101

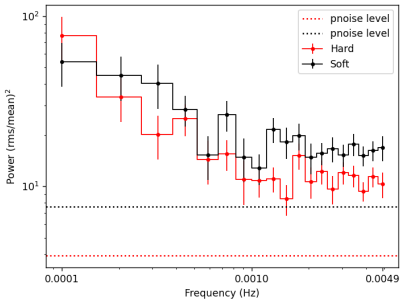

(e) 0803990201

Figure 5.3: PSD of each observation in the hard (1.2–10 keV) and soft (0.3–1.2 keV) energy bands (from left to right). Dotted lines represent the value of the Poisson noise for each observation.

As for PSDs, we measured and averaged the cross-spectra and we computed the frequency-dependent time lag between the soft band and the hard band as follows:

$$\tau_j = \frac{\phi_j}{2\pi\nu_j} \tag{5.1}$$

for a phase angle ϕ_j derived from the imaginary component of the complex cross spectrum and a frequency ν_j. We follow the convention that the negative lag means that the soft X-ray photons lag behind the hard X-ray photons and vice versa for positive lag.

In order to measure the degree of linear correlation between two light curves as a function of Fourier frequency, we computed the coherence between the 0.3–1.2 keV and 1.2–10 keV light curves, for each observation, using the following formula:

$$\gamma^2 = \frac{C_{xy,j}}{C_{x,j}C_{y,j}} \tag{5.2}$$

Here, $C_{xy,j}$ corresponds to the real part of the unnormalised cross-spectrum, and $C_{x,j}$ and $C_{y,j}$ correspond to the analogous squared amplitudes of the power spectrum for each individual light curve.

5.4 Results and discussion

In this work, we carried out a detailed timing analysis of the archival *XMM-Newton* observations in which the pulsating ULX NGC 1313 X-2 showed strong variability (i.e. F_{var} above 10%). This is one of the few ULXs for which we know the nature of the compact object and the accretion rate, which could help us to better understand the whole variability process.

For the selected observations, we computed the averaged PSD from the light curves, to reduce the noise. Therefore, we chose two smaller segment sizes (8000 s for Obs.ID 0782310101 and 10000 s for the rest) and a fractional rms-squared normalisation. From PSDs in Fig. 5.3, we note a weaker variability above ~ 0.001 Hz.

To derive the frequency-dependent (phase) lag between two bands, we extracted the cross-spectrum between them. The cross-spectra are normalised in the same way as the PSD. To reduce the effects of the noise, the cross-spectra are averaged over Fourier frequencies in a given frequency bin, as well over multiple light curve segments.

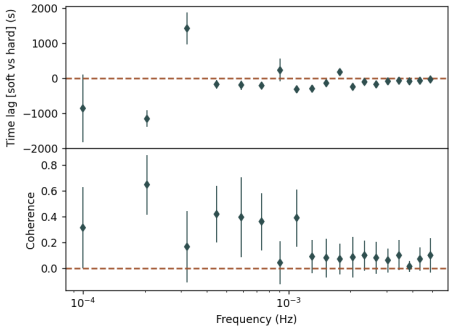

(a) 0405090101

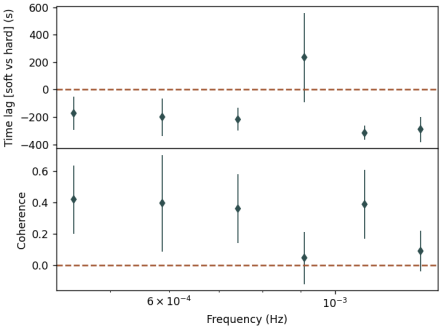

(b) 0405090101 (4×10^{-4}-10^{-3} Hz)

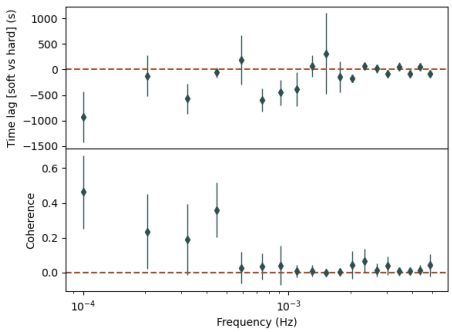

(c) 0742590301

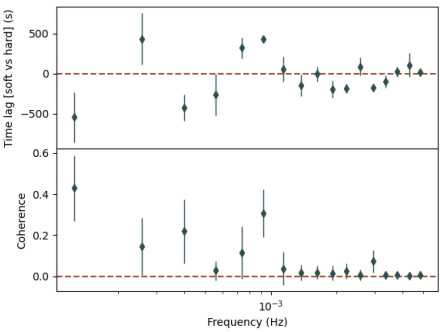

(d) 0782310101

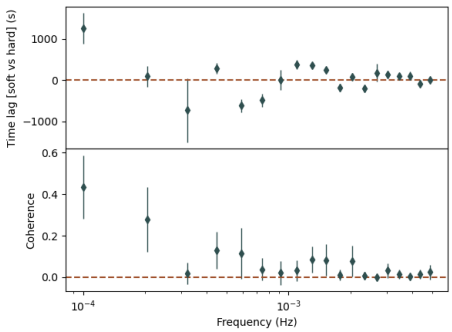

(e) 0803990101

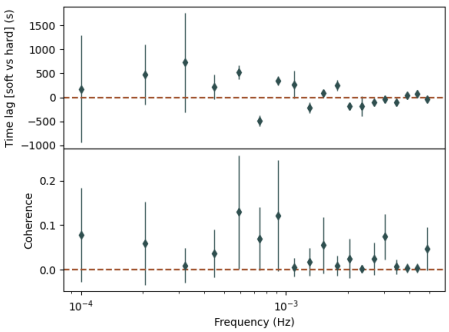

(f) 0803990201

Figure 5.4: *Upper panels:* Lag-frequency spectra between the soft [0.3–1.2 keV] and hard [1.2–10 keV] energy bands. *Lower panels:* Coherence between the hard and soft bands.

Using the phase lag of the resulting cross-spectra (i.e. the argument of the complex cross-spectrum vector), the time lags, for each observation, were obtained (see Fig. 5.4).

In general, we considered only the trend obtained for the frequency $\lesssim 0.001$ Hz, since above this value the intrinsic coherence between the two bands dramatically drops to values consistent with zero.

Fig.5.4 shows the time lag spectra as a function of frequency. We observe a delay that varies over time, in particular, a negative lag (soft lag) of $\sim$ 500 s (in Obs.ID 0405090101) and a positive lag (hard lag) with the averaged value of $\sim$ 700 s (in Obs.ID 0803990101).

In Fig.5.4 (b) we show a zoom of the Obs.ID 0405090101, in the frequency range $4{\times}10^{-4}$ – 10^{-3} Hz, where the soft lag is evident with a coherence > 0.4.

Soft lags in super-Eddington accreting compact objects are commonly believed to be caused by the wind which downscatters or softens a substantial fraction of the photons produced by the inner disc. However, in Eddington-limited sources, down scattering can also simply occur in the outer disc as shown by the presence of fluorescence lines and continua (a.k.a. *reflection*) in many stellar-mass compact objects and supermassive black holes (e.g. García et al. 2022 for reflection in NS and Fabian & Ross 2010 for a review). Instead, the interpretation of hard lags in these sources and, more in general, X-ray binaries and active galactic nuclei (AGN) invokes the mechanism of the inward propagation of mass accretion rate fluctuations (Arévalo & Uttley 2006). In the latter case, we expect that the soft photons, produced by the outer regions of the accretion flow, to lead the photons produced in the inner regions.

Since the observed time delays are quite long ($\sim$ 500–700 s) if compared to the sub-second delay expected from simple reverberation in the outer disc for a stellar-mass compact object (e.g. Kara et al. 2019), they may be attributed to the difficulty that photons have in escaping a ticker disc, due to multiple scattering events. Generally, this is the case for low efficiency discs ($\eta \sim 1 - 3\%$), expected above Eddington-limit (see Huang et al. 2023 and Fiacconi et al. 2017).

Moreover, we found a soft lag of $\sim$ 300 s, in the range (1–6) $\times\ 10^{-4}$ Hz in Obs.ID 0782310101. Also for Obs.ID 0742590301, we note a soft delay of the order of hundreds of seconds, but for coherence $\gtrsim 4 \times 10^{-4}$ Hz, it becomes comparable to zero.

We have not identified significant time delays in Obs.ID 0803990201, where the error bars are large and the coherence is less than 0.2, almost consistent with zero for

most frequencies.

5.5 Comparison to other ULXs

In Fig. 5.5, we plot the 0.3–10 keV X-ray luminosity versus soft (circle marker) / hard (square marker) lag amplitude of ULXs detected in similar energy bands.

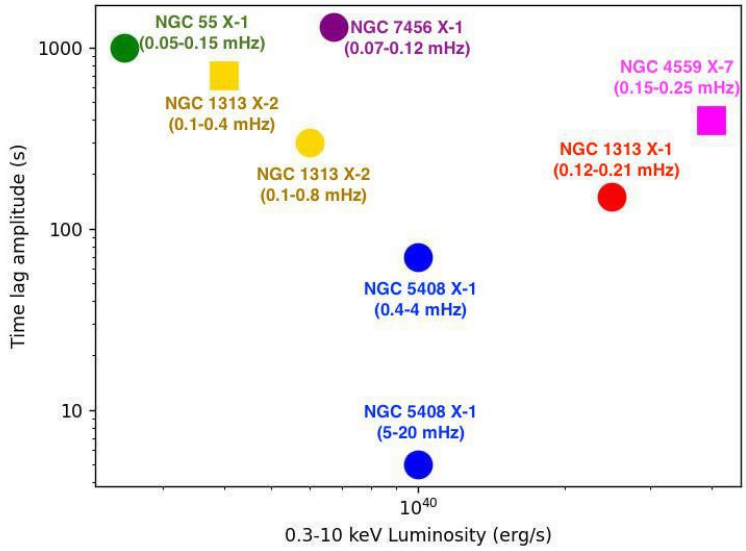

Figure 5.5: Comparison of time lags seen in several ULXs: NGC 5408 X-1 (De Marco et al. 2013 and Heil & Vaughan 2010), NGC 55 X-1 (Pinto et al. 2017), NGC 1313 X-1 (Kara et al. 2020), NGC 4559 X-7 (Pintore et al. 2021), NGC 7456 X-1 (Mondal et al. 2021) and NGC 1313 X-2 (this work). Circle markers indicate the soft lag amplitude while square markers indicated the hard lag amplitude.

To date, five ULXs exhibit time lags: NGC 5408 X-1 (De Marco et al. 2013), NGC 55 X-1 (Pinto et al. 2017), NGC 1313 X-1 (Kara et al. 2020), NGC 4559 X-7 (Pintore et al. 2021) and NGC 7456 ULX (Mondal et al. 2021). Variability timescales and the amplitudes of the lags of these ULXs are very different: from ~ 5s (in NGC 5408 X-1) to ~ 1000s (in NGC 55 X-1), which might point towards different mechanisms.

As suggested by the covariance spectra (i.e. the spectrum of the emission that contributes to the lags), the emission contributing to the delays is mainly associated with

the hotter component of the two thermal-like components, generally attributed to the inner accretion flow.

Given the vast differences in lag timescales, the exact mechanism responsible for the observed delays is not clear. There is no evidence of any correlation with luminosity or spectral hardness (see Kara et al. 2020). In three ULXs where delays were found, winds in the form or resolved emission and absorption lines were also detected. However, residuals in the CCD spectra around 1 keV are found in all of them, suggesting that the winds are ubiquitous and may perhaps contribute to the mechanism producing the lags.

It is possible to note that although there is a considerable variation in the amplitude of time lags (by up to three orders of magnitude), in general, the amplitude is about a few to a few tens per cent of the characteristic variability timescale, suggesting a degree of common origin. In particular, NGC 5408 X-1 and NGC 1313 X-1 both show soft delays that are $\sim$ 5% of the average variability timescale. They also have similarities in their covariance spectrum, which is harder than the mean, time-integrated energy spectrum (Hernández-García et al. 2015, Middleton et al. 2015a). We observe that the lag amplitude in 5408 X-1 is an order of magnitude smaller than that seen in other ULXs. However, Heil & Vaughan 2010 found a longer soft lag delay ($\sim$ 70 s), analysing longer time scales, which would indicate different ongoing processes in separated regions.

A slightly different behaviour is shown by NGC 55 X-1, which exhibits a lag that is $\sim$ 10-30 per cent of the variability timescale. In addition, its covariance spectrum is more similar to the average spectrum, if compared to the other ULXs, suggesting that the soft component - and perhaps the wind - is providing a larger contribution to the lag. However, as we can see from Fig. 5.5, the amplitude of this delay is comparable to that found for NGC 7456 X-1, in a similar frequency range (0.05–0.15 and 0.07-0.12 mHz in NGC 55 X-1 and NGC 7456 X-1, respectively).

NGC 4559 X-7 is the first ULX where low-frequency hard lags have been observed. Pintore et al. (2021) suggest that such lags can be explained in terms of propagation of mass accretion rate fluctuations (responsible also for the flares observed in this source).

In contrast to other sources, NGC 1313 X-2 exhibits two distinct delays during two separate observations, which correspond to two distinct states. It is reasonable to assume that there is a link between the presence of the lags and the accretion rate. Specifically, during a flare phase, we observe a soft lag, similar to the behaviour observed in NGC 1313 X-1, and during a slightly low flux phase, we found a hard lag. The appearance of a soft

lag in the high state may suggest that the bright inner disc (or the NS magnetosphere) is irradiating the outer disc / wind cone. While the hard lag in the lower and softer (albeit still super-Eddington) regime is an indication of a fainter inner disc and therefore a significant contribution to the lag from the inward propagating fluctuations.

Unlike NGC 5408 X-1, no QPOs are found such as NGC 55 X-1 and NGC 1313 X-1, while pulsations were found in NGC 1313 X-2 indicating a NS accretor. For the other ULXs, it is difficult to identify the accretor although there are indications for stellar-mass BHs in NGC 5408 X-1 and NGC 55 X-1 based on their broadband and wind properties (Fiacconi et al. 2017; Barra et al. 2022).

5.6 Comparison to Galactic XRBs and AGN

Comparing the properties of ULXs to those of Galactic black hole X-ray binaries (BH XRBs) can provide insight into the nature of these sources. The observed variability in BH XRBs is distributed over a wide range of time scales, from long-term variations of days-months to faster changes in milliseconds (for more detail see De Marco et al. 2022).

Detailed studies of X-ray lags in BH XRBs were carried out particularly in the hard states, thanks to high count rates (Uttley et al. 2014). The presence of these lags strongly depends on the energy and the frequency. In particular, at low frequencies we observe hard lags, instead at high frequencies soft delays, the so-called "X-ray reverberation lags". These lags, which are due to the path length difference between direct and reflected emission, have been explained as the result of the thermal response of the disc after rapid variations of the primary hard X-ray irradiating flux.

We do not expect that the soft X-ray time lags detected in NGC 1313 X-2 are due to reverberation, as they are orders of magnitude longer than those observed in XRBs.

The same type of lags seen in hard-state BH XRBs was also observed in active galactic nuclei (AGN). However, AGN variability can be measured at low frequencies (e.g. $\nu \gtrsim 10^{-4}$ Hz), where BH XRBs variability appears to be largely suppressed. After the first significant detection (Fabian et al. 2009), there is now observational evidence indicating that X-ray reverberation is a prevalent characteristic of bright, radio-quiet AGN. To date, over 30 sources have been found to have lags attributable to X-ray reverberation, using long *XMM-Newton* and *NuSTAR* observations (De Marco & Ponti

2019). The different time scales between AGN SMBHs and XRB BHs are due to the fact that accretion discs in AGN are much larger than those in XRBs. Moreover, for AGN the disc thermal emission peaks in the UV (e.g. around 10 eV), instead for XRBs the peak is in the X-ray band (e.g. around 1 keV). AGN time lags are as long as those observed in NGC 1313 X-2, but in the latter case we expect a stellar-mass compact object (a neutron star). This implies a different physical process such as multiple scattering in a thick disc-wind cone as confirmed by the lower coherence in ULX time series.

5.7 Conclusions

In this work, we have carried out a comprehensive analysis of the X-ray variability of the ULX NGC 1313 X-2. We present the discovery of a soft lag of $\sim$ 500 s and a hard lag of $\sim$ 700 s, in two different *XMM-Newton* observations.

The origin of these lags in ULXs is not well-understood, as for other ULXs, we interpret them in the context of a unified super-Eddington outflow model. Indeed, we expect that a fraction of the inner (hard) photons can be downscattered by the wind, resulting in a delay of the softer photons compared to the harder ones. This is also observed in other ULXs, such as NGC 55 X-1 and NGC 1313 X-1, for which blueshifted absorption lines were detected in the high-resolution soft X-ray spectra. Instead, the interpretation for hard lags is generally associated with that proposed for the X-ray binaries and AGNs. It is common to associate them with the inward propagation of fluctuations in accretion flow, which leads soft photons to respond before the inner regions.

In addition, the length of the observed delays ($\sim$ 500–700 s) may suggest that photons undergo multiple scattering events. This could be due to the difficulty that photons have in escaping a thicker disc, as expected in the super-Eddington accretion.

However, due to the limited spectral-timing data for ULXs, it is challenging to determine the origin of the lags. Increasing the observation time and improving the signal-to-noise ratio would allow access to lower and higher frequencies, providing more accurate estimates of the frequency and energy dependence of the lags. These constraints will be crucial for improving our knowledge of ULXs, but this may require larger X-ray missions in the future.

Data Availability

All of the data and software used in this work are publicly available from ESA's *XMM-Newton* Science Archive (XSA[2]) and NASA's HEASARC archive [3].

[2]https://www.cosmos.esa.int/web/xmm-newton/xsa
[3]https://heasarc.gsfc.nasa.gov/

6

Conclusions and future research

In the first section of this concluding chapter, I discuss the results of the research chapters of this thesis. The second provides a comparison with other types of systems such as Galactic binary systems and AGN. Finally, I describe future perspectives of research that I would like to follow and the new generation of X-ray observatories that will transform the field of accretion physics in the coming years.

6.1 Main results

Super Eddington accretion is one of the most interesting and extreme processes, not yet fully understood, in the life of black holes and neutron stars, with a significant impact on their evolution. Ultraluminous X-ray sources (ULXs) are the ideal systems in which we can investigate this accretion regime owing to their extreme luminosities, above the Eddington limit of a stellar-mass black hole ($\sim 10^{39}$ erg/s) with their spectra peaking in the X-ray band, which is less subject to interstellar absorption than the UV band where SMBH spectra peak.

Unfortunately, estimating the actual number of ULXs per galaxy (and therefore the typical ULX-phase length in an XRB) is challenging due to several factors, including their variability, transient behaviour, viewing angle, and local obscuration. Long-term monitoring of the host galaxies is indeed necessary to enhance the probability of detecting transient ULXs, and deep observations can provide accurate measurements of the source spectral shape and luminosity, which are essential for characterising the nature and properties of ULXs. In particular, by studying the evolution of the spectral components

over time, it is possible to investigate changes in the accretion rate, the geometry of the accretion flow, and the presence of outflows or winds.

Broadband X-ray spectral analysis and advanced Fourier timing techniques of several ULXs have been used to perform this research.

Despite decades of studies, the physics of super-Eddington accretion is not yet well understood. Several open questions remain answered: *Are ULX spectral transitions driven by stochastic changes in the wind or variations in the accretion rate/geometry? What is the fraction of matter lost into the wind and, therefore, the net accretion rate onto the compact object? What is the fraction of BH-NS powered ULXs? Are there any spectroscopic differences amongst them?* This thesis aims to find and provide a solution to some of these problems.

I worked on three different projects to focus on different aspects of the broad and complex topic of ULX super-Eddington accretion, i.e. transient nature (Chapter 5), broadband spectral shape (Chapter 4) and timing properties (Chapter 3).

I have studied the X-ray emission from the population of X-ray sources in the galaxy NGC 55, thanks to recent, deep, *XMM-Newton* observations which were awarded to look for changes in the spectral continuum and narrow lines produced by the wind in NGC 55 ULX-1. I carried out a source detection on the X-ray images, resolving the X-ray sources hosted in this galaxy. Among the brightest sources detected, I report the identification of the new transient ULX-2, which was previously reported as a transient X-ray source with a luminosity of a few 10^{38} erg/s, but I found that it exceeds the 10^{39} erg/s threshold in multiple epochs, as shown by *Swift* data, revealing its ULX nature (see Fig. 6.1). The X-ray spectrum can be well described using a model with two thermal components, as often found in ULXs, and fits in the class of the ULXs with soft spectra or SUL sources.

To understand the structure of the accretion disc, I studied the spectral evolution over two decades of the pulsing ULX NGC 1313 X-2. I chose this ULX because it is characterised by a remarkable spectral variability in both luminosity and spectral shape and the compact object is known to be a NS (which helps to estimate the absolute accretion rate). The primary goal was to determine the shape and nature of the dominant spectral components by investigating their variability with the changes in the source luminosity. Among the different spectral models tested, the one that provides the best description of the X-ray spectra consists of two thermal black-body components with temperatures that differ by up to an order of magnitude plus an exponential cutoff power

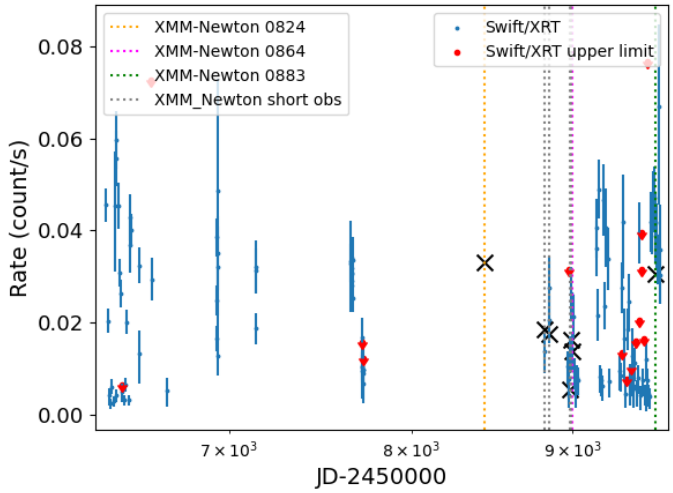

Figure 6.1: 0.3–10 keV long-term *Swift*/XRT light curve of NGC 55 ULX-2, with the dates of the *XMM-Newton* observations indicated by vertical dotted lines and the equivalent XRT count rates indicated by black 'X'.

law. In the framework of super-Eddington accretion, the hotter and brighter thermal component describes the emission from the super-Eddington inner disc and the cutoff power law describes the contribution from the accretion column of the neutron star. Instead, the cooler component describes the emission from the outer region of the disc close to the spherisation radius and the wind launching region.

Since it is crucial to understand the behaviour of thermal components, I studied how they evolve in a luminosity-temperature diagram (see Fig. 6.2). By examining the total luminosity and temperature parameter resulting from the spectral fit for different components, I compare the resulting L–T^{α} trends with those from theoretical models, such as the sub-Eddington thin disc of Shakura-Sunayev ($L \propto T^4$) or the advection-dominated disc ($L \propto T^2$). I found a negative trend in the L–T relation for the cool component, which can suggest that some of the variability is likely due to the wind detected with doppler-shifted lines. Moreover, the high luminosity observed at low temperature can be caused by the expansion of the photosphere of the disc (Poutanen et al. 2007). Instead, the L–T relation for the hotter component is somewhere in between the first two theoretical scenarios hinting at a milder thickening of the disc.

Finally, with the aim to determine the accretion disc structure in a model-independent

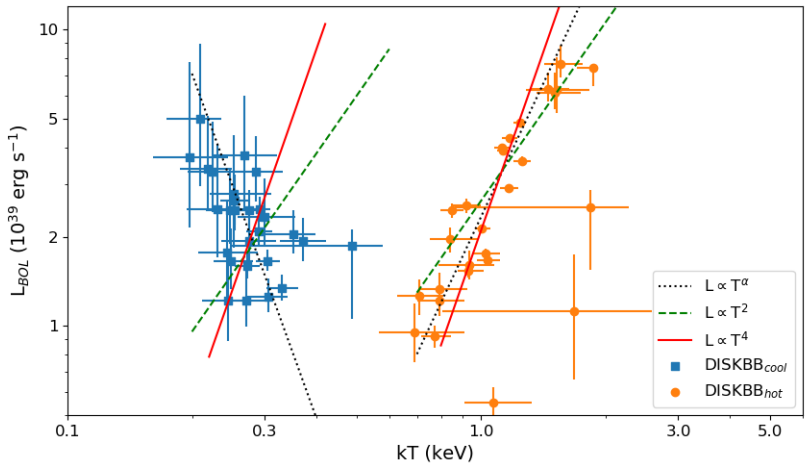

Figure 6.2: 0.001–10 keV (i.e. bolometric) luminosity versus temperature for both the cool DISKBB (blue points) and hot DISKBB (orange points) components with free column density, N_H (model: DISKBB+DISKBB+cutoffpl).

way, in the last project, I applied Fourier timing techniques to ULXs. In particular, I have worked on the observations of the pulsating NGC 1313 X-2. To better understand the behaviour of ULX-2, I identified the observations where the source showed some variability and I computed the power spectra, cross spectra, coherence and time lag spectra between energy bands whose photons are produced in different regions of the accretion disc. In particular, I found time delays between the soft and the hard band (0.3–1.2 and 1.2–10 keV, respectively). Soft lags at high frequencies are thought to arise from the reprocessing of the inner disc photons by the wind or the outer disc, which results in the soft photons lagging behind the hard ones. On the other hand, hard lags at low frequencies are thought to arise from the inward propagation of mass accretion rate fluctuations. The exact physical mechanisms that give rise to lags are still not well understood and are an active area of research. However, the time lags of $\sim$ 500 s detected in NGC 1313 ULX-2 confirm the presence of a genuinely thick super-Eddington disc.

6.2 Comparison with Galactic binary systems

XRBs spectra display a rich variety of spectral shapes, the low/hard and the high/soft state, mainly described by a disc thermal emission at lower energies ($kT \sim 1$ keV)

and a Comptonization component at high energies, the "corona" (often characterised by electron temperatures $kT_e \sim$ 20–100 keV). In contrast to the ULXs, spectra extend well beyond 10 keV, reaching around ~ 100 keV. In general, during the "hard state" the corona dominates the observed X-ray spectrum and persistent radio jets are seen, along with cool winds in the optical band at a few hundred km/s. Instead during the "soft" state the accretion disc dominates, and winds are often observed. During an outburst, the XRBs exhibit both strong flux and spectral variability. The transitions from the hard-to-soft and soft-to-hard do not occur at the same luminosities (see Fig 2.2, in Chapter 2).

ULXs spectra, on the other hand, are characterised by a strong curvature in the ~ 2–10 keV band and very steep spectra above ~ 10 keV (see Chapter 2). They could be considered as an extreme of the soft state of the XRBs, with a high accretion rate and faster winds caused by higher radiation pressure.

NS XRBs display magnetic field intensities B spanning at least the range from $\sim 10^8$ to several 10^{13} G, and beyond for magnetars. NS ULXs with high magnetic fields, i.e. B ~ 10^{12-14} G could potentially be expected from bright sources such as M 82 X-2 and NGC 5907 X-1. A large fraction of the ULX population could be host NSs that do not exhibit pulsations because at high accretion rates the magnetic field could be buried over time and favourable orientations of the binary systems are required to see pulsations. Indeed, there are similarities in the spectra between ULX with/without pulsations.

The pulsar ULXs typically have periods covering ~ 1–30 s (for more detail see King et al. 2023), while Galactic X-ray pulsars can reach periods even on the order of ~ ms. Furthermore, many of these PULXs tend to spin up at extremely high rates, such as NGC 300 X-1 (Carpano et al. 2018). It is important to note that, from the measure of the period derivative ($\dot{P}$), it is possible to obtain an upper limit of the mass transfer rate although there are caveats due to the short time span (Bachetti et al. 2022).

From the study of the variability of the accreting compact objects, time lags of the order $\lesssim$ second have been detected (e.g. Uttley et al. 2014). In several BH XRBs we observe soft X-ray lags likely due to reverberation, which consists of the reprocessing of the hard X-ray photons in the disc. Instead, hard lags are generally interpreted in terms of the propagation of fluctuations. Compared with XRBs, ULXs usually show long (soft and hard) time lags (e.g. Kara et al. 2020, Pinto et al. 2017), which can be difficult to attribute only to reverberation. Considering the ~ 500 s time lag observed for NGC 1313 X-2, we expect multiple scattering in the disc caused by the thick very thick and

possibly turbulent disc structure expected for ULXs.

6.3 Future perspectives

It is not easy to distinguish between BHs and NSs, based only on spectral properties. There are however several techniques to determine the nature of the compact object hosted by these systems, such as detecting pulsations and determining cyclotron resonant scattering features (CRSFs) mainly in the X-ray band and Doppler-shifted stellar lines in the optical band (the dynamical method).

Currently, X-ray instruments (such as *XMM-Newton*, *NuSTAR* etc.) provide sufficient statistics for only around 20 ULXs to be analysed for winds through individual lines in grating spectra (Kosec et al. 2021), and for only about 30 sources to detect pulsations (Rodríguez Castillo et al. 2020) with sufficient statistical significance. Indeed, observations with the grating spectrometers need to be longer than approximately 100 ks to detect spectral lines significantly. Detecting CRSFs is also challenging as it requires high sensitivity across a broad energy band, which is achievable only for a limited number of sources. Consequently, the statistical sample size is insufficient to explore potential sub-samples of ULXs with differing characteristics (in order to unveil observables necessary to distinguish BHs from NSs), although new deep observations could address this limitation.

A possible method to investigate the accretion disc, the wind launching region and the nature of the accretor in ULXs is through timing analyses, including energy-dependent lags and wind response to continuum variability (Middleton et al. 2021). Unfortunately, we do not have the necessary spectral resolution and sensitivity to perform such studies on ULX time series.

Another limitation is the insufficient sensitivity and spectral resolution in the Fe K band (6–10 keV), which restricts the ability to detect the hottest components of the wind launched from the inner disc. At present, the only robust detections of Fe K absorption lines are found in a few sources (e.g. NGC 1313 X-1 and NGC 4045, see Walton et al. 2016, Brightman et al. 2022, respectively).

The astrophysics of ULXs have witnessed significant advancements through the use of novel techniques in X-ray timing and spectroscopy, coupled with theoretical simulations (e.g., Bachetti et al. 2014, Pinto et al. 2016, Mushtukov et al. 2019). This

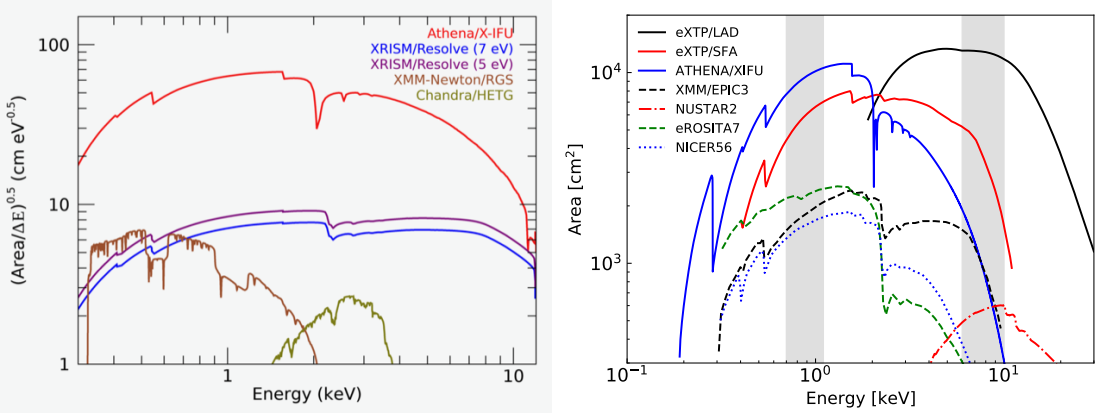

Figure 6.3: *Left panel:* Comparison of the square root of the ratio between the effective area and the energy resolution for selected future X-ray observatories (Credit: Guainazzi & Tashiro 2018). *Right panel:* Comparison of the effective area for selected future X-ray observatories.

will be improved by future missions.

There are several future X-ray missions currently being built or planned that will revolutionise this field in the next years (e.g. *Athena, eXTP, XRISM, HEX-P, etc.)*. Some of these projects could provide data with unprecedented statistics thanks to a larger collecting area and increased spectral resolution. These instruments will improve our knowledge of the spectral continuum, necessary to search for narrow and broad spectral features, which provided evidence for winds. In addition, some will be ideal instruments to search for pulsations and to perform timing analysis.

Among the most relevant telescopes related to the science of ULXs, there is *Advanced Telescope for High-ENergy Astrophysics (Athena)*[1], which is currently under ESA study and planned for launch after ~ 2035. *Athena*, with its two on-board instruments (X-IFU and WFI[2]), represents a significant improvement in effective area (see Fig. 6.3), and it will provide an enhancement, not only in the broadband analysis but also for high-resolution X-ray spectroscopic and will allow considerably deeper searches for pulsations in ULXs.

This facility will place more constraints on the population of these systems, resolving

[1] https://www.the-athena-x-ray-observatory.eu/en

[2] *The X-ray Integral Field Unit (X-IFU)*, will deliver spatially resolved high-resolution X-ray spectroscopy over a limited field of view and the *Wide Field Imager (WFI)* will provide sensitive wide field imaging and spectroscopy and high count-rate capability

ULXs in crowded fields, observing more distant and fainter sources (increasing the sample of ULXs with detected atomic lines) and probing shorter variability timescales.

In the next decade, there will also be the *enhanced X-ray Timing and Polarimetry (eXTP)*, planned for launch in 2027, which will have a large effective area in the X-ray band (> 2 keV) allowing detailed studies of the ULX population (see Fig. 6.3), in particular by boosting the search for CRSFs, the Fe K wind component, pulsations and (for nearby sources) polarisation. Overall, *eXTP* is expected to significantly advance our understanding of ULXs and their evolution.

The *X-Ray Imaging and Spectroscopy Mission, (XRISM*, 2023-) will improve high-spectral resolution measurements in the 1-10 keV band thanks to a higher effective area compared with *XMM*/RGS and Chandra gratings, thereby boosting Fe K wind detections. *HEX-P* (2032-, should it be approved by NASA) will cover the wide 0.3–150 keV band, doubling the effective area above 10 keV and improving the measurements of ULX spectral shapes and pulsations detections.

A

Appendix to Chapter 4: spectral parameters

In this appendix, we plot all the results from the spectral analysis of the pulsating NGC 1313 X-2 from Chapter 4.

A.1 Table best-fit parameters

Table A.1 reports the results of the spectral fits with the DISKBB+DISKBB+CUTOFFPL model for all *XMM-Newton* observations of X-2.

Table A.1: Best fitting spectral parameters of NGC 1313 X-2 in different observations obtained with the absorbed DISKBB+DISKBB+CUTOFFPL model.

ObsID	N_H (10^{22} cm^{-2})	T_1 (keV)	$norm_1$	L_1 (*) (10^{39} erg/s)	T_2 (keV)	$norm_2$	L_2 (*) (10^{39} erg/s)	$norm_3$ (10^{-5})	χ^2/dof
0106860101	$0.286^{+0.06}_{-0.04}$	0.219 ± 0.03	30^{+57}_{-16}	$3.4^{+1.7}_{-1.0}$	$0.71^{+0.10}_{-0.08}$	$0.11^{+0.08}_{-0.05}$	$1.26^{+0.18}_{-0.17}$	4.0 ± 0.3	137.31/144
0150280101	$0.10^{+0.05}_{-0.03}$	$0.5^{+1.8}_{-0.5}$	$0.13^{+923}_{-0.13}$	$5.75^{+24.}_{-5.}$	$1.4^{+8}_{-1.3}$	$0.03^{+0.03}_{-0.01}$	$5.2^{+1.1}_{-1.}$	$1.0^{+6.0}_{-1.0}$	64.91/63
0150280301	0.19 ± 0.02	0.37 ± 0.05	$2.3^{+1.4}_{-0.9}$	$1.9^{+0.4}_{-0.3}$	$1.871^{+0.04}_{-0.16}$	$0.014^{+0.004}_{-0.002}$	$7.46^{+0.16}_{-1.}$	$0.02^{+3}_{-0.02}$	161.42/191
0150280401	$0.27^{+0.06}_{-0.05}$	$0.27^{+0.05}_{-0.04}$	15^{+33}_{-10}	$3.8^{+2.}_{-1.3}$	$1.5^{+0.3}_{-0.2}$	$0.027^{+0.017}_{-0.010}$	$6.3^{+1.8}_{-1.0}$	9^{+5}_{-7}	165.28/158
0150280501	$0.13^{+0.03}_{-0.02}$	$0.49^{+0.09}_{-0.2}$	$0.005^{+0.10}_{-0.003}$	$1.86^{+0.3}_{-0.8}$	$1.8^{+0.4}_{-1.0}$	$0.73^{+41}_{-0.35}$	$2.5^{+0.4}_{-1.}$	$0.01^{+6.0}_{-0.01}$	86.77/87
0150280601	$0.26^{+0.06}_{-0.05}$	$0.23^{+0.06}_{-0.04}$	21^{+48}_{-15}	$2.47^{+1.6}_{-0.8}$	$0.84^{+0.14}_{-0.09}$	$0.09^{+0.06}_{-0.04}$	$1.97^{+0.18}_{-0.2}$	$3.1^{+0.6}_{-0.7}$	151.03/122
0150281101	$0.32^{+0.09}_{-0.05}$	$0.2^{+0.03}_{-0.04}$	$0.05^{+0.05}_{-0.018}$	$5.^{+4.}_{-2.}$	$0.94^{+0.14}_{-0.15}$	50^{+166}_{-29}	1.6 ± 0.18	$3.0^{+0.9}_{-1.0}$	62.86/82
205230301	0.27 ± 0.03	$0.29^{+0.05}_{-0.03}$	$1.56^{+0.2}_{-0.14}$	$3.32^{+1.1}_{-0.7}$	$0.029^{+0.009}_{-0.008}$	11^{+12}_{-6}	$7.7^{+1.2}_{-0.8}$	7^{+3}_{-5}	212.25/210
0205230401	$0.31^{+0.08}_{-0.07}$	$0.20^{+0.05}_{-0.04}$	$0.09^{+0.17}_{-0.07}$	$3.7^{+4.}_{-1.6}$	$0.69^{+0.2}_{-0.12}$	55^{+158}_{-41}	1.0 ± 0.2	$3.5^{+0.5}_{-0.6}$	82.88/90
0205230501	$0.29^{+0.05}_{-0.04}$	0.22 ± 0.03	$0.07^{+0.06}_{-0.03}$	$3.3^{+1.6}_{-0.9}$	$0.8^{+0.12}_{-0.09}$	28^{+44}_{-15}	1.22 ± 0.14	3.2 ± 0.4	130.98/128
0205230601	0.26 ± 0.05	$0.25^{+0.06}_{-0.03}$	15^{+24}_{-11}	$2.8^{+1.6}_{-1.0}$	$1.51^{+0.2}_{-0.15}$	$0.026^{+0.010}_{-0.009}$	$6.1^{+1.1}_{-0.7}$	9^{+3}_{-4}	178.94/213
0301860101	0.25 ± 0.03	$0.30^{+0.06}_{-0.04}$	6^{+9}_{-4}	$2.3^{+0.8}_{-0.5}$	$1.45^{+0.19}_{-0.14}$	$0.03^{+0.012}_{-0.009}$	$6.3^{+0.9}_{-0.6}$	7^{+3}_{-4}	210.74/218
0405090101	$0.240^{+0.016}_{-0.015}$	$0.275^{+0.02}_{-0.019}$	9^{+5}_{-3}	$2.3^{+0.8}_{-0.5}$	$1.17^{+0.06}_{-0.05}$	0.051 ± 0.008	$4.31^{+0.14}_{-0.13}$	12.2 ± 0.7	350.97/300
0693850501	$0.235^{+0.015}_{-0.014}$	$0.290^{+0.02}_{-0.019}$	$0.046^{+0.006}_{-0.005}$	$2.1^{+0.3}_{-0.2}$	1.24 ± 0.04	6^{+3}_{-2}	$4.85^{+0.11}_{-0.10}$	$2.4^{+0.5}_{-0.6}$	297.79/284
0693851201	0.218 ± 0.013	0.31 ± 0.02	$0.046^{+0.009}_{-0.008}$	$1.66^{+0.16}_{-0.13}$	$1.01^{+0.05}_{-0.04}$	$4.3^{+1.7}_{-1.2}$	2.1 ± 0.06	$0.5^{+0.2}_{-0.3}$	265.81/235
0722650101	$0.19^{+0.05}_{-0.03}$	$0.31^{+0.05}_{-0.08}$	$3.0^{+13}_{-1.5}$	$1.25^{+0.3}_{-2e+12}$	$1.0^{+5}_{-0.4}$	$0.005^{+2}_{-0.005}$	$0.17^{+1.3}_{-2e+12}$	$4.2^{+0.5}_{-4.2}$	63.42/72
0742590301	$0.28^{+0.03}_{-0.02}$	0.3 ± 0.02	$0.055^{+0.010}_{-0.009}$	$2.6^{+0.6}_{-0.4}$	1.13 ± 0.05	15^{+10}_{-6}	4.01 ± 0.12	2.5 ± 0.6	281.44/231
0742490101	0.25 ± 0.03	$0.3^{+0.04}_{-0.03}$	5^{+5}_{-3}	$1.2^{+0.3}_{-0.2}$	$1.04^{+0.08}_{-0.06}$	$0.032^{+0.009}_{-0.008}$	1.67 ± 0.06	0.8 ± 0.3	226.31/197
0764770101	$0.214^{+0.018}_{-0.017}$	$0.272^{+0.02}_{-0.018}$	7^{+3}_{-2}	$1.59^{+0.19}_{-0.14}$	$1.07^{+0.3}_{-0.16}$	$0.009^{+0.009}_{-0.005}$	$0.55^{+0.07}_{-0.05}$	$3.2^{+0.3}_{-0.4}$	173.59/227
0764770401	$0.24^{+0.05}_{-0.04}$	$0.24^{+0.05}_{-0.04}$	12^{+23}_{-7}	$1.8^{+0.9}_{-0.5}$	$0.85^{+0.06}_{-0.05}$	0.11 ± 0.03	$2.46^{+0.13}_{-0.15}$	1.7 ± 0.4	178.34/167
0782310101	$0.235^{+0.013}_{-0.012}$	$0.292^{+0.018}_{-0.016}$	$0.032^{+0.006}_{-0.005}$	$2.5^{+0.3}_{-0.2}$	1.26 ± 0.06	7^{+3}_{-2}	$3.61^{+0.14}_{-0.12}$	$7.3^{+0.6}_{-0.7}$	339.58/290
0794580601	$0.25^{+0.05}_{-0.04}$	0.25 ± 0.03	$0.08^{+0.03}_{-0.02}$	$2.5^{+0.9}_{-0.6}$	0.92 ± 0.07	15^{+21}_{-8}	$2.55^{+0.13}_{-0.14}$	5.0 ± 0.6	193.82/187
0803990101	$0.216^{+0.014}_{-0.013}$	0.33 ± 0.03	$2.5^{+1.3}_{-0.8}$	$11.34^{+0.15}_{-0.12}$	$1.17^{+0.06}_{-0.05}$	$0.035^{+0.007}_{-0.006}$	2.92 ± 0.08	$1.3^{+0.4}_{-0.5}$	229.80/249
0803990201	$0.281^{+0.019}_{-0.018}$	$0.254^{+0.019}_{-0.016}$	0.053 ± 0.007	$2.5^{+0.4}_{-0.3}$	1.13 ± 0.04	14^{+7}_{-5}	3.90 ± 0.09	$2.8^{+0.4}_{-0.5}$	314.91/259
0803990301	$0.225^{+0.03}_{-0.014}$	$0.28^{+0.05}_{-0.04}$	7^{+9}_{-4}	$1.9^{+0.6}_{-0.3}$	$0.80^{+0.13}_{-0.09}$	$0.07^{+0.06}_{-0.04}$	$1.33^{+0.19}_{-0.19}$	3.4 ± 0.3	229.31/182
0803990401	$0.27^{+0.05}_{-0.04}$	$0.24^{+0.04}_{-0.03}$	$0.056^{+0.03}_{-0.019}$	$1.2^{+0.6}_{-0.3}$	$0.8^{+0.07}_{-0.06}$	7^{+11}_{-4}	$0.93^{+0.08}_{-0.08}$	2.3 ± 0.2	152.54/175
0803990701	$0.20^{+0.04}_{-0.03}$	$0.35^{+0.05}_{-0.07}$	$0.004^{+0.008}_{-0.001}$	$2.0^{+0.4}_{-0.3}$	1.7 ± 0.9	$3.0^{+6}_{-1.3}$	$1.1^{+0.6}_{-0.5}$	$1.5^{+3}_{-1.5}$	95.17/70
0803990501	$0.27^{+0.03}_{-0.04}$	$0.25^{+0.03}_{-0.02}$	10^{+8}_{-5}	$1.7^{+0.5}_{-0.3}$	$0.93^{+0.08}_{-0.06}$	0.045 ± 0.013	1.53 ± 0.07	$0.9^{+0.3}_{-0.4}$	180.76/184
0803990601	$0.210^{+0.02}_{-0.018}$	0.31^{+} 0.03	$3.18^{+3}_{-1.2}$	$1.25^{+0.19}_{-0.14}$	$1.03^{+0.09}_{-0.08}$	$0.035^{+0.013}_{-0.010}$	$1.75^{+0.07}_{-0.08}$	0.7 ± 0.4	215.32/200

[1] *Notes*: Parameter uncertainties were estimated at 68%. (*) Luminosity values (in units of 10^{39} erg/s) are quoted for the unabsorbed model integrated over 0.3—10 keV.

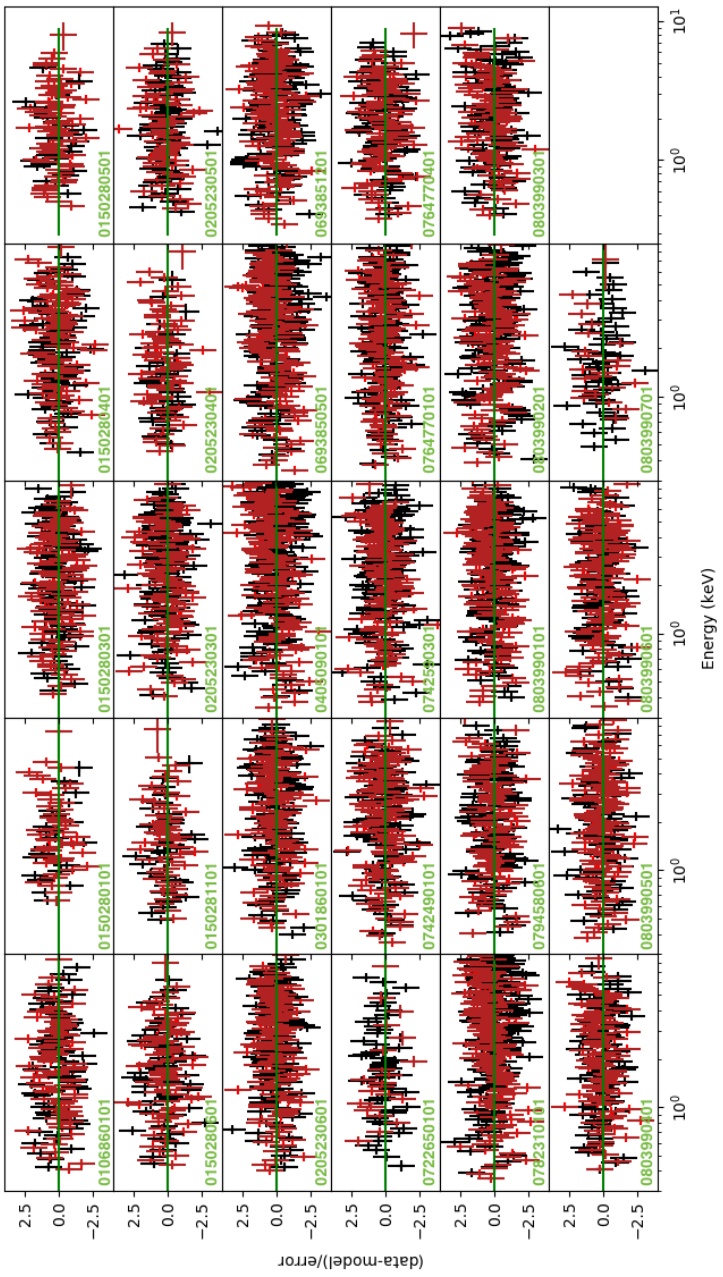

Figure A.1: Spectral residuals for the 29 spectra extracted from NGC 1313 X-2, calculated with respect to the DISKBB+DISKBB+CUTOFFPL model. Black and red points show data from the *XMM-Newton* EPIC-pn and EPIC-MOS detectors, respectively.

A.2 Table DISKBB+DISKBB parameters

Table A.2 reports the results of the spectral fits with the DISKBB+DISKBB model for all *XMM-Newton* observations of X-2. Fig. A.2 shows the associated residuals for the best-fit model.

Table A.2: Best fitting spectral parameters of NGC 1313 X-2 in different observations obtained with the absorbed DISKBB+DISKBB model.

ObsID	N_H (10^{22} cm^{-2})	T_1 (keV)	$norm_1$	T_2 (keV)	$norm_2$	χ^2/dof
0106860101	$0.199^{+0.018}_{-0.016}$	$0.34^{+0.02}_{-0.02}$	$3.2^{+1.4}_{-0.9}$	$1.82^{+0.17}_{-0.14}$	$0.0031^{+0.0012}_{-0.0009}$	149.14/145
0150280101	$0.089^{+0.2}_{-0.03}$	$0.7^{+6}_{-0.8}$	$0.05^{+101}_{-0.05}$	$1.5^{+1.5}_{-0.2}$	$0.023^{+0.018}_{-0.02}$	64.92/64
0150280301	0.19 ± 0.02	0.371 ± 0.05	$2.3^{+2}_{-1.1}$	$1.87^{+0.08}_{-0.07}$	0.014 ± 0.002	161.42/192
0150280401	0.24 ± 0.04	$0.3^{+0.06}_{-0.04}$	8^{+11}_{-5}	$1.90^{+0.10}_{-0.09}$	0.016 ± 0.003	166.83/159
0150280501	0.50 ± 0.09	$0.7^{+0.8}_{-0.3}$	$1.9^{+0.4}_{-0.3}$	$0.13^{+0.03}_{-0.02}$	$0.005^{+0.004}_{-0.003}$	86.77/88
0150280601	$0.19^{+0.03}_{-0.02}$	0.363 ± 0.05	$2.4^{+2}_{-1.1}$	$1.42^{+0.15}_{-0.12}$	$0.012^{+0.006}_{-0.004}$	157.38/123
0150281101	0.29 ± 0.06	$0.23^{+0.04}_{-0.03}$	26^{+43}_{-16}	$1.27^{+0.12}_{-0.10}$	$0.017^{+0.007}_{-0.006}$	66.69/83
0205230301	$0.25^{+0.03}_{-0.02}$	$0.33^{+0.04}_{-0.03}$	6^{+5}_{-3}	$1.82^{+0.06}_{-0.05}$	$0.020^{+0.003}_{-0.002}$	213.96/211
0205230401	$0.20^{+0.04}_{-0.03}$	$0.30^{+0.04}_{-0.03}$	5^{+5}_{-3}	$1.8^{+0.3}_{-0.2}$	$0.0028^{+0.0018}_{-0.0012}$	88.09/91
0205230501	0.213 ± 0.02	0.32 ± 0.03	$4.4^{+3}_{-1.6}$	$1.67^{+0.16}_{-0.13}$	$0.0045^{+0.0018}_{-0.0014}$	142.92/129
0205230601	$0.21^{+0.04}_{-0.03}$	$0.33^{+0.07}_{-0.05}$	4^{+5}_{-2}	$1.94^{+0.08}_{-0.07}$	0.014± 0.002	181.97/214
0301860101	0.225 ± 0.02	$0.36^{+0.05}_{-0.04}$	$2.7^{+2}_{-1.3}$	1.77 ±0.06	0.019 ± 0.003	213.29/219
0405090101	$0.182^{+0.008}_{-0.007}$	0.47 ± 0.03	$0.9^{+0.3}_{-0.2}$	2.03 ± 0.06	$0.0095^{+0.0012}_{-0.0011}$	411.82/301
0693850501	0.213 ± 0.010	0.35 ± 0.02	$2.8^{+1.0}_{-0.7}$	1.41 ± 0.02	0.030 ± 0.002	310.06/285 [2]
0693851201	$0.208^{+0.011}_{-0.010}$	$0.331^{+0.019}_{-0.017}$	$3.0^{+0.9}_{-0.7}$	$1.10^{+0.03}_{-0.02}$	0.033± 0.004	269.55/236
0722650101	0.175 ± 0.03	$0.333^{+0.04}_{-0.03}$	$2.3^{+1.7}_{-1.0}$	$3.1^{+1.0}_{-0.6}$	$0.0004^{+0.0004}_{-0.0002}$	63.79/73
0742590301	$0.245^{+0.018}_{-0.017}$	$0.31^{+0.03}_{-0.02}$	$5.5^{+3}_{-1.9}$	1.33 ± 0.03	$0.0316^{+0.0033}_{-0.0032}$	292.76/232
0742490101	$0.218^{+0.02}_{-0.018}$	0.33 ± 0.03	$2.1^{+1.4}_{-0.8}$	1.21 ± 0.04	0.018 ± 0.003	230.70/198
0764770101	0.186± 0.011	0.316± 0.012	$3.2^{+0.7}_{-0.6}$	$2.30^{+0.11}_{-0.10}$	0.0012± 0.0002	182.24/228
0764770401	$0.167^{+0.02}_{-0.017}$	0.44 ± 0.07	$0.9^{+0.8}_{-0.4}$	$1.23^{+0.14}_{-0.09}$	$0.020^{+0.011}_{-0.009}$	186.74/168
0782310101	0.201± 0.008	$0.380^{+0.018}_{-0.017}$	$2.3^{+0.6}_{-0.4}$	1.85 ± 0.04	$0.0103^{+0.0009}_{-0.0008}$	380.93/291
0794580601	$0.175^{+0.018}_{-0.016}$	$0.41^{+0.05}_{-0.04}$	$1.6^{+1.0}_{-0.6}$	$1.62^{+0.12}_{-0.10}$	0.010 ±0.003	213.02/188
0803990101	$0.204^{+0.011}_{-0.010}$	0.38 ± 0.03	$1.5^{+0.6}_{-0.4}$	1.32 ± 0.03	$0.023^{+0.003}_{-0.002}$	235.32/250
0803990201	$0.242^{+0.014}_{-0.013}$	$0.319^{+0.02}_{-0.019}$	$4.2^{+1.7}_{-1.2}$	$1.36^{+0.03}_{-0.02}$	0.028 ± 0.002	336.86/260
0803990301	$0.176^{+0.013}_{-0.012}$	$0.40^{+0.03}_{-0.02}$	$1.6^{+0.5}_{-0.4}$	$1.84^{+0.17}_{-0.14}$	$0.0031^{+0.0012}_{-0.0009}$	242.51/183
0803990401	$0.177^{+0.016}_{-0.014}$	0.46 ± 0.04	$0.46^{+0.2}_{-0.14}$	$2.0^{+0.3}_{-0.2}$	$0.0014^{+0.0009}_{-0.0006}$	173.38/176
0803990701	0.19 ± 0.03	0.359 ± 0.04	$2.7^{+2}_{-1.1}$	$2.0^{+0.3}_{-0.2}$	$0.0024^{+0.0017}_{-0.0011}$	95.21/71
0803990501	0.23 ± 0.02	0.29 ± 0.03	$4.1^{+3}_{-1.6}$	1.11 ± 0.04	0.0230 ± 0.004	185.33/185
0803990601	$0.198^{+0.016}_{-0.015}$	0.34 ± 0.03	$2.1^{+1.1}_{-0.7}$	$1.15^{+0.05}_{-0.04}$	0.023 ± 0.004	217.35/201

[2]*Notes*: Parameter uncertainties were estimated at 68%.

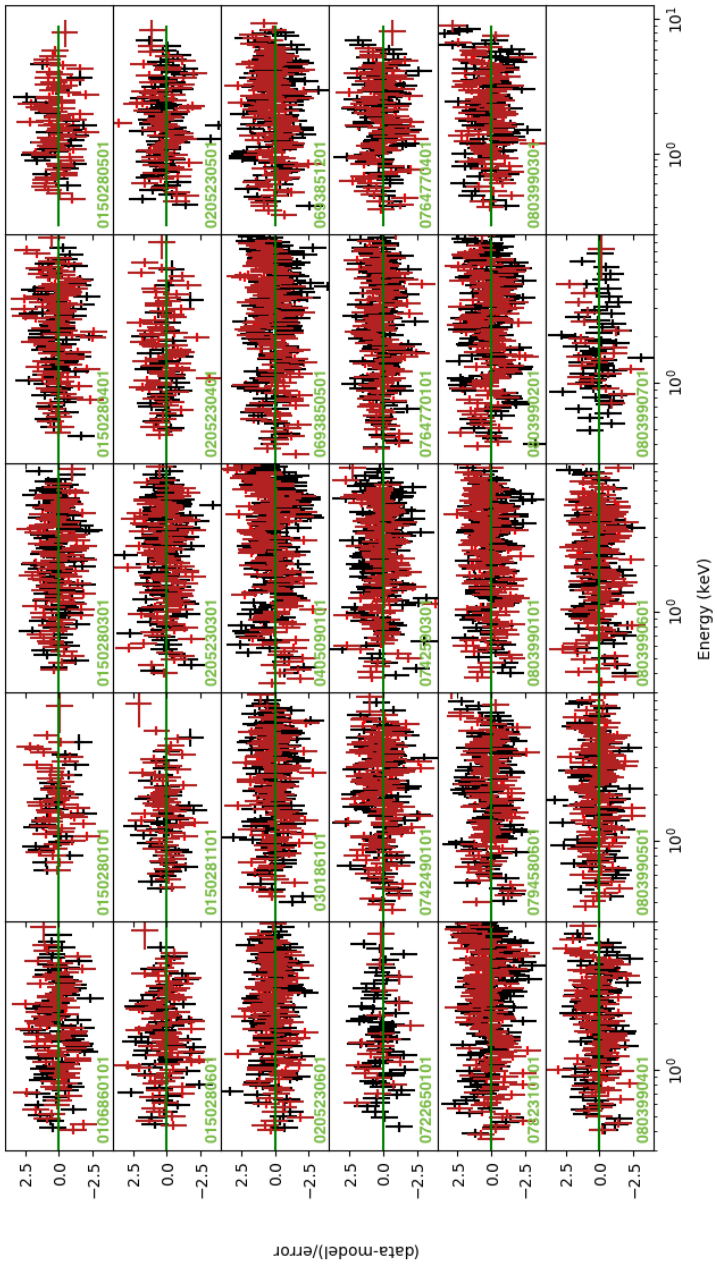

Figure A.2: Spectral residuals for the 29 spectra extracted from NGC 1313 X-2, calculated with respect to the DISKBB+DISKBB model. Black and red points show data from the *XMM-Newton* EPIC-pn and EPIC-MOS detectors, respectively.

A.3 Table of fractional variability, F_{var}

Table A.3: Fractional variability (%) measured using 40 ks EPIC-pn segments of light curve for each observation, which is a common time baseline for comparing the RMS estimated.

Obs.ID	1st segment (40ks)	2nd segment (40/80ks)	3rd segment (80/120ks)
0106860101	-	-	-
0150280101	-	-	-
0150280301	-	-	-
0150280401	-	-	-
0150280501	-	-	-
0150280601	-	-	-
0150281101	-	-	-
0205230301	-	-	-
0205230401	-	-	-
0205230501	-	-	-
0205230601	-	-	-
0301860101	-	-	-
0405090101	10.98 ± 0.02	7.191 ± 0.012	-
0693850501	18.22 ± 0.04	17.05 ± 0.05	-
0693851201	2.245 ± 0.008	-	-
0722650101	-	-	-
0742590301	23.79 ± 0.07	-	-
0742490101	4.16 ± 0.04	5.616 ± 0.011	-
0764770101	3.463 ± 0.002	-	-
0764770401	-	-	-
0782310101	11.98 ± 0.04	24.53 ± 0.07	-
0794580601	-	-	-
0803990101	15.90 ± 0.02	9.333 ± 0.009	19.73 ± 0.03
0803990201	4.907 ± 0.003	21.97 ± 0.09	11.92 ± 0.02
0803990301	3.12 ± 0.04	-	-
0803990401	5.743 ± 0.004	-	-
0803990701	-	-	-
0803990501	18.87 ± 0.04	3.82 ± 0.15	-
0803990601	14.36 ± 0.10	-	-

A.4 Table DISKBB+DISKBB parameters with fixed N_H

Table A.4 reports the results of the spectral fits with the DISKBB+DISKBB model with fixed N_H ($N_H = (0.194\times10^{22})$ cm^{-2}) for all *XMM-Newton* observations of X-2.

Table A.4: Best fitting spectral parameters of NGC 1313 X-2 in different observations obtained with the absorbed DISKBB+DISKBB model with fixed N_H.

ObsID	N_H (10^{22} cm^{-2})	T_1 (keV)	norm$_1$	T_2 (keV)	norm$_2$	χ^2/dof
0106860101	0.194	0.348 ± 0.011	$2.9^{+0.4}_{-0.3}$	$1.85^{+0.14}_{-0.12}$	$0.0029^{+0.0009}_{-0.0007}$	149.22/146
0150280101	0.194	$0.22^{+0.06}_{-0.04}$	14^{+25}_{-9}	$1.38^{+0.09}_{-0.08}$	$0.037^{+0.005}_{-0.009}$	65.24/65
0150280301	0.194	$0.34^{+0.03}_{-0.02}$	$2.4^{+0.7}_{-0.5}$	$1.87^{+0.07}_{-0.06}$	$0.0141^{+0.0020}_{-0.0019}$	161.42/193
0150280401	0.194	$0.37^{+0.04}_{-0.03}$	$2.4^{+0.9}_{-0.7}$	$1.96^{+0.10}_{-0.09}$	0.014 ± 0.003	168.43/160
0150280501	0.194	0.35 ± 0.03	$3.5^{+1.5}_{-1.0}$	$1.53^{+0.18}_{-0.14}$	$0.0121^{+0.006}_{-0.005}$	90.97/89
0150280601	0.194	0.351 ± 0.02	$2.8^{+0.7}_{-0.5}$	$1.39^{+0.11}_{-0.09}$	0.0126 ± 0.004	157.44/124
0150281101	0.194	0.30 ± 0.02	$4.9^{+1.6}_{-1.2}$	$1.39^{+0.14}_{-0.11}$	$0.011^{+0.005}_{-0.004}$	69.78/84
0205230301	0.194	0.42 ± 0.03	$1.4^{+0.4}_{-0.3}$	1.89 ± 0.06	0.016 ± 0.002	220.15/212
0205230401	0.194	$0.305^{+0.016}_{-0.015}$	$4.6^{+1.1}_{-0.9}$	$1.86^{+0.2}_{-0.19}$	$0.0027^{+0.0014}_{-0.0010}$	88.11/92
0205230501	0.194	$0.341^{+0.013}_{-0.012}$	$3.1^{+0.5}_{-0.4}$	$1.75^{+0.14}_{-0.12}$	$0.0037^{+0.0013}_{-0.0010}$	143.70/130
0205230601	0.194	0.365 ± 0.03	$2.0^{+0.6}_{-0.5}$	$1.97^{+0.07}_{-0.06}$	$0.0131^{+0.0017}_{-0.0016}$	182.19/215
0301860101	0.194	0.44 ± 0.03	$1.0^{+0.3}_{-0.2}$	1.82 ± 0.06	0.016 ± 0.002	216.03/220
0405090101	0.194	0.432± 0.012	$1.38^{+0.12}_{-0.13}$	1.981 ± 0.04	0.0106± 0.0008	414.11/302
0693850501	0.194	0.386± 0.011	$1.60^{+0.16}_{-0.15}$	$1.434^{+0.019}_{-0.018}$	0.0273± 0.0016	314.18/286 [3]
0693851201	0.194	0.354± 0.009	$2.15^{+0.2}_{-0.18}$	1.12 ± 0.02	0.030 ± 0.003	271.48/237
0722650101	0.194	$0.315^{+0.016}_{-0.015}$	$3.1^{+0.7}_{-0.6}$	$2.9^{+0.7}_{-0.4}$	$0.0005^{+0.0004}_{-0.0003}$	64.17/74
0742590301	0.194	$0.398^{+0.017}_{-0.016}$	$1.42^{+0.2}_{-0.18}$	1.39 ± 0.03	0.025 ± 0.003	303.95/233
0742490101	0.194	$0.368^{+0.017}_{-0.016}$	$1.12^{+0.19}_{-0.16}$	1.238 ± 0.04	0.016 ± 0.002	232.48/199
0764770101	0.194	0.308± 0.005	3.7 ± 0.3	2.27 ± 0.09	0.0012± 0.0002	182.73/229
0764770401	0.194	0.36± 0.02	$2.1^{+0.5}_{-0.4}$	$1.14^{+0.06}_{-0.05}$	$0.030^{+0.007}_{-0.006}$	188.30/169
0782310101	0.194	$0.393^{+0.009}_{-0.008}$	$1.95^{+0.16}_{-0.14}$	1.870 ± 0.03	0.0099± 0.0007	381.64/292
0794580601	0.194	0.368± 0.016	2.5 ± 0.4	$1.55^{+0.07}_{-0.06}$	$0.013^{+0.003}_{-0.002}$	214.05/189
0803990101	0.194	0.398± 0.014	$1.14^{+0.14}_{-0.12}$	1.335 ± 0.03	0.021 ± 0.002	236.22/251
0803990201	0.194	$0.414^{+0.015}_{-0.014}$	$1.13^{+0.13}_{-0.11}$	1.43 ± 0.03	$0.0220^{+0.0019}_{-0.0018}$	354.12/261
0803990301	0.194	0.370± 0.011	$2.3^{+0.3}_{-0.2}$	$1.73^{+0.11}_{-0.10}$	$0.0041^{+0.0011}_{-0.0009}$	244.50/184
0803990401	0.194	0.370± 0.011	0.422± 0.018	$0.69^{+0.11}_{-0.09}$	$1.85^{+0.16}_{-0.13}$	174.49/177
0803990701	0.194	$0.357^{+0.019}_{-0.018}$	$2.8^{+0.6}_{-0.5}$	$2.0^{+0.3}_{-0.2}$	$0.0025^{+0.0014}_{-0.0010}$	95.22/72
0803990501	0.194	$0.344^{+0.015}_{-0.014}$	$1.8^{+0.3}_{-0.2}$	1.16 ± 0.04	0.018 ± 0.003	188.71/186
0803990601	0.194	0.346± 0.014	$1.9^{+0.3}_{-0.2}$	$1.16^{+0.04}_{-0.03}$	0.022 ± 0.003	217.43/202

[3] *Notes*: Parameter uncertainties were estimated at 68%.

B

Appendix to Chapter 5: validation of the timing code through the confirmed case of NGC 5408 X-1

In this appendix, we show several tests of the STINGRAY code applied to the ULX NGC 5408 X-1 for which a time lag of the soft X-ray band was discovered by De Marco et al. (2013) using a different code.

In order to obtain the same results, I followed, as close as possible, the procedure described in their paper. I analysed the same observations (from 2006 to 2011) performed by *XMM-Newton* (see Table B.1). Unlike the article, where the exposures of pn+MOS1+MOS2 detectors were combined, for simplicity, I used only pn data.

As an example, I report only the results obtained for the first two observations, since in De Marco et al. 2013 the other observations were stacked.

Table B.1: *XMM-Newton* observations of NGC 5408 X-1.

Obs.ID [(1)]	Date [(2)]	$t_{\rm exp}$ (ks) [(3)] (pn)
0302900101	2006-01-13	130
0500750101	2008-01-13	114
0653380201	2010-07-17	127
0653380301	2010-07-19	129
0653380401	2011-01-26	119
0653380501	2011-01-28	124

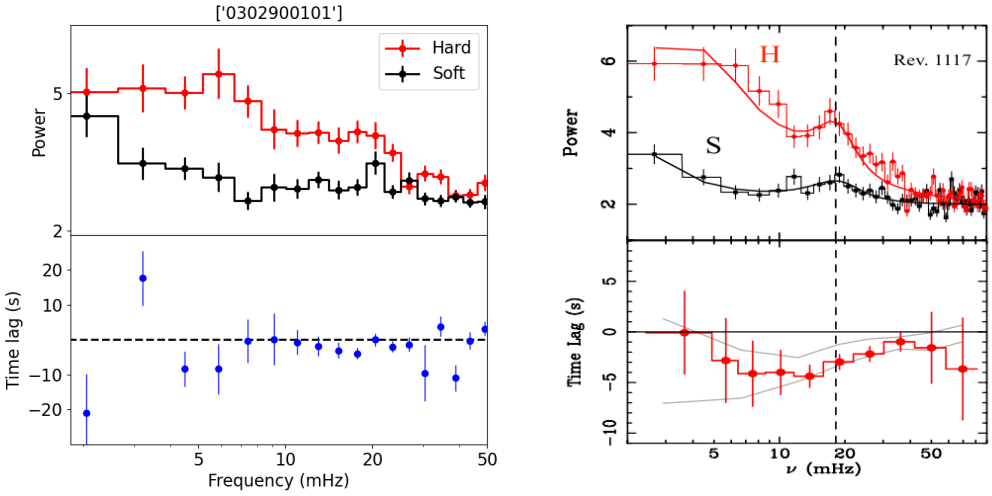

Figure B.1: Comparison between the results obtained in this thesis (left panel) and those obtained by De Marco et al. 2013 (right panel). *Upper panel*: PSD in the soft (0.3-1 keV, black) and hard (1-7 keV, red) bands. *Lower panel*: Time lag vs frequency spectra as computed between the soft and hard energy bands.

For each observation, I extracted light curves in the whole energy band (0.3–7 keV) and in two different bands (i.e. soft 0.3–1.0 keV and hard 1.0–7 keV), with a time resolution of 10s. Adopting the Leahy normalisation (Leahy et al. 1983), whereby the Poisson noise component has constant power $P_{noise} = 2$, I calculated the power spectrum for the entire light curve, divided it into smaller segments (with a size of 1000s) and calculated the power spectrum of each of them and averaged for all segments. The same procedure was also performed for hard (1.0–7 keV) and soft bands (0.3–1.0 keV). I plotted the results for ObsID 0302900101 and ObsID 0500750101 in Fig. B.1 and B.2 (left panels), respectively.

For each observation, I calculated the cross-spectrum between the soft and hard bands and the time lags as a function of frequency. I rebinned the cross-spectrum, adopting bins of length $dv_j = dv_{j-1}(1 + f)$, with f=0.1, which is slightly different from the one adopted in the paper. The results are reported in Fig. B.1 and B.2 (left panels).

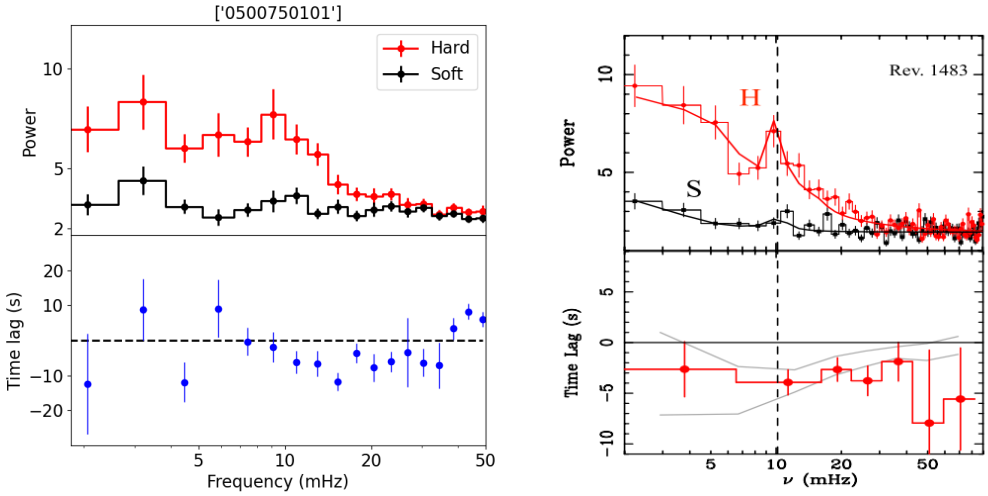

Figure B.2: Comparison between the results obtained in this thesis (left panel) and those obtained by De Marco et al. 2013 (right panel). *Upper panel*: PSD in the soft (0.3-1 keV, black) and hard (1-7 keV, red) bands. *Lower panel*: Time lag vs frequency spectra as computed between the soft and hard energy bands.

As shown, I found a soft delay of the order $\lesssim 10$ s in the frequency range 8–30 mHz in both observations, which are comparable with the time lag around ~ 5 s, obtained by De Marco et al. 2013 (see Fig. B.1 and B.2, right panels).

C

List of acronyms

Acronym	Meaning
AGN	Active Galactic Nuclei
AMXP	Accreting Millisecond X-ray Pulsar
ASCA	Advanced Satellite for Cosmology and Astrophysics
Athena	Advanced Telescope for High-Energy Astrophysics
BH	Black Hole
BD	Broadened disc
CCD	Charged Coupled Device
CCF	Current Calibration file
C.O.	Compact Object
CRSF	Cyclotron resonant scattering feature
CS	Cross-spectrum
CV	Cataclysmic variable
EPIC	European Photon Imaging Camera
ERM	EPIC Radiation Monitor
ESA	European Space Agency
ESAC	European Space Astronomy Centre
eXTP	Enhanced X-ray Timing and Polarimetry
FITS	Flexible Image Transport System
FOV	Field of view
FWHM	Full Width Half Maximum

Galactic BHB (or BH XRB)	Galactic black hole binary
GTI	Good time intervals
HUL	Hard ultra-luminous
HEW	Half Energy Width
HEX-P	High Energy X-ray Probe
HMXB	High Mass X-ray Binary
HST	Hubble Space Telescope
IMBH	Intermediate mass black hole
LEDD	Eddington luminosity / Eddington limit
LMXB	Low Mass X-ray Binary
MOS	Metal Oxide Semiconductor
NS	Neutron Star
ODF	Observation Data Files
OM	Optical monitor
NuSTAR	Nuclear Spectroscopic Telescope Array
PI	Pulsa Invariant
PPS	Pipeline Processing System
PSD	Power Density Spectrum
PSF	Point Spread Function
PULX	Ultraluminous X-ray pulsar
QPO	Quasi-periodic oscillation
RGS	Reflection Grating Spectrometer
RLOF	Roche lobes overflow
ROSAT	Röntgen Satellite
SAS	Science Analysis System
SMBH	Supermassive Black Hole
S/N	Signal-to-noise
SNe	Supernovae
SOC	Science Operations Centre
SSC	Survey System Center
SSUL (or ULS)	Supersoft ultra-luminous
SUL	Soft ultra-luminous
UFO	Ultrafast Outflow

UL	Ultraluminous
ULX	Ultraluminous X-ray source
WD	White Dwarf
XMM-Newton	X-ray Multi Mirror - Newton
XRB	X-ray binary
XRISM	X-Ray Imaging and Spectroscopy Mission
XSA	XMM-Newton Science Archive

Bibliography

Abbott, B. P., Abbott, R., Abbott, T. D., et al. 2016a, Phys. Rev. Lett., 116, 061102

Abbott, B. P., Abbott, R., Abbott, T. D., et al. 2016b, Phys. Rev. X, 6, 041015

Abbott, B. P., Abbott, R., Abbott, T. D., et al. 2019, Physical Review X, 9, 031040

Abramowicz, M. A., Czerny, B., Lasota, J. P., & Szuszkiewicz, E. 1988, The Astrophysical Journal, 332, 646

Alston, W. N., Pinto, C., Barret, D., et al. 2021, Monthly Notices of the Royal Astronomical Society, 505, 3722

Arévalo, P. & Uttley, P. 2006, Monthly Notices of the Royal Astronomical Society, 367, 801

Arnaud, K. A. 1996, in Astronomical Society of the Pacific Conference Series, Vol. 101, Astronomical Data Analysis Software and Systems V, ed. G. H. Jacoby & J. Barnes, 17

Bachetti, M., Harrison, F. A., Walton, D. J., et al. 2014, Nature, 514, 202

Bachetti, M., Heida, M., Maccarone, T., et al. 2022, The Astrophysical Journal, 937, 125

Bachetti, M., Rana, V., Walton, D. J., et al. 2013, The Astrophysical Journal, 778, 163

Barra, F., Pinto, C., Walton, D. J., et al. 2022, Monthly Notices of the Royal Astronomical Society, 516, 3972

Bhattacharya, D. & van den Heuvel, E. P. J. 1991, Physics Reports, 203, 1

Brightman, M., Harrison, F., Walton, D. J., et al. 2016, The Astrophysical Journal, 816, 60

Brightman, M., Kosec, P., Fürst, F., et al. 2022, The Astrophysical Journal, 929, 138

Brinkman, A., Aarts, H., den Boggende, A., et al. 1998, in Science with XMM, 2

Cackett, E. M., Chiang, C.-Y., McHardy, I., et al. 2018, The Astrophysical Journal, 857, 53

Carpano, S., Haberl, F., Maitra, C., & Vasilopoulos, G. 2018, Monthly Notices of the Royal Astronomical Society, 476, L45

Colbert, E. J. M. & Mushotzky, R. F. 1999, The Astrophysical Journal, 519, 89

Colbert, E. J. M. & Ptak, A. F. 2002, VizieR Online Data Catalog, 214

Collin, S. & Kawaguchi, T. 2004, Astronomy and Astrophysics, 426, 797

Cseh, D., Kaaret, P., Corbel, S., et al. 2014, Monthly Notices of the Royal Astronomical Society, 439, L1

De Marco, B., Motta, S. E., & Belloni, T. M. 2022, in Handbook of X-ray and Gamma-ray Astrophysics. Edited by Cosimo Bambi and Andrea Santangelo, 58

De Marco, B. & Ponti, G. 2019, Astronomische Nachrichten, 340, 290

De Marco, B., Ponti, G., Miniutti, G., et al. 2013, Monthly Notices of the Royal Astronomical Society, 436, 3782

Del Santo, M., Malzac, J., Jourdain, E., Belloni, T., & Ubertini, P. 2008, Monthly Notices of the Royal Astronomical Society, 390, 227

den Herder, J. W., Brinkman, A. C., Kahn, S. M., et al. 2001, Astronomy and Astrophysics, 365, L7

Done, C., Gierliński, M., & Kubota, A. 2007, Astronomy and Astrophysics Review, 15, 1

Earnshaw, H. P., Heida, M., Brightman, M., et al. 2020, The Astrophysical Journal, 891, 153

Earnshaw, H. P., Roberts, T. P., Middleton, M. J., Walton, D. J., & Mateos, S. 2019, Monthly Notices of the Royal Astronomical Society, 483, 5554

Evans, P. A., Beardmore, A. P., Page, K. L., et al. 2007, Astronomy and Astrophysics, 469, 379

Fabian, A. C. & Ross, R. R. 2010, Space Science Reviews, 157, 167

Fabian, A. C., Zoghbi, A., Ross, R. R., et al. 2009, Nature, 459, 540

Fabrika, S., Ueda, Y., Vinokurov, A., Sholukhova, O., & Shidatsu, M. 2015, Nature Physics, 11, 551

Farrell, S. A., Webb, N. A., Barret, D., Godet, O., & Rodrigues, J. M. 2009, Nature, 460, 73

Fiacconi, D., Pinto, C., Walton, D. J., & Fabian, A. C. 2017, Monthly Notices of the Royal Astronomical Society, 469, L99

Frank, J., King, A., & Raine, D. J. 2002, Accretion Power in Astrophysics: Third Edition

Fürst, F., Walton, D. J., Harrison, F. A., et al. 2016, The Astrophysical Journal Letters, 831, L14

Fürst, F., Walton, D. J., Heida, M., et al. 2018, Astronomy and Astrophysics, 616, A186

Fürst, F., Walton, D. J., Israel, G. L., et al. 2023, Astronomy and Astrophysics, 672, A140

García, J. A., Dauser, T., Ludlam, R., et al. 2022, The Astrophysical Journal, 926, 13

Giacconi, R. 1974, in Gravitational Radiation and Gravitational Collapse, ed. C. Dewitt-Morette, Vol. 64, 147

Giacconi, R. 1981, Annals of the New York Academy of Sciences, 375, 210

Gladstone, J. C., Copperwheat, C., Heinke, C. O., et al. 2013, The Astrophysical Journal Supplement, 206, 14

Gladstone, J. C., Roberts, T. P., & Done, C. 2009, Monthly Notices of the Royal Astronomical Society, 397, 1836

Grimm, H. J., Gilfanov, M., & Sunyaev, R. 2002, Astronomy and Astrophysics, 391, 923

Guainazzi, M. & Tashiro, M. S. 2018, arXiv e-prints, arXiv:1807.06903

Gúrpide, A., Godet, O., Koliopanos, F., Webb, N., & Olive, J. F. 2021a, Astronomy and Astrophysics, 649, A104

Gúrpide, A., Godet, O., Koliopanos, F., Webb, N., & Olive, J.-F. 2021b, arXiv e-prints, arXiv:2102.11159

Hameury, J. M. & Lasota, J. P. 2020, Astronomy and Astrophysics, 643, A171

Heida, M., Lau, R. M., Davies, B., et al. 2019, The Astrophysical Journal Letters, 883, L34

Heil, L. M. & Vaughan, S. 2010, Monthly Notices of the Royal Astronomical Society, 405, L86

Heil, L. M., Vaughan, S., & Roberts, T. P. 2009, Monthly Notices of the Royal Astronomical Society, 397, 1061

Hernández-García, L., Vaughan, S., Roberts, T. P., & Middleton, M. 2015, Monthly Notices of the Royal Astronomical Society, 453, 2877

Hjellming, R. M. & Johnston, K. J. 1981, The Astrophysical Journal Letters, 246, L141

Hu, C.-P., Kong, A. K. H., Ng, C. Y., & Li, K. L. 2018, The Astrophysical Journal, 864, 64

Huang, J., Jiang, Y.-F., Feng, H., et al. 2023, The Astrophysical Journal, 945, 57

Huppenkothen, D., Bachetti, M., Stevens, A., et al. 2019, Journal of Open Source Software, 4, 1393

Huppenkothen, D., Bachetti, M., Stevens, A. L., et al. 2019, The Astrophysical Journal, 881, 39

Israel, G. L., Belfiore, A., Stella, L., et al. 2017a, Science, 355, 817

Israel, G. L., Esposito, P., Rodríguez Castillo, G. A., & Sidoli, L. 2016, Monthly Notices of the Royal Astronomical Society, 462, 4371

Israel, G. L., Papitto, A., Esposito, P., et al. 2017b, Monthly Notices of the Royal Astronomical Society, 466, L48

Jithesh, V. & Wang, Z. 2015, Monthly Notices of the Royal Astronomical Society, 448, 1973

Kaaret, P., Feng, H., & Roberts, T. P. 2017, Annual Review of Astronomy and Astrophysics, 55, 303

Kaaret, P., Ward, M. J., & Zezas, A. 2004, Monthly Notices of the Royal Astronomical Society, 351, L83

Kaastra, J. S., Mewe, R., & Nieuwenhuijzen, H. 1996, in UV and X-ray Spec. of Astr. and Lab. Plasmas, ed. K. Yamashita & T. Watanabe, 411–414

Kajava, J. J. E. & Poutanen, J. 2009, Monthly Notices of the Royal Astronomical Society, 398, 1450

Kara, E., Pinto, C., Walton, D. J., et al. 2020, Monthly Notices of the Royal Astronomical Society, 491, 5172

Kara, E., Steiner, J. F., Fabian, A. C., et al. 2019, Nature, 565, 198

King, A. & Lasota, J.-P. 2020, Monthly Notices of the Royal Astronomical Society, 494, 3611

King, A., Lasota, J.-P., & Kluźniak, W. 2017, Monthly Notices of the Royal Astronomical Society, 468, L59

King, A., Lasota, J.-P., & Middleton, M. 2023, New Astronomy Review, 96, 101672

King, A. R., Davies, M. B., Ward, M. J., Fabbiano, G., & Elvis, M. 2001, The Astrophysical Journal Letters, 552, L109

Koliopanos, F., Vasilopoulos, G., Godet, O., et al. 2017, Astronomy and Astrophysics, 608, A47

Koljonen, K. I. I., Maccarone, T., McCollough, M. L., et al. 2018, Astronomy and Astrophysics, 612, A27

Kosec, P., Pinto, C., Fabian, A. C., & Walton, D. J. 2018a, Monthly Notices of the Royal Astronomical Society, 473, 5680

Kosec, P., Pinto, C., Reynolds, C. S., et al. 2021, Monthly Notices of the Royal Astronomical Society, 508, 3569

Kosec, P., Pinto, C., Walton, D. J., et al. 2018b, Monthly Notices of the Royal Astronomical Society, 479, 3978

Kovlakas, K., Zezas, A., Andrews, J. J., et al. 2020, Monthly Notices of the Royal Astronomical Society, 498, 4790

Leahy, D. A., Darbro, W., Elsner, R. F., et al. 1983, The Astrophysical Journal, 266, 160

Liu, J.-F. & Bregman, J. N. 2005, VizieR Online Data Catalog, 215

Lomb, N. R. 1976, Astronomy and Astrophysics, Supplement, 39, 447

Luangtip, W., Roberts, T. P., & Done, C. 2016, Monthly Notices of the Royal Astronomical Society, 460, 4417

Lumb, D. H., Warwick, R. S., Page, M., & De Luca, A. 2002, Astronomy and Astrophysics, 389, 93

Marshall, H. L., Canizares, C. R., & Schulz, N. S. 2002, The Astrophysical Journal, 564, 941

Mason, K. O., Breeveld, A., Much, R., et al. 2001, Astronomy and Astrophysics, 365, L36

Mendez, B., Davis, M., Newman, J., et al. 2002, in American Astronomical Society Meeting Abstracts, Vol. 201, American Astronomical Society Meeting Abstracts, 23.06

Middleton, M. J., Heil, L., Pintore, F., Walton, D. J., & Roberts, T. P. 2015a, Monthly Notices of the Royal Astronomical Society, 447, 3243

Middleton, M. J. & King, A. 2016, Monthly Notices of the Royal Astronomical Society, 462, L71

Middleton, M. J., Miller-Jones, J. C. A., Markoff, S., et al. 2013, Nature, 493, 187

Middleton, M. J., Roberts, T. P., Done, C., & Jackson, F. E. 2011, Monthly Notices of the Royal Astronomical Society, 411, 644

Middleton, M. J., Walton, D. J., Alston, W., et al. 2021, Monthly Notices of the Royal Astronomical Society, 506, 1045

Middleton, M. J., Walton, D. J., Fabian, A., et al. 2015b, Monthly Notices of the Royal Astronomical Society, 454, 3134

Middleton, M. J., Walton, D. J., Roberts, T. P., & Heil, L. 2014, Monthly Notices of the Royal Astronomical Society, 438, L51

Miller, M. C. 2002, The Astrophysical Journal, 581, 438

Mineshige, S., Hirano, A., Kitamoto, S., Yamada, T. T., & Fukue, J. 1994, The Astrophysical Journal, 426, 308

Mondal, S., Różańska, A., De Marco, B., & Markowitz, A. 2021, Monthly Notices of the Royal Astronomical Society, 505, L106

Motta, S. E., Kajava, J. J. E., Giustini, M., et al. 2021, Monthly Notices of the Royal Astronomical Society, 503, 152

Mushtukov, A. A., Ingram, A., Middleton, M., Nagirner, D. I., & van der Klis, M. 2019, Monthly Notices of the Royal Astronomical Society, 484, 687

Nandra, K., George, I. M., Mushotzky, R. F., Turner, T. J., & Yaqoob, T. 1997, The Astrophysical Journal, 476, 70

Pakull, M. W. & Mirioni, L. 2002, arXiv e-prints, astro

Pakull, M. W. & Mirioni, L. 2003, in Revista Mexicana de Astronomia y Astrofisica Conference Series, Vol. 15, Revista Mexicana de Astronomia y Astrofisica Conference Series, ed. J. Arthur & W. J. Henney, 197–199

Pakull, M. W., Soria, R., & Motch, C. 2010, Nature, 466, 209

Pasham, D., Strohmayer, T., & Mushotzky, R. 2015, in APS Meeting Abstracts, Vol. 2015, APS April Meeting Abstracts, U2.002

Pinto, C., Alston, W., Soria, R., et al. 2017, Monthly Notices of the Royal Astronomical Society, 468, 2865

Pinto, C., Mehdipour, M., Walton, D. J., et al. 2020a, Monthly Notices of the Royal Astronomical Society, 491, 5702

Pinto, C., Middleton, M. J., & Fabian, A. C. 2016, Nature, 533, 64

Pinto, C. & Walton, D. J. 2023, arXiv e-prints, arXiv:2302.00006

Pinto, C., Walton, D. J., Kara, E., et al. 2020b, Monthly Notices of the Royal Astronomical Society, 492, 4646

Pintore, F., Esposito, P., Zampieri, L., Motta, S., & Wolter, A. 2015, Monthly Notices of the Royal Astronomical Society, 448, 1153

Pintore, F., Motta, S., Pinto, C., et al. 2021, Monthly Notices of the Royal Astronomical Society, 504, 551

Pintore, F. & Zampieri, L. 2012, Monthly Notices of the Royal Astronomical Society, 420, 1107

Pintore, F., Zampieri, L., Stella, L., et al. 2017, The Astrophysical Journal, 836, 113

Pintore, F., Zampieri, L., Wolter, A., & Belloni, T. 2014, Monthly Notices of the Royal Astronomical Society, 439, 3461

Portegies Zwart, S. F. & McMillan, S. L. W. 2002, The Astrophysical Journal, 576, 899

Poutanen, J., Lipunova, G., Fabrika, S., Butkevich, A. G., & Abolmasov, P. 2007, Monthly Notices of the Royal Astronomical Society, 377, 1187

Qing, G., Wang, W., Liu, J.-F., & Yoachim, P. 2015, The Astrophysical Journal, 799, 19

Qiu, Y. & Feng, H. 2021, The Astrophysical Journal, 906, 36

Remillard, R. A. & McClintock, J. E. 2006, Annual Review of Astronomy and Astrophysics, 44, 49

Robba, A., Pinto, C., Walton, D. J., et al. 2021, Astronomy and Astrophysics, 652, A118

Roberts, T. P. & Warwick, R. S. 2000, Monthly Notices of the Royal Astronomical Society, 315, 98

Rodríguez Castillo, G. A., Israel, G. L., Belfiore, A., et al. 2020, The Astrophysical Journal, 895, 60

Sathyaprakash, R., Roberts, T. P., Walton, D. J., et al. 2019, Monthly Notices of the Royal Astronomical Society, L104

Scargle, J. D. 1982, The Astrophysical Journal, 263, 835

Shakura, N. I. & Sunyaev, R. A. 1973, Astronomy and Astrophysics, 500, 33

Skinner, G. K., Bedford, D. K., Elsner, R. F., et al. 1982, Nature, 297, 568

Soria, R. 2007, Astrophysics and Space Science, 311, 213

Stobbart, A. M., Roberts, T. P., & Warwick, R. S. 2006, Monthly Notices of the Royal Astronomical Society, 370, 25

Strüder, L., Briel, U., Dennerl, K., et al. 2001, Astronomy and Astrophysics, 365, L18

Sutton, A. D., Roberts, T. P., & Middleton, M. J. 2013, Monthly Notices of the Royal Astronomical Society, 435, 1758

Swartz, D. A., Soria, R., Tennant, A. F., & Yukita, M. 2011, The Astrophysical Journal, 741, 49

Swartz, D. A., Tennant, A. F., & Soria, R. 2009, The Astrophysical Journal, 703, 159

Taniguchi, Y., Shioya, Y., Tsuru, T. G., & Ikeuchi, S. 2000, Publications of the Astronomical Society of Japan, 52, 533

Tao, L., Feng, H., Grisé, F., & Kaaret, P. 2011, The Astrophysical Journal, 737, 81

Tauris, T. M. & van den Heuvel, E. P. J. 2006, in Compact stellar X-ray sources, Vol. 39, 623–665

Thorne, K. S. 1974, The Astrophysical Journal, 191, 507

Truemper, J., Pietsch, W., Reppin, C., et al. 1978, The Astrophysical Journal Letters, 219, L105

Tully, R. B., Courtois, H. M., & Sorce, J. G. 2016, The Astronomical Journal, 152, 50

Turner, M. J. L., Abbey, A., Arnaud, M., et al. 2001, Astronomy and Astrophysics, 365, L27

Uttley, P., Cackett, E. M., Fabian, A. C., Kara, E., & Wilkins, D. R. 2014, Astronomy and Astrophysics Review, 22, 72

VanderPlas, J. T. 2018, The Astrophysical Journal Supplement, 236, 16

Vasilopoulos, G., Lander, S. K., Koliopanos, F., & Bailyn, C. D. 2020, Monthly Notices of the Royal Astronomical Society, 491, 4949

Vaughan, B. A. & Nowak, M. A. 1997, The Astrophysical Journal Letters, 474, L43

Vaughan, S., Edelson, R., Warwick, R. S., & Uttley, P. 2003, Monthly Notices of the Royal Astronomical Society, 345, 1271

Vierdayanti, K., Done, C., Roberts, T. P., & Mineshige, S. 2010, Monthly Notices of the Royal Astronomical Society, 403, 1206

Walton, D. J., Bachetti, M., Fürst, F., et al. 2018a, The Astrophysical Journal Letters, 857, L3

Walton, D. J., Fürst, F., Harrison, F. A., et al. 2017, The Astrophysical Journal, 839, 105

Walton, D. J., Fürst, F., Harrison, F. A., et al. 2018b, Monthly Notices of the Royal Astronomical Society, 473, 4360

Walton, D. J., Fürst, F., Heida, M., et al. 2018c, The Astrophysical Journal, 856, 128

Walton, D. J., Fürst, F., Heida, M., et al. 2018d, The Astrophysical Journal, 856, 128

Walton, D. J., Harrison, F. A., Grefenstette, B. W., et al. 2014, The Astrophysical Journal, 793, 21

Walton, D. J., MacKenzie, A. D., Gully, H., et al. 2022, VizieR Online Data Catalog, J/MNRAS/509/1587

Walton, D. J., Middleton, M. J., Pinto, C., et al. 2016, The Astrophysical Journal Letters, 826, L26

Walton, D. J., Pinto, C., Nowak, M., et al. 2020, Monthly Notices of the Royal Astronomical Society, 494, 6012

Wang, C., Soria, R., & Wang, J. 2019, The Astrophysical Journal, 883, 44

Watarai, K.-y., Fukue, J., Takeuchi, M., & Mineshige, S. 2000, Publications of the Astronomical Society of Japan, 52, 133

Webb, N., Cseh, D., Lenc, E., et al. 2012, Science, 337, 554

Wiktorowicz, G., Lasota, J.-P., Middleton, M., & Belczynski, K. 2019, The Astrophysical Journal, 875, 53

Wilms, J., Allen, A., & McCray, R. 2000, The Astrophysical Journal, 542, 914

Wilson-Hodge, C. A., Malacaria, C., Jenke, P. A., et al. 2018, The Astrophysical Journal, 863, 9

Wu, S., Coughlin, E. R., & Nixon, C. 2018, Monthly Notices of the Royal Astronomical Society, 478, 3016

Zampieri, L. & Roberts, T. P. 2009, Monthly Notices of the Royal Astronomical Society, 400, 677